

MULTIPLEXED HIGH-RESOLUTION IMAGING APPROACH TO DECIPHER THE  
CELLULAR HETEROGENEITY OF THE KIDNEY AND ITS ALTERATION IN  
KIDNEY DISEASE AND NEPHROLITHIASIS

Angela Renae Sabo

Submitted to the faculty of the University Graduate School  
in partial fulfillment of the requirements  
for the degree  
Doctor of Philosophy  
in the Department of Cellular and Integrative Physiology,  
Indiana University

January 2023

Accepted by the Graduate Faculty of Indiana University, in partial fulfillment of the requirements for the degree of Doctor of Philosophy.

Doctoral Committee

---

James C. Williams, Jr., PhD, Chair

---

Tarek M. El-Achkar, MD

December 2, 2022

---

Sharon M. Moe, MD

---

Kenneth W. Dunn, PhD

© 2023

Angela Renae Sabo

## ACKNOWLEDGEMENTS

There are a number of people that deserve more than an acknowledgement for the help and support they have provided me over the years. I can only hope that I have made my appreciation known, that the work I have done makes each person proud, and that I continue to make them proud as I move forward in my career.

I first want to thank the friends that I have made throughout my academic journey, as they are what helped keep me focused through the endless hours of studying and researching. Zoë Terwilliger, there isn't enough paper in the world to write out how appreciative of you I am. Our 4+ hour long phone calls kept me sane; I will be forever grateful to have you to go to for judgment-free advice and ranting. You are the reason I am addicted to Starbucks coffee now, but I think it's a fair trade for the unconditional support you have shown me. Alissa Novak, if not for you, I would have never thrived as much as I did through the first semester classes here. Our late-night pizza and Red Bull fueled study sessions were more fun than they had any right to be, and a small part of me misses them some days. Lauren Hirschfeld, Samantha Colin, and Dr. Paige Ni, our margarita and taco nights, while random and not nearly frequent enough, always came when we all needed them most and I look forward to more as we all start our careers.

The other members of the labs I was part of deserve one of the biggest thank you's I can give, simply for having to deal with me every day of the week. I wish I could name everyone between the two labs, but my acknowledgements would be as long as my thesis itself if I tried that, there's so much to be thankful for with this group. Dr.'s Daria Barwinska and Kaice LaFavers, the two of you provided endless hours of help, advice, and laughs over the years, and I look forward to many more as we continue to work

together. Dr. Michael Ferkowicz, I owe almost everything I know about microscopy to you. If not for your patience, perfectionism, and inability to say no, this work would be nowhere near the quality it is now. You taught me, much to everyone else's dismay, that it is perfectly okay to demand perfection, even when it seems unattainable.

I've also had many mentors throughout my career, but were it not for each of them, I would not be the scientist I am today. My undergraduate research mentor, Dr. Pamela Connerly, you took a chance on letting me join your lab as a freshman with no experience, and for that I am forever grateful. The day I started in your lab is the day I knew I would be a researcher until I could no longer make it to a lab bench. I always knew I wanted to be in science but working with you solidified the role I wanted to play in the scientific community. Dr. Seth Winfree, while not a formal mentor, you certainly left an impact on me and my career, and I cannot put into words how much I appreciate all of the time you put into helping me. What I don't owe Mike for my microscopy skills and perfectionism, I owe to you. I remember one of the first times you were helping me image, you told me something along the lines of "one day you'll be moving around on this scope like a pro" and I thought you were absolutely crazy. I am happy to admit that you were right, and that imaging is by far one of my favorite activities. You have taught me so much about imaging, analysis, and coding (against every attempt of me avoiding it) and have provided me with invaluable life and career advice. Were it not for you believing in my abilities and pushing me, I would be lost.

My PhD mentors, Dr.'s James Williams and Tarek Ashkar, you two provided me something I never expected to find in my graduate career – a second family. There was no question in my mind that your labs were the right choice for me. The environment you

foster is that of love and kindness and being part of that environment made my time in graduate school better than it deserved to be. There was not a single day that I felt unappreciated or alone in that lab. Dr. Williams, your patience is unmatched, and I hope to be even half the mentor and teacher you are one day. You taught me many things throughout my time in the lab, but the most important was to be kind to myself and allow myself to make mistakes – a task I will always struggle with. Dr. Ashkar, you were a fierce supporter of me from day one, and the opportunities you provided me with over the years are immeasurable. There were times I doubted myself and my abilities, but you never let those doubts keep me from being successful. Your support and confidence in me carried me through the times where I felt as if I was not right for this field, and I am so thankful you always saw my potential.

Lastly, I would like to thank my parents and my brother. Mom and Dad, you guys encouraged me from day one to pursue my dreams, and you made sure I had the means to do so. I would not be where I am today if not for your support, love, and guidance. I may not follow you guys around with a stack of Dr. Seuss books anymore, but I will always be the ever-curious little girl you raised, asking questions to the point of exhaustion and annoyance. Steven, you are my absolute best friend and I appreciate everything you have done for me. Your support means more to me than you will ever know, and I don't know where I would be without it. The three of you are my strongest supporters, and as long as I continue to make you all proud, I will always consider myself successful. I love you.

All works included in this thesis are used with permission of the publishers and/authors.

Angela Renae Sabo

MULTIPLEXED HIGH-RESOLUTION IMAGING APPROACH TO DECIPHER THE  
CELLULAR HETEROGENEITY OF THE KIDNEY AND ITS ALTERATION IN  
KIDNEY DISEASE AND NEPHROLITHIASIS

Kidney disease and nephrolithiasis both present a major burden on the health care system in the US and worldwide. The cellular and molecular events governing the pathogenesis of these diseases are not fully understood. We propose that defining the cellular heterogeneity and niches in human and mouse kidney tissue specimens from controls and various models of renal disease could provide unique insights into the molecular pathogenesis. For that purpose, a multiplexed fluorescence imaging approach using co-detection by Indexing (CODEX) was used, using a panel of 33 and 38 markers for mouse and human kidney tissues, respectively. A customized computational analytical pipeline was developed and applied to the imaging data using unsupervised and/or semi-supervised machine learning and statistical approaches. The goal was to identify various cell populations present within the tissues, as well as identify unique cellular niches that may be altered with disease and/or injury. In mice, we examined disease models of acute kidney injury (AKI) and in human tissues we analyzed specimens from patients with AKI, IgA nephropathy, chronic kidney disease, systemic lupus erythematosus, and nephrolithiasis. In both mice and humans, the disease and reference samples show similar broad cell populations for the main segments of the nephron, endothelium, as well as similar groups of immune cells, such as resident macrophages and neutrophils. When comparing between health and disease, however, a

change in the distribution of few sub-populations occurred. For example, in human kidney tissues, the abundance and distribution of a subpopulation of proximal tubules positive for THY1 (a marker of differentiation and repair), was markedly reduced with disease. Changes observed in mouse tissues included shifts in the immune cell population types and niches with disease. We propose that our analytical workflow and the observed changes in situ will play an important role in deciphering the pathogenesis of kidney disease.

James C. Williams, Jr., PhD, Chair

Tarek M. El-Achkar, MD

Sharon M. Moe, MD

Kenneth. W. Dunn, PhD.



## TABLE OF CONTENTS

List of Tables .....	xi
List of Figures .....	xii
List of Abbreviations .....	xiv
Introduction and Background .....	1
Stone Disease .....	3
Kidney Disease – Chronic and Acute .....	6
Chapter 1 - Label-free imaging of non-deparaffinized sections of the human kidney to determine tissue quality and signatures of disease .....	8
Introduction .....	8
Results .....	11
Discussion .....	14
Methodology .....	17
Chapter 2 - Developing a robust analytical pipeline for large-scale data .....	30
Introduction .....	30
2.1 - Large-scale three-dimensional imaging and analysis of the human kidney .....	31
Introduction .....	31
Results .....	33
Discussion .....	43
Methodology .....	50
2.2 – Excerpt from: Integrated cytometry with machine learning applied to high- content imaging of human kidney tissue for in-situ cell classification and neighborhood analysis .....	55
Introduction .....	55
Results .....	58
Discussion .....	59
Methodology .....	64
Chapter 3 - CODEX multiplexed imaging of the murine kidney .....	82
Introduction .....	82
Results .....	84
Discussion .....	88
Methodology .....	90
Chapter 4 - Surveying the heterogeneity in the renal cortex and its changes in disease ...	99
Introduction .....	99
Results .....	100
Discussion .....	103
Methodology .....	105
Chapter 5 - CODEX Multiplex imaging of the Renal Papilla .....	115
Introduction .....	115
5.1 - A Spatially anchored transcriptomic atlas of the human kidney papilla identifies significant immune injury and matrix remodeling in patients with stone disease .....	116
Introduction .....	116
Results .....	118
Discussion .....	126

Methods.....	134
Chapter 6 - Summary of Work.....	156
References.....	159
Curriculum Vitae	

## LIST OF TABLES

Table 1.1 - Summary of tissue samples and the steps of the processing pipeline .....	20
Table 2.1 - Results of label free and VTEA analysis of five nephrectomy samples .....	69
Table 2.2 - Results of label free and VTEA analysis of three diabetic biopsies.....	75
Table 2.3 - Antibodies used for CODEX multiplexed imaging .....	77
Table 3.1 - Antibodies used for CODEX multiplexed imaging of mouse kidney specimens .....	92
Table 4.1 - Antibodies used for CODEX multiplexed imaging on human renal cortex..	108
Table 5.1 - Antibodies used for CODEX multiplexed imaging on human renal papilla..	156

## LIST OF FIGURES

Figure 1.1: Flowchart representing the general methodology described in this paper. ....	21
Figure 1.2: Widefield fluorescence imaging of non-deparaffinized tissue sections allows for quality assessment.....	22
Figure 1.3: Two-photon imaging and second harmonic generation imaging yield quantitation on collagen content. ....	23
Figure 1.4: SHG imaging results correlate with Lillie's allochrome staining for collagens. ....	24
Figure 1.5: SHG imaging results correlate with Lillie's allochrome staining for collagens. ....	25
Figure 1.6: Detection of changes in tubulo-interstitial and glomerular endogenous fluorescence during disease. ....	26
Figure 1.7: Nuclear staining and cytometry can be conducted on paraffin-embedded samples without deparaffinization. ....	28
Figure 2.1: Overview of the tissue cytometry workflow. ....	67
Figure 2.2: 3D multiphoton microscopy of unlabeled nephrectomy. ....	68
Figure 2.3: 3D confocal immunofluorescence of structural markers ....	70
Figure 2.4: 3D confocal fluorescence microscopy and cytometry of structural and immune cell markers.....	71
Figure 2.5: 3D confocal fluorescence and multiphoton autofluorescence/SHG microscopy of regions of apparent injury. ....	73
Figure 2.6: 3D Multiphoton autofluorescence/SHG and confocal immunofluorescence microscopy of diabetic renal biopsies.....	74
Figure 2.7: Scatterplots of glomerular nuclear density and immune cell density.....	76
Figure 2.8: Automated detection, classification of cell-types and assessing cellular microenvironments in CODEX data with VTEA.....	78
Figure 2.9: Subclustering of epithelial cells in CODEX data uncovers novel cell states in the proximal tubular (PT) and thick ascending limb (TAL). ....	80
Figure 3.1: CODEX multiplex imaging allows for the identification and classification of all major cell types present within the kidney, including immune cells and injured populations.....	93
Figure 3.2: Subclustering and identifying immune cell populations. ....	95
Figure 3.3: Changes in abundance and distribution of myeloid cells in injury and THP -/- mice. ....	97
Figure 3.4: Myeloid niches change in injury and THP -/-. ....	98
Figure 4.1 Staining panel utilized for the human CODEX experiments. ....	109
Figure 4.2 Louvain clustering of reference tissue identifies major cell types. ....	111
Figure 4.3 Neighborhood analysis of reference tissues ....	112
Figure 4.4: Louvain clustering of reference and disease tissues show changes in abundance of clusters.....	113
Figure 4.5: Neighborhood analysis of reference and disease specimens so unique injury niches.....	114
Figure 5.1: Spatially anchored cellular and molecular characterization of the human kidney papilla.....	144
Figure 5.2: Differentially expressed genes (DEGs) induced by stone disease in	

various cells within the human papilla.....	147
Figure 5.3: MMP7 expression in the papilla.....	149
Figure 5.4: Signatures of injury and inflammation are localized to regions of mineralization in the kidney papilla from stone disease. ....	150
Figure 5.5: CODEX imaging of a papilla with mineral deposition identifies various stages of immune activation and fibrosis around the plaque. ....	152
Figure 5.6: Protein markers of oxidative stress (ROS) and macrophage activation are diffusely increased in biopsies of stone patients. ....	154
Figure 5.7: MMP7 and MMP9 levels are increased in urine of CaOx stone patients and correlate with disease activity. ....	155

## LIST OF ABBREVIATIONS

3D	three-dimensional
ABCC6	ATP binding cassette subfamily C member 6
AKI	Acute Kidney Injury
AQP1	Aquaporin 1
AQP2	Aquaporin 2
CaOx	Calcium Oxalate
CKD	Chronic Kidney Disease
CLIA	Clinical Laboratory Improvement Amendments
CLP	Cecal Ligation Puncture
CODEX	CO-Detection by indEXing
DEGs	Differentially Expressed Genes
DKD	Diabetic Kidney Disease
FSGS	Focal segmental glomerulosclerosis
FN1	Fibronectin
HuBMAP	Human BioMolecular Atlas Program
IRI	Ischemia Reperfusion Injury
IC	Intercalated Cells
KPMP	Kidney Precision Medicine Project
MMPs	Matrix Metalloproteinases
MPO	Myeloperoxidase
NBF	Neutral-buffered Formalin
OCT	Optimal Cutting Temperature

OPN	Osteopontin
PC	Principal Cells
p-c-JUN	Phosphorylated c-JUN
PFA	Paraformaldehyde
PPi	Inorganic Pyrophosphate
PROM1	Prominin-1
ROI	Region of Interest
RP	Randall's Plaque
snRNAseq	Single nuclear RNA sequencing
SLE	Systemic Lupus Erythematosus
SPP1	Osteopontin
ST	Spatial Transcriptomics
TC	Tissue Cytometry
THP	Tam-Horsfall Protein
tSNE	t-distributed stochastic neighbor embedding
UMAP	Uniform Manifold Approximation and Projection
UMI	Unique Molecular Identifier
VIM	Vimentin
VSGE	Visium spatial gene expression

## Introduction and Background

The renal space is complex, with numerous different cell types that each have important roles that allow the kidney to function properly. For epithelial cells alone, at least 16 distinct cell types have been identified, and the number of endothelial, interstitial, and immune cells likely outnumber the epithelial population (Balzer 2022). Being able to identify and distinguish these cells accurately is an important aspect of renal research, therefore we need a robust methodology for cell identification. Identifying these cell types is only the tip of the renal iceberg, however. There are many technologies that allow for the identification of all cell types in the kidney, but a majority of these technologies lack an important feature: the spatial localization of the cell types. Without knowing the location of the cells that are present within a kidney, it is impossible to determine cell-to-cell interactions/associations. Imaging technologies allow for the identification of cell types, as well as provides the spatial information many other technologies are missing. With imaging, areas of damage or infiltration are often seen, and can help provide insight as to what is happening in a kidney when it is damaged or diseased (Ferkowicz 2021).

Standard confocal microscopy allows for the imaging of tissue that is up to 100 microns thick, providing a three-dimensional look at the renal space. While this provides copious amounts of spatial information, the ability to accurately identify all of the cells present in the kidney is lacking. With standard confocal microscopy, four probes is the maximum number that can be used, unless spectral deconvolution is utilized, which raises the maximum to eight probes. Even the upper limit of eight is still not enough to identify all cells present within the kidney. With the ability to obtain large-scale, high-resolution



images, comes the limitation in the number of cells that can be identified within one tissue specimen.

Dissociative cell-based assays such as single cell transcriptomics, flow cytometry, etc., are beneficial in that they can provide information on the transcriptome of whatever tissue or collection of cells that were analyzed. The only way to achieve spatial information with these methodologies is to analyze regions of the kidney separately, i.e., separating the cortex, medulla, and papilla from one another. This, however, would provide only a rough estimate of spatial information, and scale is limited to the region of the kidney, rather than a cell-based resolution like imaging can provide.

With spatial transcriptomics, imaging and whole-transcriptome mRNA expression analysis are combined. The results of the transcriptomic analysis are overlaid onto a histology image of the same tissue section that was analyzed, so the spots can be visualized on the tissue itself. While this method does give researchers a more complete look at the location each of the transcripts come from, that location is still approximate, as the spots analyzed are not at a cellular resolution.

Another caveat to technologies such as spatial transcriptomics and dissociative cell-based assays is that since the entire transcriptome is being analyzed, the results may not always correspond to proteins that are active in the cells. While knowing the whole transcriptome is beneficial and provides an extraordinary glimpse into the innerworkings of the renal space, knowing which of those transcripts corresponds to active proteins provides the best look at what is happening in the kidney when diseased or injured.

In order to have a “limitless” number of targets available for analysis, as well as obtain cellular resolution based spatial information, cyclic imaging needs to be utilized.

CO-Detection by indEXing (CODEX), a multiplex imaging platform created by Gary Nolan and distributed by Akoya Biosciences, allows for an almost unlimited number of probes to be imaged on one tissue section by creating a cyclic imaging system, where antibodies with unique barcodes are matched to reporters with complimentary barcodes. Each cycle consists of applying three reporters, imaging said reporters, and then removing the reporters so the next set can be added. This is repeated as many times as necessary, with DAPI (a nuclear stain) included in each cycle for tissue alignment once imaging is completed. This not only gives us the capability of identifying numerous cell types at one time, but also reduces the amount of tissue that is needed from each specimen, which is an especially important aspect when working with human tissue specimens.

This CODEX multiplexed imaging combined with unsupervised clustering and analysis will allow for identification of cell types present and the niches that those cells make up when they interact with one another. Due to the complex nature of the kidney, there are many renal diseases that could benefit from an in-depth cellular resolution-based analysis. By uncovering the cellular neighborhoods present and how they interact with one another, new insights into how a disease begins and/or progresses can be found. Three renal diseases of interest will be analyzed in this work, including stone disease, acute kidney injury, and chronic kidney disease.

### **Stone Disease**

Nephrolithiasis (kidney stone disease) is one of the oldest diseases known to man, with reports in medical texts as early as 3200 BCE (Modlin 1980, Shah 2002). In the United States alone, one-in-eleven individuals will be affected by stone disease, and 50%

of those people will have a stone recurrence within ten years of their first incident (Scales 2012). Despite the prevalence of nephrolithiasis, there are still numerous questions surrounding the development of kidney stones, and how to best prevent them.

The most common type of kidney stone is calcium oxalate (CaOx), which accounts for more than two-thirds of all kidney stones (Bouderlique 2019). A common feature of CaOx stones is that they tend to form on Randall's plaque (RP), a deposit of calcium phosphate that begins forming in the tip of the renal papilla. This plaque deposit starts forming in the interstitium surrounding the thin ascending limbs of the Loop of Henle and vasa recta in that area. In some individuals, the papillary epithelium covering the plaque loses its integrity and the interstitial plaque is exposed to the urine in the renal calyx. If this happens, the plaque can then act as a nidus for a stone to begin forming. As the stone begins to form, the plaque acts as an anchor, holding the stone in place. Even less is understood about RP than with kidney stones themselves, leaving another large gap in the literature surrounding nephrolithiasis. Questions surrounding RP that many researchers are attempting to answer include how this plaque begins to form, what changes are happening at the cellular level to allow for this plaque development, and why individuals with RP do not always form stones.

There have been studies that suggest a role of the immune system during stone formation on RP in humans, primarily from macrophages and T cells (Okada 2009, Taguchi 2018). These studies focus on the stone formation rather than the formation of plaque itself, however, still leaving the mystery of plaque formation unanswered. Studying how plaque forms, however, is complicated. Individuals do not usually know they have plaque forming until they have a stone event, therefore the chances of catching

plaque formation early are slim. Until recently, there were no rodent models available that accurately depicted RP.

In recent years, a mouse model for pseudoxanthoma elasticum has been found to be an accurate model of RP, where plaque can begin forming as early as six months (Bouderlique 2019). This mouse model is the only model of RP that has been found to date, and studies that have been conducted thus far show that these mice have the same formation pattern as that of human RP (Bouderlique 2019, Letavernier 2019, Letavernier 2018). In this mouse, the ABCC6 (ATP binding cassette subfamily C member 6) gene is knocked out. While ABCC6 is primarily expressed in the liver, there is also a significant level of expression in the renal tubules (Letavernier 2018). When functioning normally, ABCC6 is involved in transporting ATP from cells, which is then converted into AMP and inorganic pyrophosphate (PPi), the latter of which is an inhibitor of ectopic calcification. When ABCC6 is knocked out, that PPi generation is reduced, therefore allowing ectopic calcification to occur, which in the renal space presents as RP (Jansen 2014, Letavernier 2018).

In order to fully understand the mechanism behind the development of RP and CaOx stones, analyzing the renal space at the cellular level is critical. Currently, the level of damage that the papillary space encounters during the development of plaque is incompletely understood. Characterizing the cellular make-up of the papilla in both stone formers and control samples can provide information on what is occurring before plaque begins to form, during the plaque formation, and even what occurs to cause the loss of papillary epithelium in individuals that get stone formation on plaque. The cortex of stone

formers will be analyzed as well, in order to evaluate what changes may occur further away from the stone/plaque event.

### **Kidney Disease – Chronic and Acute**

Chronic kidney disease (CKD) is defined as the gradual loss of kidney function, mainly caused by hypertension, diabetes mellitus, or glomerular inflammatory conditions. Acute kidney injury (AKI), however, is defined as the sudden failure of the kidneys due to injury, medications, or illness. While these conditions were classically thought of as two separate entities, their relationship has recently been reevaluated. CKD has now been recognized as a major risk factor for the development of AKI, and patients with CKD are less likely to fully recover from incidents of AKI. Similarly, patients who have had AKI are more likely to develop progressive CKD later in life.

In the case of AKI, the endothelium is affected first and immune cells such as inflammatory neutrophils and monocytes are recruited. During the reparative process after injury has occurred, M2 (pro-repair) macrophages become the dominant immune cell present rather than neutrophils. Complete repair can take several days and is characterized by normalized creatinine levels and no proteins present in the urine. With CKD, injury can begin in the vasculature, the tubulointerstitium or the glomerulus. No matter where the injury occurs, the microvasculature is lost, and fibrosis increases, causing hypoxia. Tubular cells are lost as well, and are replaced with fibrosis, further increasing the loss of renal function.

Understanding the cellular changes that occur in AKI and CKD could help provide important insight into the development and progression of both diseases. By characterizing the cellular changes that occur with each disease, researchers could find

therapeutic targets in order to slow the progression or potentially help reverse certain types of damage. To study AKI, mouse samples that have undergone ischemia reperfusion injury will be utilized, as well as human tissue specimens that were obtained from diagnostic biopsies. Tam-Horsfall Protein (THP, also known as Uromodulin) knockout mice will be utilized to study AKI, as THP has been shown to have a protective role in AKI, and mice lacking THP are more sensitive to injury caused by AKI. CKD will also be analyzed via human tissue specimens, but no mouse models will be analyzed.

## Chapter 1 - Label-free imaging of non-deparaffinized sections of the human kidney to determine tissue quality and signatures of disease

The following manuscript is used with permission of the publisher (Sabo 2021).

### **Introduction**

The global prevalence of kidney disease exceeds 9% and is associated with significant morbidity, mortality, and economic burden (Carney, 2020). Our understanding of the pathogenesis of human kidney disease continues to evolve, in part due to advances in the molecular interrogation and imaging of human kidney biopsy specimens (Barwinska 2021, El-Achkar 2021, Ferkowicz 2021). Frequently, the specimens obtained after a diagnostic kidney biopsy may be too small or of limited quality and require a significant effort by nephropathologists to perform an appropriate diagnostic evaluation. Furthermore, based on recommendations from the College of American Pathologists, and to assure compliance with Clinical Laboratory Improvement Amendments (CLIA) laws and regulations, pathologists must retain paraffin blocks for a period of 10 years (Khoury 2008). Therefore, the availability of kidney biopsy specimens for research purposes is limited. Endeavors such as the Kidney Precision Medicine Project are underway to study prospectively collected kidney biopsies with detailed clinical phenotypes (de Boer 2021). These samples are acquired from altruistic donors and the available kidney tissue is both precious and scarce. Thus, an effective means to extract additional information from human biopsy specimens while conserving tissue is highly desirable and could benefit not only researchers but also patients who may be able to circumvent repeat biopsy procedures when the tissue obtained is limited.

In conventional diagnostic preparations, patient-sourced biopsy specimens are fixed in 10% neutral buffered formalin (NBF), processed into paraffin blocks, and sectioned into delicate ribbons of tissue that are mounted on glass slides and subsequently deparaffinized for downstream histochemical and/or immunohistochemical techniques. On average, a diagnostic biopsy specimen from an 18G needle provides cylindrical tissue cores with a diameter of  $\sim 1$  mm (Roth 2013). From a specimen of this size, one can expect to obtain a limited number of histological sections of 2–5 micron thickness from the middle portion of the tissue, assuming the long axis of the tissue core is aligned parallel to the face of the paraffin block. Such specimens are typically prioritized for diagnostic use, thereby limiting the amount of tissue that can be released for institutionally approved research studies. To overcome this limitation, we believe there is value in developing tissue-sparing techniques that both qualify and quantify histopathology. Such an approach would maximize the amount of information that could be obtained from a single specimen, which is especially important for tissue samples of limited or insufficient volume.

Label-free fluorescence imaging describes the process of exciting and acquiring a fluorescence signal from tissue sections without the addition of any fluorescent probes. This process takes advantage of the endogenous fluorescence of several metabolites or proteins within the tissue (Hato 2017). Furthermore, molecules with non-centrosymmetric molecular structure such as fibrillar collagen (e.g., types I and II) and actomyosin produce a nonlinear optical effect known as second harmonic light when excited with an intense laser source (Chen 2012, Strupler 2007). Second harmonic generation (SHG) imaging has become more established for tissue-based microscopy,



and we have recently shown that combining label-free and SHG imaging with subsequent multi-fluorescence confocal microscopy in a single kidney section can be very valuable in evaluating the pathobiology of kidney disease (Ferkowicz 2021). The use of label-free imaging in conventional tissue processing and diagnostic preparations is not established (Bonsib 1990). In particular, the application and utility of label-free imaging in non-deparaffinized human kidney sections have not been previously reported.

In this project, we sought to determine the feasibility and usefulness of label-free imaging of formalin-fixed paraffin-embedded kidney sections without deparaffinization. We established a broadly applicable methodology that allows for pre-qualification of the tissues to ensure that specimens of sufficient quality were selected for further analysis. Our results show that both structural and morphological information can be obtained from paraffin sections before deparaffinization. Furthermore, using additional specialized microscopy, we explored whether biologically relevant information, such as collagen content assessed by SHG imaging and changes in endogenous fluorescence, could be useful in defining a signature for disease, even before histological assessment occurs. This has been conducted previously in sections that have already undergone deparaffinization (Bhuiyan 2021, Ranjit 2015, Ranjit 2016) but not in sections that are still embedded in paraffin. We propose that the knowledge from label-free imaging of non-deparaffinized sections could guide downstream processing in a conventional histologic workflow. Our findings also have implications for tissue economy in multimodal molecular and imaging interrogation of human kidney biopsy specimens.

## Results

### *Workflow for data extraction from fresh frozen paraffin embedded (FFPE) sections without deparaffinization*

Eighteen kidney biopsy specimens were used in this study and are described in Table 1.1. Specimens from the kidney cortex were either from kidney stone-forming patients with normal kidney function obtained during percutaneous nephrolithotomy or from clinically indicated kidney biopsies of patients with an eventual primary pathology diagnosis of diabetic kidney disease (DKD) or focal segmental glomerulosclerosis (FSGS). After fixation, the specimens underwent standard processing for paraffin embedding and sectioning. The sections were imaged first using widefield epifluorescence microscopy to quickly assess the quality of the tissue section, followed by second harmonic generation imaging and endogenous fluorescence signature determination (Figure 1.1). Finally, for the purpose of adjudication, sections were deparaffinized and stained with Lillie's allochrome.

### *Rapid tissue qualification using widefield epifluorescence microscopy*

Widefield epifluorescence imaging was conducted on non-deparaffinized tissue sections in order to provide a quick assessment of tissue quality without damaging the tissue or relying on time-intensive analyses. In most cases, the total duration of this step did not exceed 10 minutes per tissue. To "pass" qualification, a section must have visible glomeruli (at least one must be clearly visible, but most times multiple glomeruli were observed), the tubules had to be morphologically distinguishable, and the tissue had to be of sufficient dimensions (qualitatively assessed as enough area to distinguish periglomerular space from other cortical areas) to provide an adequate area for analysis.

In Figure 1.2, an example of a tissue that met all three requirements is shown (Figure 1.2A), as well as a specimen that did not successfully pass this step (Figure 1.2B). In total, eleven samples were chosen for further study: five specimens from stone-forming patients (one of whom had also a history of diabetes), two with DKD and four with FSGS (Table 1.1).

#### *Quantifying fibrosis and endogenous fluorescence with label-free imaging*

To test if interstitial fibrosis could be imaged while a section was still embedded in paraffin, samples underwent SHG imaging. Such imaging was conducted by exciting the samples at 910 nm and collecting between 440 and 460 nm to select for fibrillar collagen. Endogenous fluorescence was captured concurrently using confocal microscopy. Figure 1.3 shows the SHG and autofluorescence images obtained from the nephrolithiasis kidney specimens. The amount of fibrosis present in the sample was measured by an unsupervised thresholding algorithm (Otsu 1979) and was normalized to the total area of the tissue as reported in Figure 1.3D.

#### *Histological adjudication of label-free imaging*

Label-free images collected from sections before deparaffinization were compared to images collected after deparaffinization and staining with Lillie's allochrome. Because this comparison is performed on the same sections without altering the orientation, the label free and stained images were spatially registered. (Figure 1.4). Areas of high signal in the SHG channel showed a correlation with the blue collagen staining in the Lille's allochrome images, indicating areas of interstitial fibrosis. Furthermore, glomeruli and distal tubular segments had a unique dim autofluorescence signature compared to proximal convoluted tubules.

To quantify how well the SHG signal correlated with the Lillie's allochrome staining, regions were selected at random across four samples and scored. SHG images were "scored" using Otsu autothresholding, as described above, and Lillie's allochrome images were scored by a nephropathologist. The correlation between the two sets of scores is shown in Figure 1.5C, along with representative images from the samples analyzed (Figure 1.5A and 1.5B).

#### *Assessing changes in autofluorescence signature in disease*

The average autofluorescence signal from the tubulo-interstitium was analyzed from images of the entire specimens obtained from widefield epifluorescence microscopy. An example image from each disease group is displayed in Figure 1.6. The tubulo-interstitium from stone-forming healthy patients had higher average endogenous fluorescence intensity compared to patients with diabetes or with FSGS (Figure 1.6D;  $p=0.02$  and  $< 0.01$ , respectively). Similar findings were obtained from high resolution images of the glomeruli using two-photon /SHG imaging (Figure 1.6E-H). Note that a stone-forming patient who had diabetes was included in the diabetic group (Figure 1.6G and 1.6H).

#### *Visualization of nuclei and measuring cell density in sections without deparaffinization*

The ability to visualize nuclei in kidney tissue sections without deparaffinization was tested by applying DAPI to the paraffin embedded sections. Imaging for this experiment was conducted with confocal microscopy, the results of which are shown in Figure 1.7. Our results show that we could successfully label all the nuclei in a non-deparaffinized tissue section. Such an approach allows the performance of tissue cytometry analysis on the tissue using the volumetric tissue exploration and analysis

(VTEA) software (Winfree 2017). There are numerous analyses that can be explored with the ability to label nuclei on non-deparaffinized samples, ranging in complexity from cell count/cell density analysis to machine learning techniques to determine cell types based on the nuclear morphology, as we have previously shown with fresh frozen as well as 4% paraformaldehyde (PFA) fixed kidney specimens (Woloshuk 2021). By segmenting all the nuclei in the imaging data, the total number of cells present in the tissue section shown in Figure 1.7A was measured and found to be 11,863 nuclei. Considering the autofluorescence signal of a specific structure, the cellular density in a specific region of interest (such as the glomeruli) can then be calculated (Figure 1.7). An example of this analysis is shown in Figure 1.7E-G, where we focus on a glomerulus. The results from the segmentation using VTEA are shown in Figure 1.7G, where we identified 141 cells in that particular glomerular cross-section.

## **Discussion**

Our study demonstrates that a sizable amount of actionable information can be obtained from tissue sections while they are non-deparaffinized. This data can be used for multiple applications such as qualification of the tissue for content and quality, quantitation of fibrosis, determination of disease signature or even nuclear staining without deparaffinization and tissue cytometry analysis. Since paraffin embedding of tissues is a standard and common practice, maximizing the amount of information that can be obtained before committing the tissue to downstream analysis could have potential advantages for workflow efficiency and increasing tissue utility and extending usability. Furthermore, in the case of scarce tissue, the proposed approach has direct implication on tissue conservation.

Extracting information that could guide downstream use does not need to occur in highly specialized settings, because visualization of tissue content and quality could be done with widefield epifluorescence microscope, an instrument that is widely available in most pathology labs. This commonly available technology can inform on the size of the tissue, glomerular content, and general tubule condition, without the need for staining or time-intensive analysis. A pipeline for screening paraffin-embedded tissue sections using widefield fluorescence could improve the efficiency of downstream processing. For example, an optimal diagnostic sample for glomerular diseases would include 15 or more glomeruli, and sometimes more than 20 glomeruli for diseases such as FSGS (Pritzker 2019, Roth 2013). By screening sections before staining, the optimal diagnostic sample could be identified a priori. Furthermore, a survey of the quality and content of all paraffin embedded sections could be very valuable for subsequent assignment to various assays and enhanced techniques (Messias 2015).

Specialized high content data can also be obtained from paraffinized tissue sections, such as the measurement of interstitial fibrosis with SHG imaging or applying nuclear staining to perform tissue cytometry and measure cellularity in various structures. Such data could be used in conjunction with other downstream imaging and molecular assays to maximize the use of limited tissue, such as in the case of a kidney biopsy specimen. The specificity of endogenous fluorescence to the type of tubules and structures could be leveraged for use in future machine learning applications to delineate the content of a tissue section at high resolution (Liu 2020, Rivenson 2019). Furthermore, our preliminary data suggest that endogenous fluorescence itself may be altered by

disease and could be potentially used for disease screening (Croce 2010). This needs to be validated in a larger dataset.

This study has limitations predominantly related to the sample size, which precludes us from making generalizable conclusions without validation in a larger study. Although the samples from surgeries and needle biopsies were processed in a similar standard protocol, they were performed in different laboratories. While there could be variations in practices that contribute to the differences seen between reference and disease samples, both laboratories have an established track record of expertise and collaboration in tissue processing (Evan 2014, Evan 2015), which makes this possibility less likely. The goal of our study was to show the feasibility of the approach and its application, and our preliminary findings warrant additional investigations in a larger study. A second limitation to this study is the decision to limit the samples used to those that contained cortical tissue. The fibrotic content could vary from the cortex to the medulla, which could require different imaging and/or analysis techniques to be utilized. In conclusion, our results show that label-free imaging of paraffin-embedded sections without deparaffinization is easily implemented on common microscopes and provides useful information about tissue quality as well as quantifiable features that could potentially inform on the biology of health and disease. Additional high content data could be obtained with more specialized imaging, with possible implications on tissue economy in multimodal molecular and imaging interrogation of sparse human kidney biopsy specimens.

## Methods

### *Sample Collection*

Tissue samples from patients with stone disease were obtained via percutaneous nephrolithotomy (Evan 2003). Patients were randomly selected from an ongoing study in which all patients were consented for study (Indiana University Institutional Review Board protocol #1010002261). After biopsies were performed, samples were fixed with 4% PFA and then embedded in paraffin. All samples selected for this paper were from calcium oxalate stone formers with normal kidney function.

DKD and FSGS needle biopsy specimens were obtained from the Biopsy Biobank Cohort of Indiana (Indiana University Institutional Review Board protocol #1601431846; Eadon 2020). These are diagnostic biopsies performed for clinical indication. After biopsy specimens were obtained, they were fixed with 10% formalin and then embedded in paraffin. The pathological diagnosis of DKD or FSGS was performed by a nephropathologist (C.P).

### *Widefield epifluorescence microscopy*

Non-deparaffinized kidney tissue sections were imaged using a Keyence BX810 slide scanner and three different filter cubes, including DAPI, GFP, and TRITC. Images were collected using a Nikon PanFlour 10x/0.3 Ph1 air objective.

### *Second Harmonic Generation and Two-photon Imaging*

Non-deparaffinized kidney tissue sections were also imaged with 2-photon microscopy using a 25x 0.95 NA Leica dipping objective with excitation provided by a MaiTai DeepSee tunable titanium-sapphire laser (Spectra Physics, Santa Clara, CA) adjusted to 910 nm. The descanned pathway was configured for multiphoton imaging by



fully opening the confocal pinhole and adjusting photomultiplier detectors to collect emissions from 440 to 460nm (for SHG) and from 493 to 776 nm (for autofluorescence).

#### *Single photon confocal imaging*

Confocal imaging was conducted using a 25x 0.95 NA Leica dipping objective. Autofluorescence was collected in four different channels, ranging from 400 to 776 nm.

#### *Staining sections with DAPI*

Non-deparaffinized kidney tissue sections were stained with DAPI to facilitate the calculation of the number of cells in the specimens. These sections were incubated with a 1:100 dilution of DAPI for 5 minutes, washed in PBS, and imaged as described above

#### *Histological Staining*

Deparaffinized tissue sections were stained with Lillie's allochrome to facilitate the distinction of different collagen types in the tissue. Allochrome is similar to Masson's trichrome, except collagens within the tubule basement membranes and interstitial fibrosis stain purple and blue, respectively (Lillie 1951).

#### *Image Analysis*

Image analysis was conducted using the open-source software ImageJ. The average fluorescence intensity of both the tubules and the glomeruli were measured in the three disease groups (Stone, Diabetes, and FSGS).

Cells were counted in images of DAPI stained sections with VTEA, a software plugin for ImageJ (Winfree 2017). VTEA utilizes nuclear staining, such as DAPI, to segment cells from the tissue volume for quantitation.

In order to calculate the amount of fibrosis in each sample, the total area of the tissues was calculated, and the average signal was measured. Otsu autothresholding was

then applied to select for SHG signal with high intensity (Otsu 1979), and the area occupied by the thresholded pixels was calculated using the “area fraction” measurement in ImageJ.

For correlation of SHG images to histology staining, three regions were randomly selected from four of the stone patient samples, for a total of twelve regions. Regions from the histology sections were scored by a nephropathologist. Regions from the SHG images were thresholded as described above, and the percent area occupied by SHG signal was calculated.

#### *Statistical Analysis*

Statistical analysis was conducted using PRISM software. Mean +/- standard deviation was reported. Statistical significance was determined using one-way ANOVA and significance was set to  $P < 0.05$ .

Sample	Tissue obtained through	Clinical Disease	No. of Gloms	Steps in Pipeline			
				Pre scanning	2P/SHG	Lillie's Allochrome	Analysis
Stone 1	PCNL	Nephrolithiasis	2	X	X	X	
Stone 2	PCNL	Nephrolithiasis	5	X	X	X	X
Stone 3	PCNL	Nephrolithiasis	3	X	X	X	X
Stone 4	PCNL	Nephrolithiasis	16	X	X	X	X
Stone 5	PCNL	Nephrolithiasis	0	X			
Stone 6	PCNL	Nephrolithiasis	4	X			
Stone 7	PCNL	Nephrolithiasis	2	X			
Stone 8	PCNL	Nephrolithiasis	0	X			
Stone 9	PCNL	Nephrolithiasis	0	X			
Stone 10	PCNL	Nephrolithiasis	3	X			
Stone 11	PCNL	Nephrolithiasis	8	X			
Diabetic 1	PCNL	Nephrolithiasis, Diabetes	2	X	X	X	X
Diabetic 2	Diagnostic kidney biopsy	Diabetes	2	X	X	X	X
Diabetic 3	Diagnostic kidney biopsy	Diabetes	15	X	X	X	X
FSGS 1	Diagnostic kidney biopsy	FSGS	9	X	X	X	X
FSGS 2	Diagnostic kidney biopsy	FSGS	15	X	X	X	X
FSGS 3	Diagnostic kidney biopsy	FSGS	5	X	X	X	X
FSGS 4	Diagnostic kidney biopsy	FSGS	9	X	X	X	X

Table 1.1 - Summary of tissue samples and the steps of the processing pipeline

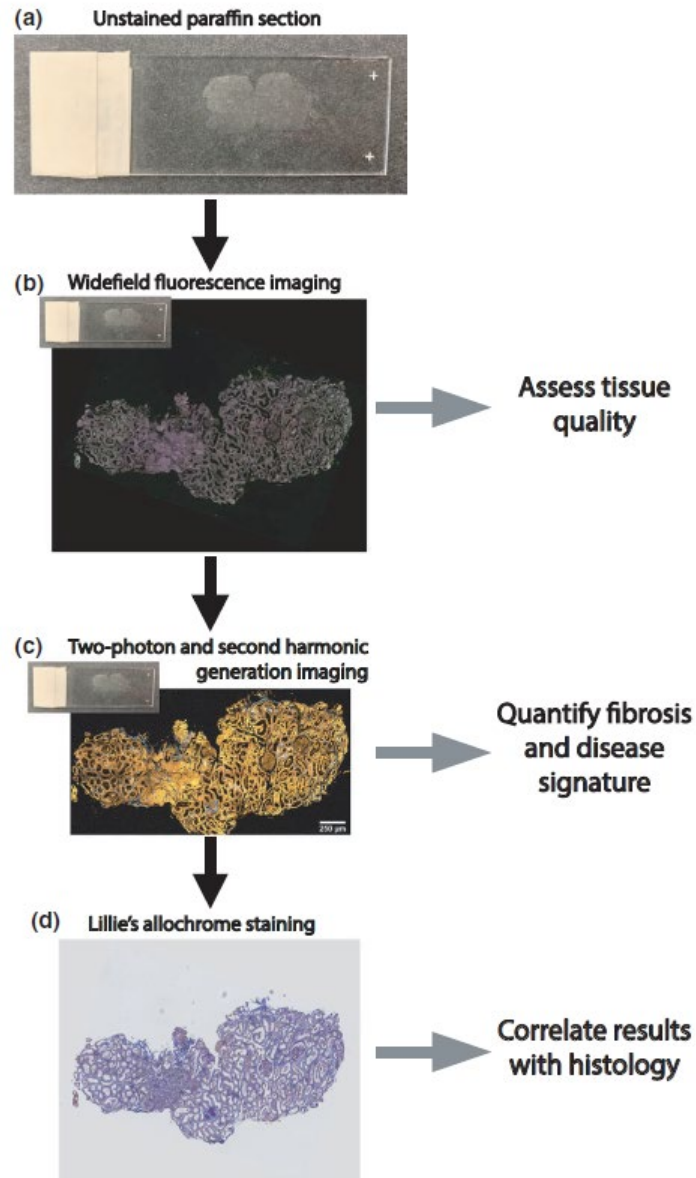


Figure 1.1: Flowchart representing the general methodology described in this paper.

A) example of a non-deparaffinized kidney tissue section. b) Representative image of a non-deparaffinized tissue section imaged using widefield epifluorescence. c) The same section was imaged using two-photon/second harmonic generation imaging. d) This section was lastly deparaffinized and stained with Lillie's allochrome.

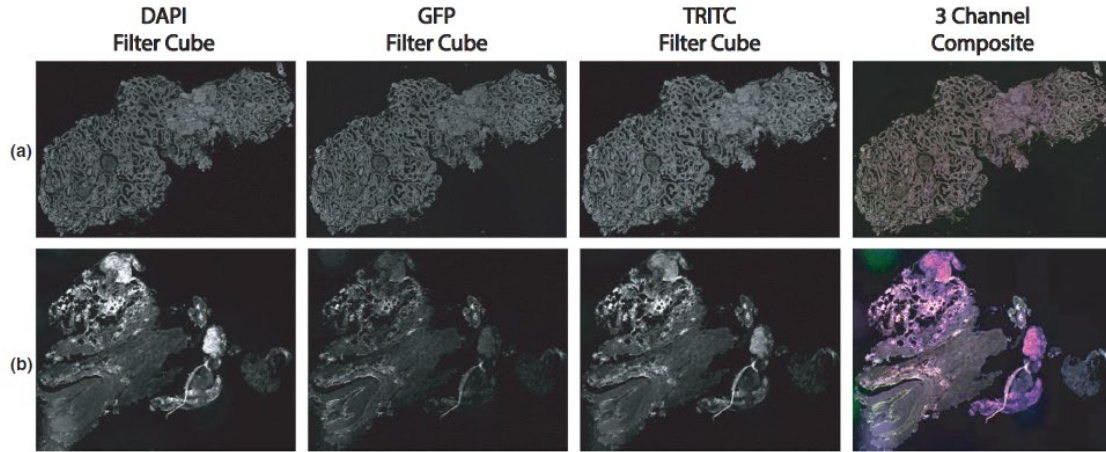


Figure 1.2: Widefield fluorescence imaging of non-deparaffinized tissue sections allows for quality assessment. Imaging was performed using a fluorescence slide scanner with filter cubes set for DAPI, GFP, and TRITC fluorescent spectra. Two samples are shown above, with each channel displayed individually and as a composite of the three channels. The sample in (a) (stone patient sample 1) was used for the duration of the study, whereas the sample in (b) (stone patient sample 5) was not used due to poor sample quality

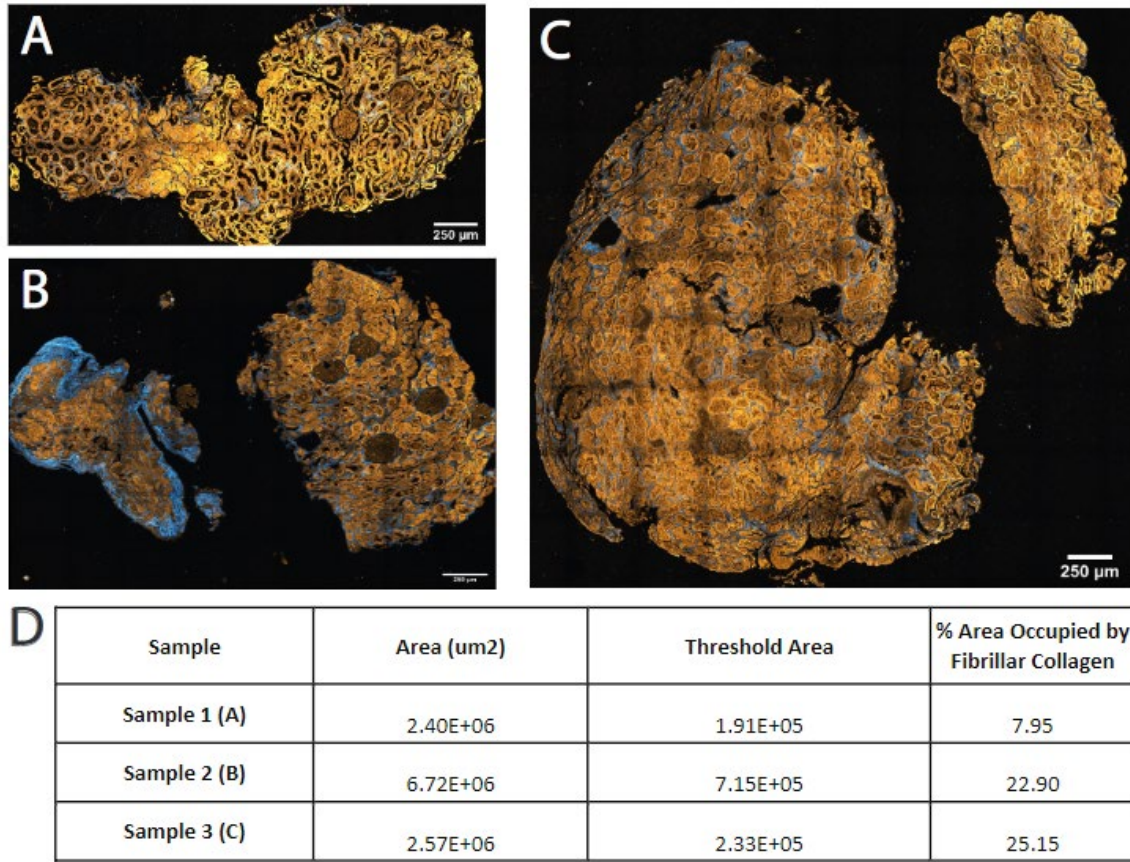


Figure 1.3: Two-photon /second harmonic generation imaging yield quantitation on collagen content. Two-photon imaging and SHG imaging were conducted on the four non-deparaffinized kidney tissue sections obtained from kidney biopsies of stone-forming patients. a–c) Tissue autofluorescence is displayed in orange, and collagens are shown in blue. To estimate the amount of collagenous content in each sample unsupervised thresholding on the signal was applied and was normalized to the tissue area. Results from that analysis are shown in (d)



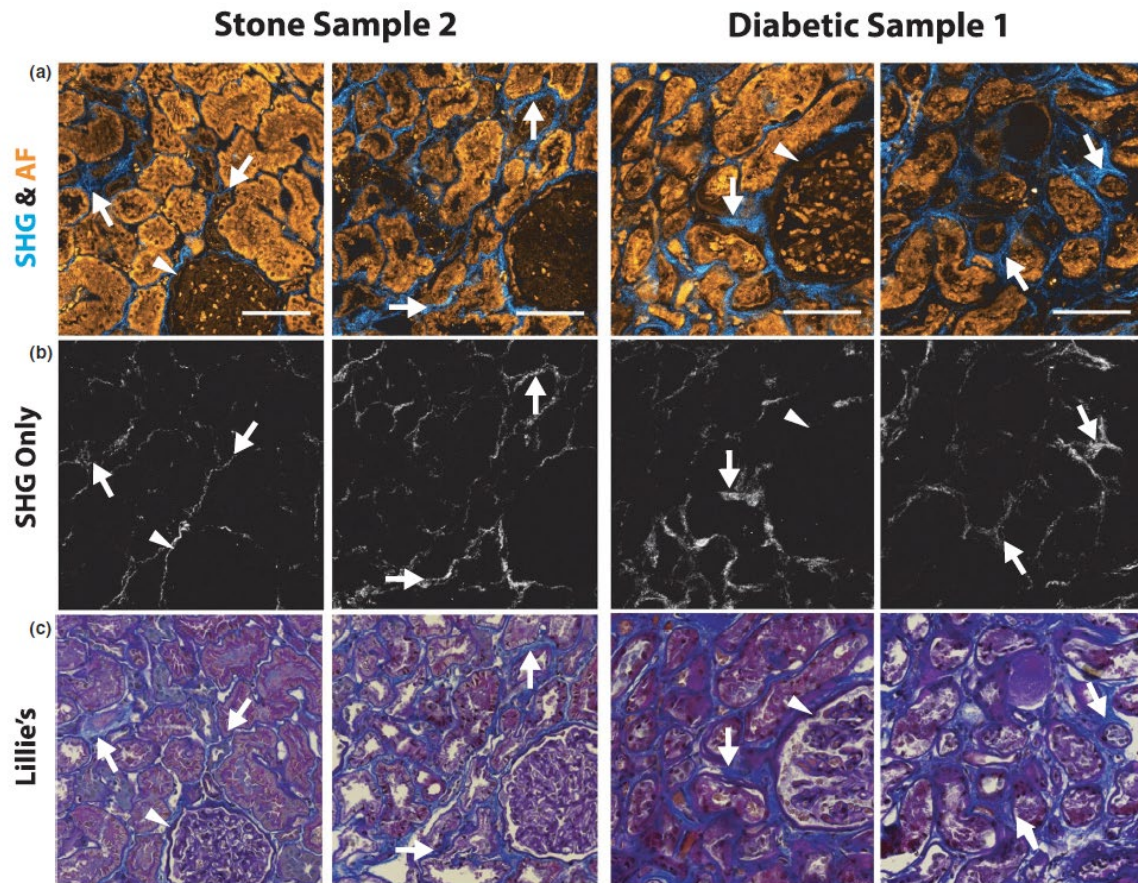


Figure 1.4: SHG imaging results correlate with Lillie's allochrome staining for collagens. a) SHG imaging and two-photon autofluorescence from two different samples. b) The same images with only SHG signal displayed. c) The same regions from the same sections are displayed after staining with Lillie's allochrome. The blue hue corresponds to fibrosis, dark purple is showing collagens that makeup the basement membranes (arrowheads, typically non-fibrillar), and nuclei are stained dark brown/black. Arrows denote areas of signal in the SHG images that correlate with the Lillie's allochrome stain. Glomeruli and distal tubular segments have a dim autofluorescence compared to proximal tubules. Scale bars are 100 microns

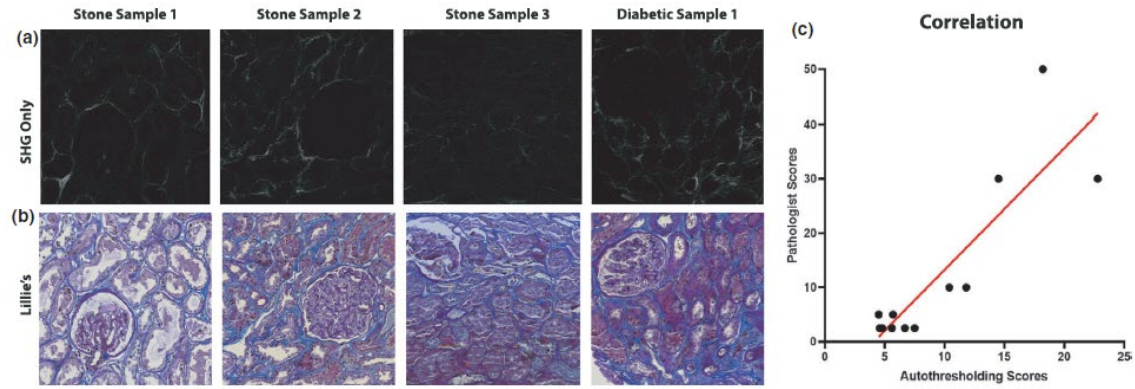


Figure 1.5: SHG imaging results correlate with Lillie's allochrome staining for collagens. a) SHG signal of one region from each scored sample. b) The same regions from the same sections after staining with Lillie's allochrome. c) Shows the correlation of pathologist scoring of Lillie's allochrome staining to scoring from auto-thresholding ( $r^2 = 0.752$ )



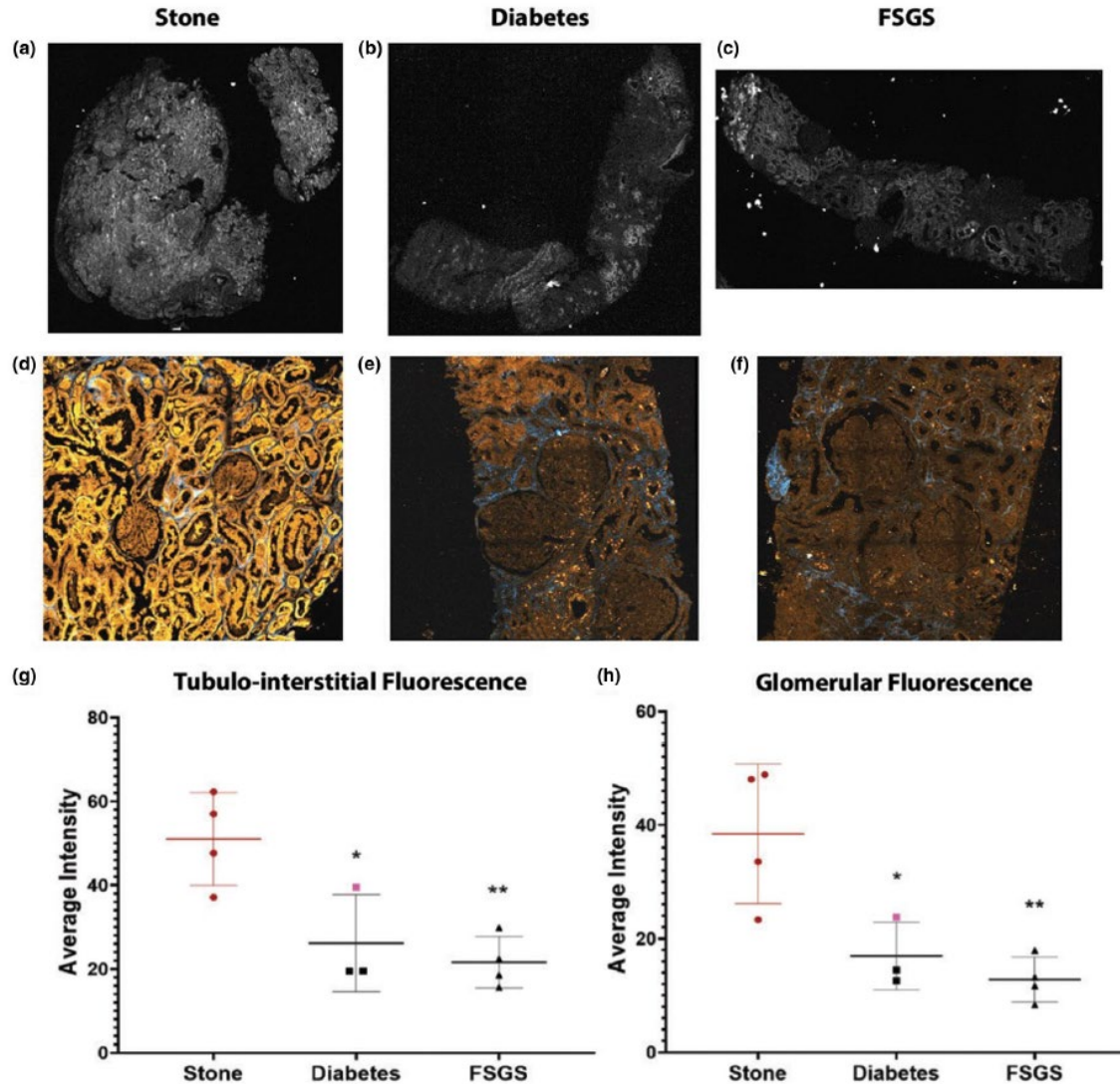


Figure 1.6: Detection of changes in tubulo-Interstitial and glomerular endogenous fluorescence during disease. a–c) The analysis of tubulo-Interstitial endogenous fluorescence was conducted on images obtained in the GFP channel (epifluorescence imaging), as shown previously in Figure 2. d–f) Glomerular analysis was conducted on images obtained using two-photon and second harmonic generation imaging. g, h) Show the results from the tubulo-Interstitial and glomerular analyses, respectively. g) Data points represent the average intensity of the whole tissue. (continued on next page)

(Figure 1.6 cont.): h) Data points represent the average intensity of all of the glomeruli combined for each sample. The data point displayed in pink in the diabetes group is from a stone patient that also had history of diabetes. Single and double asterisks denote significant comparison between diabetes or FSGS to the stone reference group, respectively ( $p < 0.05$ ). No difference was observed when comparing diabetes versus FSGS for either tubulo-interstitial or glomerular endogenous fluorescence

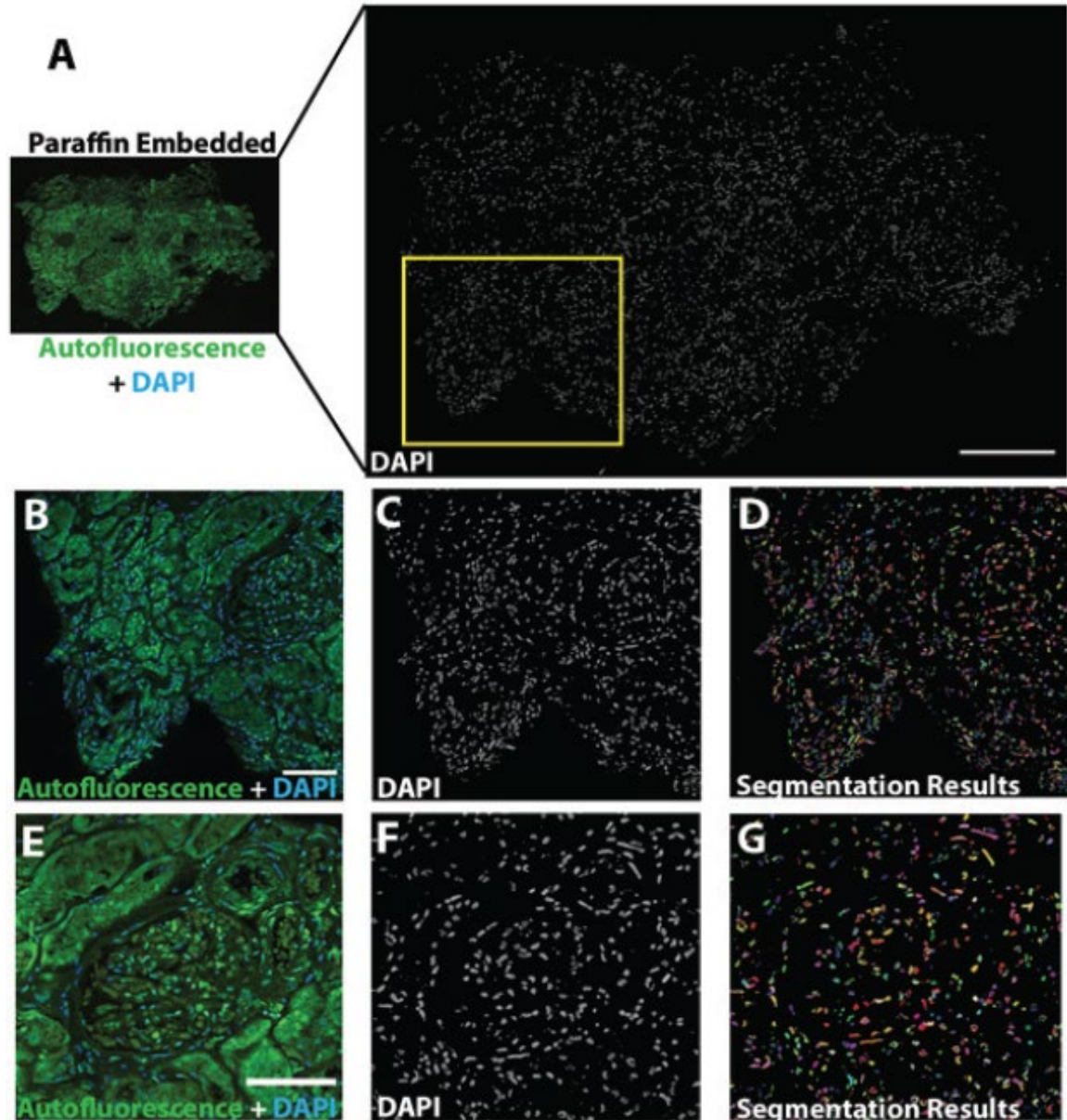


Figure 1.7: Nuclear staining and cytometry can be conducted on paraffin-embedded samples without deparaffinization. a) A non-deparaffinized kidney section (10  $\mu\text{m}$  thickness) was incubated with DAPI and subsequently imaged using confocal fluorescence microscopy. A z-stack spanning the entire thickness was obtained (step size 1 micron). Scale bar = 250 micron. b, c) High magnification region from the yellow box in (a). Scale bar = 150 micron. (continued on next page)

(Figure 1.7 cont.): . d) Segmentation results from tissue cytometry VTEA analysis.

Each color represents an individual nucleus that was segmented. Total count was 11,863 cells for the image volume from (a). e, f) Glomerulus from (b) is enlarged and displayed. Scale bar = 100  $\mu\text{m}$ . g) Segmentation results from VTEA analysis. In total, 141 nuclei were identified in the glomerulus with a density of  $5.5 \times 10^{-4}$  cells/ $\mu\text{m}^3$

## Chapter 2 - Developing a robust analytical pipeline for large scale data

### **Introduction**

Comprehensive tissue interrogation has become an area of interest in numerous organ systems aside from the kidney. Consortia such as the Kidney Precision Medicine Project (KPMP) and the Human BioMolecular Atlas Program (HuBMAP) are dedicated to uncovering and characterizing the cellular components that make up each organ system. For consortia like the KPMP, this analysis is focused on disease states such as AKI, CKD, and/or diabetes. By looking at these diseases, we aim to classify patients based on their molecular pathways as well as identify cells and/or pathways that could be targets for novel therapies (de Boer 2020). Other consortia, like the HuBMAP, are focused on creating healthy reference atlases of numerous different organ systems in order to understand the intricacies of how the human body functions.

Included below are two papers that describes research results within the Kidney Precision Medicine Project. The first details our early work on large-scale image analysis and supervised classification of cells based on antibody staining and intensity using VTEA, a free ImageJ plugin (Ferkowicz 2021). The excerpt from the second manuscript describes work that was conducted to develop the unsupervised learning methodologies within VTEA and apply them to the renal space in order to classify cell types and uncover and characterize the cellular niches (Winfree 2022). These papers are indicated with italic section headers (and for the published paper, used with permission of the publisher; for the paper presently under review, quotations used by permission of the authors).

In the first paper, I was tasked with conducting the glomerular-based analysis shown in Figure 2.7, as well as assisting with the segmentation and analysis of the different biopsies imaged, as shown throughout the entirety of the paper. In the excerpt from the second paper, I was the primary researcher for the CODEX multiplexed imaging. I was heavily involved in the creation of the antibody panel, conjugated antibodies, conducted the experiment, and helped with the initial analysis shown in Figure 2.8 (Winfree 2022)

**2.1 – Large-scale three-dimensional imaging and analysis of the human kidney**  
**(Ferkowicz 2021)**

**Introduction**

For nearly 70 years, histological analysis of biopsy samples has represented the “gold standard” of renal pathology, with clinical diagnoses largely based upon structural changes detected using morphological stains. However, as we enter the era of personalized medicine, researchers increasingly appreciate the need to obtain and quantify additional molecular and genetic information from clinical tissue samples, information that can be used to develop mechanism-based diagnoses and individualized therapies.

Advances in molecular biology have made it possible to collect a rich molecular phenotype of individual samples, even to characterize the genome and transcriptome of individual cells. In the realm of renal research, single-cell “omics” techniques are poised to provide new insights into the mechanisms underlying kidney development, disease and treatment (Malone 2018, Park 2019). However, a general shortcoming of these approaches is that in the process of homogenizing a tissue for cellular analysis one loses

all spatial context, discarding crucial information about the organization of structures and cells in the tissue and the relationships that inform the in-situ behaviors of each cell.

Spatial context is particularly important to understanding cell function in the kidney, whose structure reflects multiple layers of cellular organization. Endothelia and epithelia are organized into sheets that are organized into capillaries and tubules, which are in turn are organized into capillary networks and nephrons whose function is mediated by their organization within the cortex and medulla. This spatial complexity is compounded in the context of disease in which the structure and cellular relationships are disrupted in a time-dependent way, with the additional complication of the local infiltration and activation of immune cells.

An alternative approach is to use multiplexed fluorescence microscopy to characterize the protein or RNA phenotype of cells in fixed tissue sections. Confocal microscopy extends the spatial context of fluorescence studies into three dimensions (3D), which is critical for capturing the structure and inter-relationship of large multicellular structures such as glomeruli and tubules. Whereas light microscopy has traditionally been used to sample representative regions of a tissue sample, automated systems can now be used to collect multiplexed images of entire millimeter-scale samples with subcellular resolution. The analysis of image volumes of this size and complexity is well beyond the capabilities of visual inspection and depends upon advanced methods of digital image analysis that are used to identify and quantitatively characterize each cell, essentially providing a census of every cell in the specimen. The resulting data, which may consist of hundreds of features measured for each of hundreds of thousands of cells,

are then analyzed using methods of multidimensional data analysis to test hypotheses and to identify unforeseen patterns and relationships.

This approach, which we have termed “tissue cytometry” has been used to obtain unique insights into cellular function in lymphatic tissues (Petrovas 2017, Im 2016, Liu 2015, Fonseca 2015, Radtke 2015, Gerner 2015, Gerner 2012), tumors (Lee 2019, Halse 2018), bone marrow (Coutu 2017), and by our group in human and mouse kidney (Winfree 2017, Winfree 2017, Winfree 2018, Micanovic 2018, LaFavers 2019, Makki 2020). Although these studies demonstrate its power, the wide-scale adoption of tissue cytometry as a tool in biomedical research has been limited by the fact that published examples utilize specialized techniques that are beyond the capabilities of most laboratories. Here we describe a complete and accessible pipeline, including methods of sample preparation, microscopy, image analysis, and data analysis for large-scale tissue cytometry of human kidney tissues.

## **Results**

### *Overview of the approach*

The defining goal of our approach is to maximize the information content of images collected from human kidney samples. Each additional parameter improves our ability to unravel the complexity of the kidney, to test hypotheses, and to reveal unforeseen relationships and processes. The need to extract maximum information from each sample is particularly acute for human tissue samples. First, these samples are frequently rare, particularly for specific disease states. Second, human tissue samples incur an ethical responsibility to the donor/patient to justify their sacrifice by extracting maximum information from each precious sample. Thus, we developed a tissue



preparation, imaging and image analysis workflow that provides a quantitative characterization of every cell in an entire 50 micron thick tissue sample with respect to eight different fluorescent probes, tissue autofluorescence, and second-harmonic generation. Described in detail in subsequent sections, the entire process is summarized below and schematized in Figure 2.1.

Cryosectioned samples are first placed in a temporary mount and imaged using multiphoton microscopy to collect high-resolution autofluorescence and SHG images of the entire sample. The section is then removed from its temporary mount and processed for fluorescence labeling with six antibodies, fluorescent phalloidin, and DAPI. The tissue is then mounted permanently on a slide, where it is imaged in its entirety using spectral confocal microscopy. The resulting 16-channel image volume is spectrally deconvolved to discriminate the fluorescence of the eight fluorescent markers. VTEA software is then used to segment the resulting DAPI volume into the individual nuclei of each cell and to quantify the fluorescence in each of the eight channels. VTEA provides scatterplots of the fluorescence associated with each nucleus that can be gated to identify specific cell types, that are then mapped back onto the original image volume. The combination of image maps and scatterplots are then used to interactively explore the image volume. In the following sections, we present an expanded demonstration of this workflow and how it can be used to extract and explore the cellular and molecular constitution of human tissue samples.

#### *Multiphoton microscopy of unlabeled human kidney tissue*

The endogenous fluorescence of tissues is frequently considered an objectionable impediment to immunofluorescence microscopy. However, autofluorescence, arising

from a variety of different molecular sources (e.g., NADH, flavins, porphyrins, collagen, elastin, and lipofuscin) has also been used as a “label-free” approach for characterizing tissue structure and detecting pathologies (Croce 2014, Dong 2010). The fact that tissue autofluorescence can be efficiently stimulated by two-photon processes means that multiphoton microscopy can be used to simultaneously image tissue autofluorescence alongside signals arising from SHG, another label-free imaging modality. The predominant source of SHG signals in biological tissues is fibrillary collagen. Accordingly, SHG has been previously used to detect fibrosis and other pathological alterations of the extracellular matrix (Dong 2010, Ranjit 2016).

Figure 2.2 shows the results of a study in which multi-photon microscopy was used to collect a 3D volume of autofluorescence and SHG signals from a 4 mm by 9 mm, 50 micron thick section of fixed human nephrectomy tissue. Since tissue cytometry requires images collected at a spatial resolution sufficient to distinguish individual nuclei, we employed an approach in which the image volume of the tissue is constructed as a mosaic of smaller image volumes (each ~400 micron across), collected using a  $\times 20$  objective, with a numerical aperture large enough (0.75) to provide subcellular resolution. For each panel of the mosaic, the tissue was illuminated at 910 nm, and two-channel images (SHG and autofluorescence) were collected at 1 micron intervals through the entire 50 micron thickness of the tissue. The process was then repeated across the entire sample, and the resulting volumes stitched together into a single mosaic.

The images of tissue autofluorescence (Figure 2.2 A, D, G) demonstrate that tissue autofluorescence provides structural information sufficient to identify glomeruli and tubules, but also regions of apparent tubular drop out (arrows in Figure 2.2G). The

images of SHG, that largely reflect fibrillary collagen, provide a complementary characterization of the structure of the extracellular matrix, including regions of collagen deposition likely to reflect fibrosis. Interestingly, SHG signals are frequently strong in regions lacking autofluorescence, consistent with the expectation of fibrosis in regions of tubular drop out. Table 2.1 shows the results of quantitative analyses of the autofluorescence SHG images of this and four other nephrectomies, which were used to determine the number of glomeruli and the percentage of the tissue section collected from the cortex (based upon autofluorescence) and the percentage of the tissue area that is fibrotic (based upon SHG).

*Spectral confocal microscopy of human kidney labeled with eight fluorescent probes*

Although the autofluorescence image provides structural information, and the SHG indicates the distribution of fibrillary collagen, a characterization of the cellular constitution of the sample requires immunofluorescence labeling of cell-specific proteins. Thus, after multiphoton microscopy, the tissue was removed from its temporary mount and labeled with eight fluorescent probes. As described in “Methods”, the tissue was processed for immunofluorescence labeling, using antibodies to aquaporin-1 (AQP1, to label proximal tubule cells), THP (to label thick ascending limbs), and CD68, CD3, SIGLEC8, and myeloperoxidase (MPO) (to label macrophages, T cells, eosinophils, and neutrophils, respectively). Following immunofluorescence labeling, the tissue was incubated with fluorescent phalloidin (to label filamentous actin) and DAPI (to label cell nuclei). The tissue was then mounted in a permanent mount and imaged using spectral confocal microscopy and the same 3D mosaic imaging approach described above.

Although the excitation and emission spectra of the fluorescent probes are offset from one another, they nonetheless overlap with one another to varying degrees. In order to selectively distinguish the fluorescence of each probe, we employed an approach in which spectral information obtained separately for each probe was used to “unmix” the images of the combined fluorescence (see “Methods”). In order to capture as much spectral information as possible, the sample was illuminated sequentially at 405, 488, 552, and 635 nm, and four channels of fluorescence were collected for each illumination. This procedure was repeated for each focal plane for each panel of the mosaic, resulting in a rich 16-channel image volume of the tissue that was then spectrally deconvolved, using linear unmixing, to distinguish the eight different fluorescent probes.

Figure 2.3 shows how the addition of probes to detect filamentous actin, THP and AQP1 augments the information provided by autofluorescence and SHG. As expected, fluorescent phalloidin strongly labeled the filamentous actin of the vasculature, glomerular capillaries, basement membranes and tubule brush borders. The magnified images shown in Figure 2.3D-I demonstrate that AQP1 immuno- fluorescence correlates well with the phalloidin fluorescence of the brush borders of proximal tubule cells. In contrast, immunolabeling for THP identifies a distinct set of tubules of the thick ascending limb, but also strongly labels structures in tubule lumens that appear to be tubular casts. Interestingly, regions showing strong SHG fluorescence and amorphous phalloidin labeling correlate with regions lacking immunofluorescence (indicated with arrows in Figure 2.3G, H, I), consistent with the loss of tubular markers in fibrotic regions.

### *3D tissue cytometry of human kidney*

Figure 2.4A shows a projection of the same tissue volume shown in Figure 2.3C, with the addition of the nuclear fluorescence of DAPI and the immunofluorescence detected for CD68, CD3, and MPO (labeling macrophages, T cells, and neutrophils, respectively). Although several interesting patterns are apparent in the figure, it is clear that the richness of the data in this  $9800 \times 19,800 \times 50$  voxel, 8-probe image volume exceeds our ability to evaluate it visually. In order to fully explore and discover meaningful patterns in an image of this scale and complexity, the image must be converted into quantitative data.

Quantification of large-scale three-dimensional images of tissues has been conducted using an approach that has been variously termed histo-cytometry (Gerner 2012, Li 2017), 3D confocal cytometry (Coutu 2017), 3D imaging cytometry (Lee 2019), and tissue cytometry (Winfree 2017, Winfree 2017, Winfree 2018). Conceptually similar to flow cytometry, tissue cytometry is based upon the detection and attribution of immunofluorescence signal levels to individual cells, providing a multiparameter analysis of a cell population. However, as it is based upon fluorescence measurements detected as a laser scans over a tissue, tissue cytometry provides this information along with the spatial location of each cell, as demarcated by methods of digital image analysis (segmentation). The combination of large-scale microscopy with automated methods of digital image analysis transforms microscopy from a tool for characterizing sample regions into one providing a census of every cell in a tissue sample.

While a variety of software tools have been developed to support quantitative analysis of two-dimensional images, few have been developed for the analysis of large-

scale 3D image volumes. Moreover, none integrate all of the necessary tools of image processing, segmentation, quantification, and data analysis into a single package. We developed VTEA in response to the need for an accessible, yet powerful solution to 3D tissue cytometry. Developed as a plug-in for the widely-used ImageJ freeware, VTEA organizes each of the steps of tissue cytometry into a bidirectional workflow that facilitates interactive exploration and analysis of complex, 3D image volumes.

VTEA tissue cytometry is based upon a strategy in which each individual cell is identified by its fluorescently- labeled nucleus and then characterized by quantification of the immunofluorescence of the cell markers in the region immediately surrounding the nucleus. A 3D watershed segmentation of the nuclei in the image shown in Figure 2.4A identified 248,050 nuclei from the 1.7 mm<sup>3</sup> volume of the tissue, each of which is depicted in a different color in Figure 2.4B. Although difficult to discern in this image, the tissue includes several high-density regions, which are shown in a density plot in the inset. Some of these regions are associated with regions of immune cell infiltrates that are apparent in the original image (indicated with arrows in Figure 2.4A).

The nuclear segmentation is used to define regions that are used to quantify nuclear fluorescence, and in the region immediately surrounding the segmented nucleus, the fluorescence of each of the eight fluorescent probes following linear unmixing. VTEA presents these data in csv files, as well as in interactive scatterplots that can be used to visualize the distributions of values any two measurement parameters along the x and y axes (Figure 2.4F, G). In order to extend the dimensionality of these scatterplots, each point can be rendered in a color representing the value of a third measurement parameter of the user's choice.

The VTEA scatterplots can be used to identify specific cell types in fluorescence images in an approach similar to that used by FlowJo to identify cells in flow cytometry analyses of suspended cells. Like FlowJo, VTEA provides the user with a tool to draw “gates” on the scatterplots to identify specific cell types based upon the levels of fluorescence of specific cell markers. Figure 2.4F shows examples of gates drawn onto a scatterplot of AQP1 and THP fluorescence to define cells of the proximal tubule and thick ascending limb, respectively. This gating procedure is repeated for each of the cell markers to identify each cell type and the resulting gated data is used by VTEA to generate a new version of image in which the identity of each cell is mapped onto its nucleus in a unique color. Figure 2.4C shows the results of scatterplot mapping of different cell types based upon gating the fluorescence levels obtained from the image shown in Figure 2.4A. Figure 2.4H, I show the results of gating the magnified sub-regions shown in Figure 2.4D, E, respectively. In these examples, the fluorescence of antibodies against THP, AQP1, MPO, CD68, and CD3 was used to identify cells of the thick ascending limb, proximal tubule, neutrophils, macrophages, and T cells, respectively. The fluorescence of phalloidin was used to detect cells rich in F-actin, primarily cells of the glomeruli and peritubular capillaries. As this mapping is immediately updated as gates are adjusted, it provides an effective method for visually validating the gating strategy. As the gated cells are rendered in a single, bright color, the mapped image also serves to more clearly delineate the distribution of dimly-labeled cells (e.g., CD3+ cells).

VTEA’s scatterplot functions are crucial to accurate identification of specific cell populations in highly multiplexed image volumes. The quantitative analysis and gating

procedures described above were conducted on fluorescence data following linear unmixing which, as described above, was used to distinguish the fluorescence of each individual probe from the combined spectrum of the eight fluorescent probes. Although linear unmixing is effective for distinguishing probes whose fluorescence levels are similar, it frequently fails to completely eliminate crosstalk of strong signals into the spectral channels used to detect weaker signals. In the samples analyzed here, the fluorescence of the THP probe was much stronger than the other probes. However, VTEA scatterplot tools can be used to selectively identify cells whose target probe signals are contaminated by fluorescence crosstalk by the intense THP signal. For example, the crosstalk from THP cells with high signal spilling into the AQP1 channel can be parsed out by plotting AQP1 vs. THP (Figure 2.4F). VTEA's ability to represent a third dimension of data in 2D scatterplots using color can also be used to isolate the effect of crosstalk. In Figure 2.4G, color is used to represent AQP1 fluorescence. When viewed in this way, the cells whose CD68 signal derives from AQP1 crosstalk are immediately apparent, and easily excluded from the "true" CD68+ gate.

The data derived from VTEA analysis of this volume are summarized in Table 2.1, along with those from four other nephrectomy tissue samples. The degree of fibrosis varied between a minimum of 7.7 to a maximum of 12.3% of total areas. As expected, the distribution and abundance of tubular cells varies depending on various renal areas sampled (cortex vs. medulla). Interestingly, there was a consistent immune cell infiltration in all the specimens imaged, distributed in a focal pattern within each tissue. The average number of immune cells (reported as % of total cells) were:  $2.1 \pm 0.9$ ,  $0.3 \pm 0.1$ , and  $5.0 \pm 2.2$ , for neutrophils, inflammatory macrophages, and T cells, respectively.



Multiplexed analysis of tissues at this scale offers unique benefits. First, the extended volume of sampling increases the likelihood of detecting rare events. The scale of the image is sufficient to detect multiple highly-localized foci of inflammation, which may be missed when surveying a small area of tissue. More significantly, the ability to conduct a multiparametric analysis of multiple events provides the opportunity to identify meaningful correlations that might otherwise be missed. For example, four regions of inflammation are indicated in Figure 2.5A, each with a different constitution of T cells (white) and neutrophils (red) (Figure 2.5B–E). While the underlying basis of these differences is unknown, an evaluation of the corresponding immunofluorescence, autofluorescence, and SHG images suggests that they may reflect regions at different stages of inflammation, associated with various degrees of fibrosis (increased SGH density), and tubular drop-out (loss of autofluorescence, AQP1, and THP immunofluorescence). While this interpretation may be speculative, it demonstrates how an image of an entire tissue might provide a snapshot in time of multiple regions of injury, each at a different stage, and how a multiparameter analysis might be used to understand the progression of injury.

#### *Application of large-scale 3D tissue cytometry to kidney biopsies*

Figure 2.6 shows an example of one of the most exciting applications of tissue cytometry—the analysis of clinical biopsy samples, in this case kidney core biopsies obtained from patients diagnosed with diabetic nephropathy. Label-free imaging uncovers the structural make-up of the biopsies (glomeruli, tubules, renal capsule, etc.) and the associated area of collagen deposition through SHG. Spectral confocal imaging and results of tissue cytometry with VTEA are shown in Figure 2.6 and Table 2.2,

respectively. In the example shown, we can infer an advanced degree of fibrosis, which corresponds to the advanced clinical disease of the patients (CKD stages 3 and 4).

Although it may be premature to derive meaningful conclusions from this small sample size, the analysis already underscores the heterogeneity of diabetic kidney disease and the presence of active foci of inflammation with neutrophil and macrophage infiltration even in advanced disease. Other observations of interest are the change in structural markers, especially THP, which is significantly decreased compared to reference tissue with comparable amount of cortical tissue (samples 1, 2, and 4, Table 2.1): THP+ cells (%):  $0.2 \pm 0.2$  vs.  $6.1 \pm 1.9$ , respectively ( $p = 0.03$ ). The absence of T cells is also noted ( $P < 0.05$  compared to reference tissue) and needs to be validated in a larger series.

Figure 2.7 shows a specific example of how tissue cytometry can be used to study the cellularity of glomeruli, a key site of pathology in diabetic kidney disease. Compared to reference tissue, where the range of glomerular cellular density is consistent, diabetes induces an increase in glomerular cellular density in many but not all the studied biopsy specimens (Figure 2.7A). Interestingly, cellularity remains homogeneous within each specimen, suggesting that glomerular pathology induced by diabetes is global and not focal in nature. Furthermore, diabetes does not increase immune cell infiltration of glomeruli, as shown in Figure 2.7B.

## **Discussion**

Here we have demonstrated an accessible approach to tissue cytometry, a technique that is increasingly used to analyze and understand the complex biology of human and animal tissues. As compared with traditional methods of histology,

fluorescence-based tissue cytometry offers several advantages. First, the fluorescence modality is compatible with confocal or multiphoton microscopy, which can be used to collect 3D image volumes, providing unique structural information, more accurate representations of spatial relationships and a more accurate and extensive census of cells in a tissue. Second, fluorescently-labeled antibodies, lectins and toxins can be used to provide molecular specificity, which supports enumeration of specific cell types and structures. Third, fluorescence supports multiplexing, which can be used to detect multiple cell types, and thus their interactions, in the same tissue. Finally, quantitative methods of digital image analysis are more fully developed and implemented for the analysis of fluorescence images, facilitating automated analysis of large and complex image volumes.

The nascent field of tissue cytometry developed naturally (and inevitably) from the development of methods for large-scale, high-content, and high-resolution imaging. The automation of confocal microscope systems gave researchers the capability to collect fluorescence images of centimeter-scale samples at submicron resolution. The development and implementation of methods of tissue clearing extended the depth of image volumes from tens of microns into the range of millimeters. Whereas once confocal image volumes might consist of the fluorescence of two or three probes, new laser systems and methods of spectral deconvolution now enable researchers to simultaneously resolve seven or more probes in the same sample.

The scale and complexity of these image volumes presents both an opportunity and a challenge. Capable of providing rich molecular data for entire tissue biopsies, tissue cytometry can transform fluorescence microscopy from a tool used to qualitatively

characterize “representative fields” into a tool for generating a quantitative, multi-parameter census of every cell in a tissue. However, tissue cytometry is still a developing field—effectively extracting information from such large and complex image volumes depends upon developing methods of microscopy optimized for quantitative analysis, methods of image analysis suited to quantitatively characterizing individual cells in a tissue and methods of data analysis that can be used to explore, and ideally, discover unforeseen patterns in the data. Thus, tissue cytometry remains a tool that is utilized by relatively small number of laboratories with particular skill in quantitative microscopy.

Here we have presented a straightforward workflow for tissue cytometry based upon commonly used methods of tissue processing, microscopy techniques that can be implemented by nearly all commercially- available confocal microscope systems, and an image and data analysis workflow based upon the easy-to-use VTEA freeware that we developed as a plug-in for ImageJ. We specifically show how this approach can be used to study human kidney tissue both in nephrectomy reference tissue and from kidney biopsies from patients with diabetes.

Although we have described a workflow that is specific in its details, tissue cytometry is a highly flexible research tool that is compatible with a variety of different methods of tissue preparation and fluorescence microscopy. Our approach is based upon analyses of OCT-frozen tissue cryosections. While frozen tissues are common to research laboratories and tissue banks, a rich repository of clinical samples are embedded in paraffin. Such samples are compatible with immunofluorescence once “deparaffinized” by treatment with organic solvents. This approach was used in recent studies in which quantitative multiplexed immunofluorescence was used to analyze human tumor biopsies

(Lee 2019, Halse 2018). These studies demonstrate the exciting potential of tissue cytometry as a tool for extracting new data from archived clinical samples. Cellular and molecular data obtained from tissue cytometry could be combined with corresponding clinical data to provide unique insights into disease and therapy. However, the potential large-scale studies of this kind will critically depend upon the quality and consistency of the clinical samples.

For our studies, tissue samples were cut to a nominal thickness of 50 micron, a thickness that could be rapidly labeled and imaged, and yielded substantial amounts of high-quality data. However, spatial scale of tissue cytometry can be significantly increased through the use of “tissue clearing” techniques that extend the depth of fluorescence microscopy by reducing light scatter. Tissue cytometry has been applied to cleared tissues to characterize cell populations in tissues samples that are hundreds of microns thick (Lee 2019, Coutu 2017, Li 2017). While tissue clearing significantly extends the scope of fluorescence imaging, it does so at the cost of time. First the process of tissue clearing typically requires days in itself. Second, extending the thickness of tissues extends the time required for all incubations as well as the time required to collect image volumes.

The process of collecting multiplexed fluorescence images required 24–36 hours per sample, largely due to the inherently slow process of single-point scanning confocal microscopy. Alternative modes of microscopy could be used to accelerate image capture. For example, microscope systems such as spinning-disk confocal and light-sheet microscopes speed the process of image capture by collecting images of entire fields in a matter of milliseconds. A light-sheet microscope system, modified to accommodate the

geometry of tissue sections on slides, was demonstrated to be capable of collecting a 1 mm<sup>3</sup> volume in <1 min (Glaser 2019). Another alternative is the “ribbon-scanning” confocal microscope system, which uses a high-speed resonant scanner to continuously scan a sample as the stage translates through the sample. A commercially available system was recently demonstrated that could scan a two-channel image of an entire 1 mm<sup>2</sup> field in <3 min (Watson, 2017). The impressive speed advantage of the light-sheet and ribbon-scanning systems is reduced somewhat for studies involving more than one or two probes, since collection of additional channels requires repeated, time-consuming filter changes (for the light-sheet system) or additional stage scans (for the ribbon-scanning confocal).

In order to glean as much information as possible from each sample, we first used multiphoton microscopy to acquire autofluorescence and second-harmonic images of unlabeled tissue, and then used confocal microscopy to acquire 8-channel fluorescence images following labeling with fluorescent probes. Multiphoton-excited autofluorescence and SHG have previously been used to analyze mouse experimental mouse models of kidney injury (Strupler 2008), and to characterize unlabeled human bladder biopsies (Jain 2012), human prostate (Tewari 2011), and human colorectal cancer (Matsui 2017). However, we are unaware of studies in which multiphoton microscopy of unlabeled tissue was followed by confocal microscopy of the same tissue following fluorescent labeling. Imaging the same tissue before and after labeling is complicated by the need to manipulate the sample between the two image collections. In our protocol, the unlabeled tissue was removed from the temporary mount for fluorescent labeling, subsequent confocal imaging was conducted after the tissue was mounted a second time. The process

of tissue incubation and remounting introduced small changes in the overall shape of the tissue, so that the multiphoton and confocal images were only approximately registered with one another, compromising our ability to include autofluorescence and SHG data in the VTEA cytometry analysis. We have since developed a new technique whereby tissues are fluorescently labeled while still mounted on the slide, eliminating the misregistration of multiphoton and confocal fluorescence images. Doing so will increase the data space of each cell in the tissue so that it includes not only the 8 fluorescent probes, but also the autofluorescence and SHG associated with each cell.

Multiplexed fluorescence microscopy is complicated by the extensive overlap in the excitation and emission spectrum of fluorescent probes, which limits the discrimination of any single fluorophore in a multi-labeled sample. Imaging up to three or four probes can be accomplished by judicious choice of optical filters. However, distinguishing additional fluorescent probes typically requires spectral deconvolution of fluorescence images, particularly in the presence of tissue autofluorescence. In our studies, we used linear unmixing to discriminate eight fluorescent probes. We found that linear unmixing was frequently only partially successful in removing the strong fluorescence of the probes used to detect AQP1 and THP from that of probes used to identify immune cells. Whereas residual signal contamination would ordinarily be difficult to detect and correct, we describe how VTEA's scatterplot tools simplify the process of discriminating cell populations in the presence of signal crosstalk. The VTEA scatterplots can also be used to identify signal saturation, an issue that is frequently encountered due to between-sample variability, and compromises the signal linearity that is prerequisite to linear unmixing.

The problem of spectral crosstalk in multiplexed imaging can be avoided in two ways. First, a number of techniques have been developed whereby highly multiplexed fluorescence images are assembled from a sequence of images of tissues labeled with between one and three probes at a time. In this approach, following imaging, the first set of probes are removed (Golstev 2018, Agasti 2017, Wang 2017, Wahlby 2002) or their fluorescence is quenched (Hillert 2016, Schubert 2006, Lin 2015, Gerdes 2013) the sample is labeled with a new set of probes, and the tissue is imaged again. As this process is repeated, highly-specific images of 50 or more different antigens can be collected from the same tissue sample. The second approach to avoiding spectral crosstalk is to abandon fluorescence as the source of image contrast. Imaging mass cytometry uses heavy metal isotopes to label antibodies, which are then used like fluorescently-labeled antibodies to label tissues. The isotopes are detected using mass spectrometer following ablation of the tissue with either a laser (Giesen 2014) or ion beam (Angelo 2014). Using isotopes with appropriately distinct mass-to-charge ratios, images of more than 30 probes can be collected with subcellular resolution (Giesen 2014). The major drawback of sequential fluorescence and imaging mass cytometry is that neither is compatible with tissues more than a few microns in thickness, limiting their ability to characterize tissues in 3D.

Perhaps the most challenging aspects of tissue cytometry are those involved with extracting and exploring the complex data obtained from large multiplexed 3D image volumes. In most published examples of 3D tissue cytometry (Petrovas 2017, Im 2016, Liu 2015, Fonseca 2015, Radtke 2015, Gerner 2015, Gerner 2012, Lee 2019, Moreau 2012), image analysis is first conducted using combinations of custom-designed and commercial software, and the resulting data are then exported to Excel and/or FlowJo for



data analysis. The Schroeder laboratory developed an alternative approach, in which images are first segmented using Imaris, and then analyzed using the custom-designed XiT software which provides additional capabilities for image quantification and data exploration (Coutu 2018). We developed VTEA in response to the need for powerful, yet accessible software that incorporates the entire image and data analysis into a single platform. This design provides a seamless bidirectional conduit between the image and data space, facilitating refinement of image analysis, interactive exploration of image data and discovery of unique patterns and associations. Insofar as VTEA is an evolving platform that is continuously being refined and extended, the version demonstrated here represents only a fraction of the capabilities that we will have incorporated into the version available at the time of publication. In addition to the features demonstrated here, the new version will provide tools for [1] analysis of structural features [2], analysis of spatial relationships and [3] unsupervised analysis of multiplex data.

In conclusion, we provide a complete workflow to perform large-scale 3D imaging and tissue cytometry on human kidney tissue, which could be used to extract “big data” type spatial information from kidney biopsies from patients with kidney disease. We showed examples of how such analyses can provide useful insights that can be linked to the biology or pathology of kidney disease. We anticipate that this imaging and analytical approach will complement other Omics type outputs and could help spatially map pathological changes that occur with kidney disease.

## **Methods**

Reference kidney samples (from tumor-free regions of nephrectomies or deceased donors) were obtained from the KPMP (Kidney Precision Medicine Project,

<https://kpmp.org>) and diabetic nephropathy biopsy specimens were obtained from the Biopsy Biobank Cohort of Indiana. This study was approved by the Institutional Review Board of Indiana University. The diabetic nephropathy biopsies were indicated because of rapidly progressing kidney disease and the patients were at stage 2 or 3 CKD at the time of biopsy with nephrotic range proteinuria.

#### *Sample sectioning for multiphoton and confocal microscopy*

Fresh-frozen human kidney samples are placed in cold Optimal Cutting Temperature (OCT) compound for 3 min and then transferred to a cryomold with partially frozen OCT in the bottom on a block of dry ice. Once the OCT is completely frozen, the tissue block is wrapped in parafilm and stored at  $-80^{\circ}\text{C}$ . Frozen tissues are sectioned to a thickness of 50 micron using a cryostat and then immediately fixed in 4% fresh PFA for 24 h, and subsequently stored at  $4^{\circ}\text{C}$  in 0.25% PFA.

#### *Multiphoton microscopy*

The imaging strategy described here consists of two steps. Multiphoton microscopy is first used to collect auto- fluorescence and second-harmonic images of the unlabeled tissue. The tissue is then labeled with fluorescent compounds and antibodies and confocal microscopy is used to collect multiplexed images of the fluorescent labels. Since fluorescence labeling was accomplished with the tissue suspended in a solution, this sequential approach required that multiphoton microscopy be conducted on unlabeled tissue mounted in a temporary mount from which the tissue could be easily removed. Accordingly, multiphoton microscopy was conducted on tissues that were rinsed in PBS and temporarily mounted in a nonhardening mounting medium on low-charge slides and sealed via removable rubber cement sealant.

Both multiphoton and confocal microscopy were conducted using a Leica SP8 confocal scan-head mounted to an upright DM6000 microscope with computer-controlled motorized stage. In order to collect images of entire millimeter-scale tissues at submicron resolution, the Leica Tile Scan function was used to collect a mosaic of smaller image volumes using a high-power, high-numerical aperture objective. The Leica LASX software was then used to stitch these component volumes into a single image volume of the entire sample. The scanner zoom and focus motor control were set to provide voxel dimensions of 0.5 by 0.5 micron laterally and 1 micron axially.

Multiphoton excitation microscopy was conducted using a  $20 \times 0.75$  NA Leica multi-immersion objective (adjusted for water immersion), with excitation provided by a MaiTai DeepSee tunable titanium-sapphire laser (Spectra Physics, Santa Clara, CA) adjusted to 910nm. The descanned pathway was configured for multiphoton imaging by fully opening the confocal pinhole and adjusting photomultiplier detectors to collect emissions from 439 to 465nm (for SHG) and from 473 to 497 nm (for autofluorescence).

#### *Fluorescence labeling for confocal microscopy*

Following multiphoton microscopy, the temporary mount is dismantled, and the unlabeled tissue is carefully retrieved for fluorescence labeling. The tissue is washed in PBS for 10min and placed in blocking buffer (PBS with 0.1% Triton X-100 (MP Bio-medical) and 10% Normal Donkey Serum (Jackson Immuno Research)). The tissue is gently rocked for 4–8 h at room temperature after which it is placed in 200 microliters of a solution containing antibodies to be used for indirect immunofluorescence (AQP1, MPO, CD68, and SIGLEC-8) and rocked for 8–16 h at room temperature. The tissue is then washed in two changes of 2 ml of PBST (PBS with 0.1% Triton X-100) over 6 h,

and placed in blocking buffer. After 4–8 h of gentle rocking at room temperature, the tissue is then incubated in the panel of secondary antibodies. Following an 8–16 h incubation the tissue is washed in two changes of 2 ml of PBST over 6 h, and placed in blocking buffer for 4–8 h. The tissue is then incubated at room temperature in 200 microliters of a solution containing the directly-labeled antibodies (THP, CD3) as well as DAPI and OregonGreen phalloidin. After 8–16 h in this solution, the tissue is washed in two changes of PBST over 6 h and mounted in Prolong Glass (Thermo Fisher) on acid-cleaned slides.

#### *Confocal microscopy of labeled tissue*

Confocal microscopy was conducted using a Leica 20× 0.75 NA multi-immersion objective (adjusted for oil immersion), with excitation provided by a solid state laser launch with laser lines at 405, 488, 552, and 635 nm. A total of 16 images is collected for each focal plane of each panel of the 3D mosaic. The sample is first illuminated at 405 nm, and the four confocal detectors (two PMT, two HyD) adjusted to collect 410–430, 430–450, 450–470, and 470–490 nm emissions. The sample is then illuminated at 488 nm and the confocal detectors adjusted to collect 500–509, 510–519, 520–530, and 530–540 nm emissions. The sample is then illuminated at 552 nm and the confocal detectors adjusted to collect 570–590, 590–610, 610–630, and 631–651 nm emissions. Finally, the sample is illuminated at 633nm and the confocal detectors adjusted to collect 643–664, 664–685, 685–706, and 706–726 nm emissions. The resulting 16-channel image is then spectrally deconvolved (via linear unmixing, as described below) to discriminate the eight fluorescent probes in the sample.

### *Spectral deconvolution*

The excitation and emission spectra of many of the fluorescent probes used in these studies overlap with one another. In order to discriminate each of the 8 fluorescent probes, the 16-channel images were spectrally deconvolved using the Leica LASX linear unmixing software. The unmixing matrix is derived from 16-channel reference images of singly-labeled samples (tissue labeled with DAPI or OregonGreen alone, or samples containing microspheres (Thermo Fisher, cat# C37253) labeled with one of the fluorophores used for immunofluorescence.) Spectral deconvolution results were validated by collecting 16-channel images of three samples containing 6 different fluorescently-labeled microspheres in different known proportions, and then comparing the numbers of microspheres identified by linear unmixing with the numbers expected based upon their known proportions. Regression of the pooled results indicated an excellent agreement between the observed and expected counts and a G-test of independence detected no significant difference ( $P = 0.98$ ).

### *Quantitative image analysis—tissue cytometry*

All tissue cytometry was conducted using the Volumetric Tissue Exploration and Analysis (VTEA) software. VTEA is unique 3D image processing workspace that was developed by our group as a plug-in for ImageJ (Winfree 2017). Compatible with essentially any personal computer system, VTEA can be obtained using the ImageJ updater system as described at <https://imagej.net/VTEA>. The details of VTEA's operation and utility are described in more detail in the Results section. Validation of the gates drawn on the analytical scatterplots was performed by visual mapping of the gated cells over the image volume and kept constant between specimens in the particular study. Cell

density isomaps (e.g., Figure 2.4B) were generated in R using ggplot. Tissue volumes were quantified as the product of the lateral dimension of the tissue (quantified in FIJI) multiplied by the mean depth of the tissue, as measured by the distance between the first and last sections containing at least one segmented nucleus.

#### *Image processing for figures*

As described above, mosaic image volumes were assembled using the Leica Suite X software. Quantitative analysis was conducted using raw image data, but micrograph images presented in figures were contrast enhanced in a way that preserved the visibility of both the dim and bright structures of the original images. Images in figures were processed, assembled and annotated using Adobe Photoshop.

#### *Statistics*

When applicable, average values are reported  $\pm$  standard errors. Two-tailed Student's t tests were used as tests of significance.

### **2.2 Excerpt from: Integrated cytometry with machine learning applied to high-content imaging of human kidney tissue for in-situ cell classification and neighborhood analysis (Winfree 2022)**

#### **Introduction**

Renal researchers increasingly appreciate the importance of characterizing the cellular niches of the kidney (cell types and subtypes, physiological state, neighborhood interactions) and how they are altered in kidney disease (Anders 2011, Chessa 2016, Winfree 2021, Lake 2021). Imaging of kidney tissue specimens with single-cell resolution at a large scale is an attractive approach for uncovering cellular niches in their tissue context (Ferkowicz 2021, Neumann 2021, Ferreira 2021). Such an approach has

become more feasible because of the increased ability to collect mesoscale imaging datasets on accessible confocal microscopes, whole slide imagers and light-sheet microscopes. Furthermore, combining mesoscale imaging with highly multiplexed staining or labeling approaches allows for the capture, in situ, of hundreds-of-thousands cells that may be classified by many markers. The scale and depth of these data create a mounting challenge for timely quantitative and interpretable analysis. This is particularly important for kidney research, where biopsy-scale multiplexed imaging datasets of the human kidney are being collected and publicly released by large collaborative consortia such as the Kidney Precision Medicine Project (KPMP) and the Human BioMolecular Atlas Program (HuBMAP) (El-Achkar 2021, HuBMAP Consortium 2019).

Tissue cytometry (TC) is a powerful approach for analyzing mesoscale fluorescence images with single-cell resolution (Ferkowicz 2021, Winfree 2017, Stolzhus 2020, Li 2017, Gerner 2012). Depending upon the imaging platform, datasets may be either 2D or 3D (Winfree 2017, Golstev 2012). An important first step in TC is to survey all the cells by segmentation. This is often accomplished by using nuclei as fiducials for cells. Segmentation entails identifying regions of images as nuclei based on contrast provided by stains, registering each individual nucleus as an object, and identifying an associated cytoplasm spatially or with a specific marker. Features to describe these cells can be calculated on this segmentation. These features could be related to fluorescence intensities of markers within or around the nucleus (i.e. the cytoplasm) or based on the spatial coordinates or proximity relationships to these nuclei (Winfree 2017, Gerner 2012, Golstev 2018). Multiplexing several markers in the same experiment enhances the richness of the imaging data, by providing specificity of cell types based on unique

markers (or unique combination thereof) and generating spatial information based on the distribution of stains within the tissue (Ferkowicz 2021, Gerner 2012, Golstev 2018, Lin 2018).

In a standard cytometry analysis, after cell segmentation, cells can be classified and quantitated by supervised approach using gating based on marker intensity, in which cells are defined according to threshold levels of marker fluorescence (gating). However, as the scale and complexity of multiplex mesoscale image volumes increase, such a manual approach becomes intractable and increasingly unlikely to be successful at uncovering the complex spatial organization and cellular niches of the kidney. Multiplexed mesoscale tissue cytometry thus requires tools supporting unsupervised analysis, ideally with machine learning, to characterize the cellular makeup of a tissue accurately and completely, to identify cellular niches and to map their neighborhoods and microenvironments (Stoltzfus 2020, Golstev 2018, Jackson 2020, Shurch 2020, Stoltzfus 2021). Given the complexity of the interacting processes of segmentation, classification, quantification and neighborhood analysis, the ideal system should incorporate all these processes into a single, integrated analysis and visualization software package.

Since the initial description of VTEA as an open-source project, several excellent tools for tissue cytometry have been developed. In this time VTEA (v0.5.2-v0.7) has been used in several projects involving single imaging fields to large mesoscale multi-fluorescence kidney image volumes to perform supervised cytometry analysis with gating (Lake 2021, Ferkowicz 2021, Black 2021, Black 2021, Varberg 2017, Makki 2020, Woloshuk 2021, Micanovic 2021). However, machine learning, data visualization and analysis tools that are useful for multidimensional, big-data scale imaging data were not



previously implemented in VTEA's uniquely integrated pipeline. Here we describe VTEA 1.0 which specifically adds, 1) machine learning for clustering and dimensionality reduction to aid in automated classification of cell types, 2) neighborhood analysis to uncover cellular niches and 3) new data visualization tools to support discovery. To facilitate this growth of VTEA's integrated approach, a SciJava framework was implemented (Rueden 2021, Schindelin 2012). VTEA now supports extensible image processing, segmentation, classification, visualization, and neighborhood analysis for processing on hundreds-of-thousands of cells and multi-gigabyte datasets with a fully integrated workflow. We demonstrate the utility of VTEA by identifying cell subtypes based on labels, spatial association and neighborhood membership using large scale 3D and 2D imaging data from kidney tissue.

## Results

*Applying VTEA's pipeline on highly multiplexed CODEX data of the human kidney to uncover cell sub- types and biologically relevant cell neighborhoods*

Human cortical biopsy underwent CODEX imaging with 23 markers (Figure 2.8A, Table 2.3) and analyzed with VTEA to perform cytometry, cell-classification, and neighborhood analysis (Figure 2.8B-E). Unsupervised hierarchical clustering of the 11,355 segmented cells identified the major cell types in the kidney (Figure 2.8B). Using subgating and subclustering, additional novel cell state phenotypes were identified including PROM1-positive (CD133) thick ascending limb and proximal tubule cells (Figure 2.8B, and 2.9D) and CD68-positive dendritic cells, CD68-positive putative macrophages, and CD68- positive epithelial cells (Figure 2.8C and 2.9C-E). To determine if specific cellular microenvironments were present in the tissue, VTEA's

neighborhood analysis function was used to tabulate neighborhoods and revealed, after clustering and dimensionality reduction, unique neighborhoods with associations between tubular epithelial cell subtypes and immune cells, such as the association of PROM1-positive TAL and PROM1-positive PT cells with low levels of CD68-positive macrophages (Figure 2.8D and E, N4 and N5 respectively) and an association of CD90-positive proximal tubules with DC and T-cells (Figure 2.8E, N6).

## **Discussion**

In this work, we present an integrated tissue cytometry approach with VTEA to analyze and extract biologically relevant data from state-of-the-art and increasingly multiplexed fluorescence imaging datasets of human kidney tissue. This approach leverages innovative tools for analysis and visualization using machine learning to perform rigorous, reproducible, and informative analysis that could be used to uncover the complex spatial organization and cellular make-up of the human kidney. Using this analysis pipeline, we demonstrated how we can improve the accuracy and resolution of cell classification in kidney tissue. Furthermore, we showed unique advantages of this approach in performing advanced quantitative analysis to uncover cell populations based on spatial associations and neighborhood memberships. In addition, VTEA has the tools to perform intuitive analysis on highly- multiplexed datasets and extract novel information on cell subtypes and neighborhoods that could complement findings from other omics studies at the single cell level. VTEA is available for download through the FIJI plugin updater with the source code is available on github, <https://github.com/icbm-iupui/volumetric-tissue-exploration-analysis>. Additional description and vignettes demonstrating the use of VTEA are available at <https://vtea.wiki>.

One of the advantages of incorporating machine learning and dimensionality reduction in the VTEA workflow, as compared to relying only on one label of interest to identify cells, is the ability to use information from the other label intensities and potentially additional spatial parameters. These added parameters increase the discriminative power to identify specific population of cells such as better identification of low intensities of a specific marker. These applications will improve the accuracy compared to a standard gating strategy and increase the confidence of identifying novel cells that may be biologically relevant, as we showed for low AQP2 expressing cells in the distal nephron.

In addition to improving the accuracy and resolution of cell classification, the workflow of VTEA with machine learning tools will facilitate the cytometry analysis of imaging data that was not previously feasible using a standard VTEA approach. We present examples of spatially overlapping cells within structures like glomeruli. Taking advantages of multiple dimensions, it is possible now to accurately quantify the various cell types within glomeruli. This process could also be semi-automated using the data analytical tools provided, thereby having important potential implications on studying human glomerular pathology, where the cell density of specific cell types such as podocyte, immune and mesangial cells may be linked to the pathogenesis of kidney disease (Ferkowicz 2021). We also demonstrated the utility of VTEA in classifying cells based on spatial parameters, such as neighborhood memberships based on association with structures such as vessels and or other cell types. In the CD45-positive immune cell example, we could classify two cell populations based on nuclear staining and association with vessels. We hypothesize that these immune cell subpopulations may reflect different

stages of activity and infiltration: from margination, extravasation and exiting vessels towards forming foci of inflammation within the peritubular space. These findings are only proof-of-principle of the capabilities of VTEA in using imaging-based data for discovery of spatially based cell niches and require further validation to fully determine biological relevance and generalizability (Lake 2021, Black 2021).

Next, we demonstrated VTEA's utility in segmentation and analysis of imaging data from kidney tissue, while supporting classification, quantitation, and visualization. VTEA can process mesoscale datasets with tens to hundreds of thousands of cells both in 2D and 3D while maintaining the interactive characteristics of the analysis. In the multiplexed 3D confocal large-scale data, we used unsupervised analysis and dimensionality reduction to classify the cell types and validated these classes of cells based on visualizing the distribution of intensity for each classified cell type. This provides a semiautomated process for large and high-content datasets that augments the rigor of other quality check measures already used, such the validation of the identified cells by mapping them in the original image.

We also analyzed highly multiplexed large-scale data from human cortical kidney tissue imaged with CODEX. This imaging technology expands the ability to multiplex markers on the same 10 micron thick tissue sections using DNA-conjugated antibodies. With CODEX imaging, these antibodies are revealed three at a time by the reversible binding of fluorescent oligonucleotide reporters. Following imaging, the fluorescent reporters are stripped from the tissue and replaced with a second set of three probes and imaged again. This process is repeated until all the antibodies in the tissue have been revealed. Images of DAPI-labeled nuclei are collected in each round to enable

registration of images into a single highly multiplexed image. Although CODEX imaging has been described on mouse and human kidney tissue recently (Neumann 2021), the analytical output from such data has been limited. Using the integrated analytical pipeline with VTEA, we can perform not just cytometry, but also use unsupervised machine learning to classify major cell types and uncover novel subtypes. For example, we demonstrate the existence of subtypes of proximal tubules (PT: CD90-positive PT, PROM1-positive PT) and thick ascending limb cells (PROM1-positive TAL).

Subclassifying also identified T-cell subtypes based on multiple markers. Using neighborhood analysis, we can uncover new spatial associations that could inform on the biology. For example, macrophage association with PROM1-positive TAL cells is consistent with recent single cell transcriptomics data suggesting the transcriptional phenotype of PROM1-positive TALs, may be in niches of immune activation (Lake 2021). We expect that applying VTEA analysis on such highly multiplexed CODEX data will complement and spatially anchor single cell transcriptomics data and may inform and confirm (at the protein level within the tissue) transcriptomics outputs such as receptor-ligand analyses.

The advantages of VTEA analysis have been outlined in this work and include the unique integrated workflow in the setting of a general framework of accessibility, flexibility, and extensibility. VTEA can work as a stand-alone tool carrying the imaging data (after collection) all the way to analysis, which offers unique advantages. For example, applying the integrated VTEA workflow to analyze human kidney multiplexed imaging data will enhance efficiency and discovery because all the steps, including advanced machine learning analysis and visualization, occur in one software space.

Furthermore, VTEA has unique strengths such as: 1) fine-tuning, in real-time, image processing and segmentation parameters to optimize the analysis and 2) gating for interactive back-and-forth between image and analysis. Importantly, VTEA can also operate with custom workflows to accept inputs from other sources. For example, a better segmentation algorithm (by importing segmentation maps) or an outside set of measurements (such as from MorphoLibJ) can be easily imported. VTEA also exports csv files of measured and unsupervised machine learning features and indexed segmentation maps for integration into other tools and pipelines.

Tissue cytometry with VTEA still has limitations. Despite the advantages of an integrated workflow that has been applied on computer desktops (not requiring computer clusters or server-based), the analysis and visualization of large mesoscale datasets will require desktop computers with enhanced data processing and RAM. Although the analyses of the smaller image datasets presented here can be performed on very modest computers (e.g., 2016 Macbook). There are also persistent challenges in mobilizing large datasets from acquisition platforms to the analysis computers. Importantly, this is not unique to VTEA or even TC and a problem that pertains to other mesoscale and omics datasets. Combining datasets, into the same analytical and non-overlapping image spaces within VTEA is an ongoing area of research and development. Practically, with progress in multiscale and hierarchical image formats this may be greatly simplified soon (Moore 2021). Furthermore, multiple datasets can be aligned into a single analysis with VTEA using normalization and mapping strategies but testing and adequately addressing batch effects needs to be established across image datasets (Hickey 2021). One possibility is to use cell-centric neighborhood analysis, which is, by default, normalized spatially for a

common set of cell classifications, to combine disparate imaging datasets. We recently used such an approach on 3D large-scale multiplex confocal image volumes of human biopsies from the Kidney Precision Medicine Consortium and successfully combined neighborhoods of ~1.2 million cells (Lake 2021).

In conclusion, we present tissue cytometry with VTEA as a solution to analyze and interpret high- content imaging data of human kidney tissue. Using appropriate unsupervised machine learning approaches, we demonstrated how VTEA can classify and characterize cell populations based on a suite of cell-wise features including intensity measurements and neighborhood cell population statistics. We anticipate that this approach will be useful in uncovering the complex spatial organization and cellular make-up of the human kidney and generalized to analyzing imaging data of tissues from other organs.

## **Methods**

### *Tissue acquisition*

Tissue was collected and processed under the Institutional Review Board at Indiana University approved protocols: 1906572234, for nephrectomy samples and 1010002261, for human biopsy samples.

### *CODEX*

***Antibody Conjugation and Validation.*** 14 of the 23 antibodies used here were conjugated in-house using the protocol outlined by Akoya Biosciences. To conjugate barcodes to antibodies, antibodies were reduced using a “Reduction Master Mix” (Akoya Biosciences) to which lyophilized barcodes resuspended in molecular biology grade water and “Conjugation Solution” (Akoya Biosciences) were added and incubated for 2

hours at room temperature. Labeled antibodies were purified from free-barcode in a 3-step wash and spin process and stored at 4°C. Successful conjugation was validated via SDS-PAGE gel electrophoresis as well as immunofluorescent staining of reference tissue followed by confocal microscopy.

***Tissue Preparation.*** 10-micron sections of human renal tissue embedded in OCT were cut onto poly-L-lysine coated coverslips. Sections were prepared as detailed by Akoya Biosciences and as described previously<sup>7,14</sup>. Tissue retrieval was conducted with a 3-step hydration process, followed by fixation with a PFA-containing solution. Following fixation, the coverslip mounted tissue was incubated overnight at 4°C with an antibody cocktail of 23 of the antibodies listed in Table 2.3. Tissues were washed, and post-fixed in 4% PFA for 15 minutes.

***Imaging.*** Antibodies were imaged cyclically using the CODEX system from Akoya Biosciences and a Keyence BZ-X810 slide scanning microscope fitted with a 20x air objective (0.75 NA). Images were processed using the CODEX Processor (Akoya Biosciences) and images exported for analysis with VTEA.

#### *Software design, development, and distribution*

Volumetric Tissue Exploration and Analysis (v1.0) was developed in Java, with SQL, R-script and Python, using the integrated development environment Netbeans (Apache) using a maven build scheme. Major application program interfaces (APIs) used in VTEA include SciJava (v.30.0.0), ImageJ (v.1.53f), h2 (v. 1.4.198), SMILE (v.1.5.3), Renjin (v3.5-beta76) and JFreeChart (v. 1.5.0). The github release tag @cdfbd46 can be used to perform all the analyses presented here. VTEA v1.0, bleeding- edge and archival versions, can be downloaded and built from source-code using a maven build scheme,



<https://github.com/icbm-iupui/volumetric-tissue-exploration-analysis> . Stable releases can be installed in FIJI by using the FIJI updater and selecting the “Volumetric Tissue Exploration and Analysis” update site. General description, analysis vignettes with demonstration data and development plans can be found at <https://www.vtea.wiki> and <https://imagej.net/plugins/vtea>.

#### *Computers used in analysis*

Image data was analyzed VTEA on a Macbook laptop (mCorei5, 8 GB RAM, 2016), a Lenovo P51 (Xeon quad-core, 64 GB RAM) or an 8-core custom-built workstation (Xeon 8-core, 256 GB RAM).

#### *Figure preparation*

All images were generated in ImageJ/FIJI and plots (scatter, violin, heatmaps), gated cell overlays and segmentation maps were created by VTEA. Photoshop (Adobe) was used for final annotation and assembly of panels. Scales were set by the microscopy platform and annotated in ImageJ/FIJI. All intensity changes are linear unless otherwise noted.

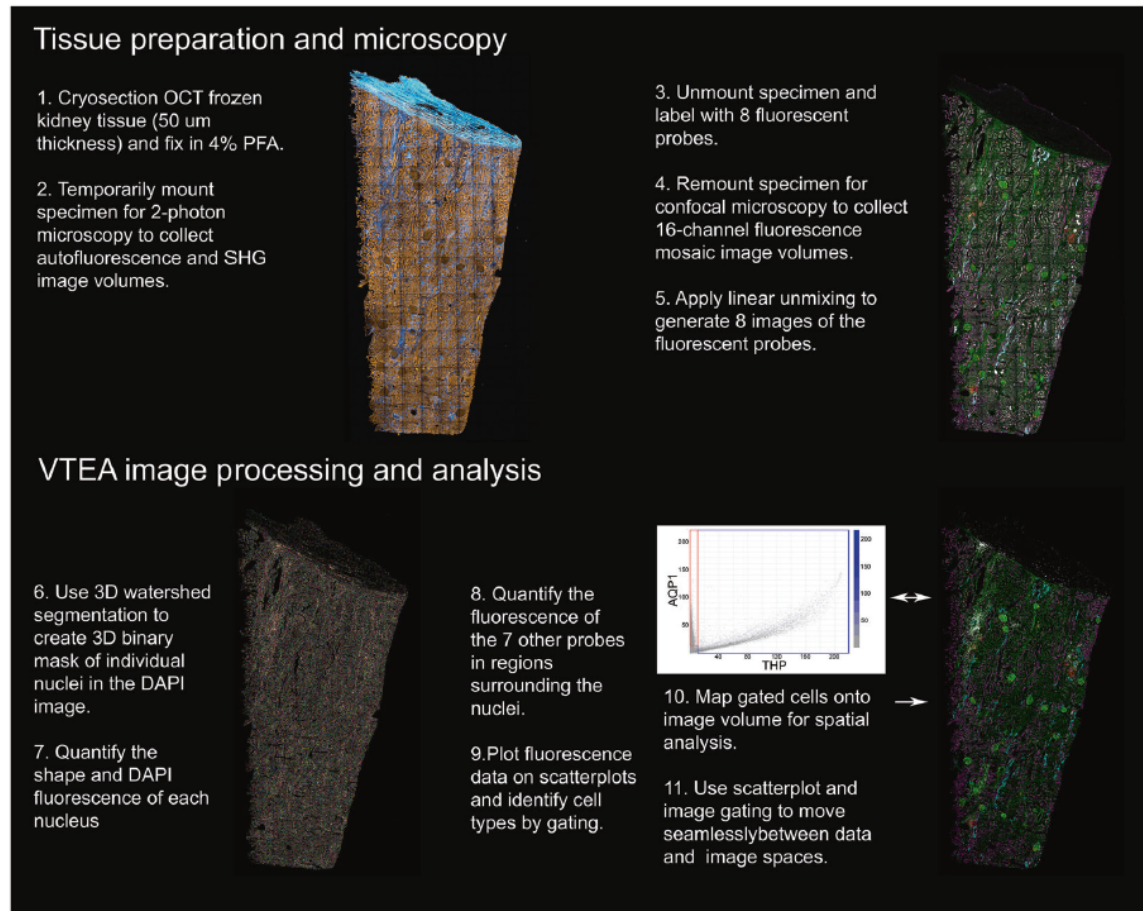


Figure 2.1: Overview of the tissue cytometry workflow. Major steps involved in the tissue imaging analysis pipeline

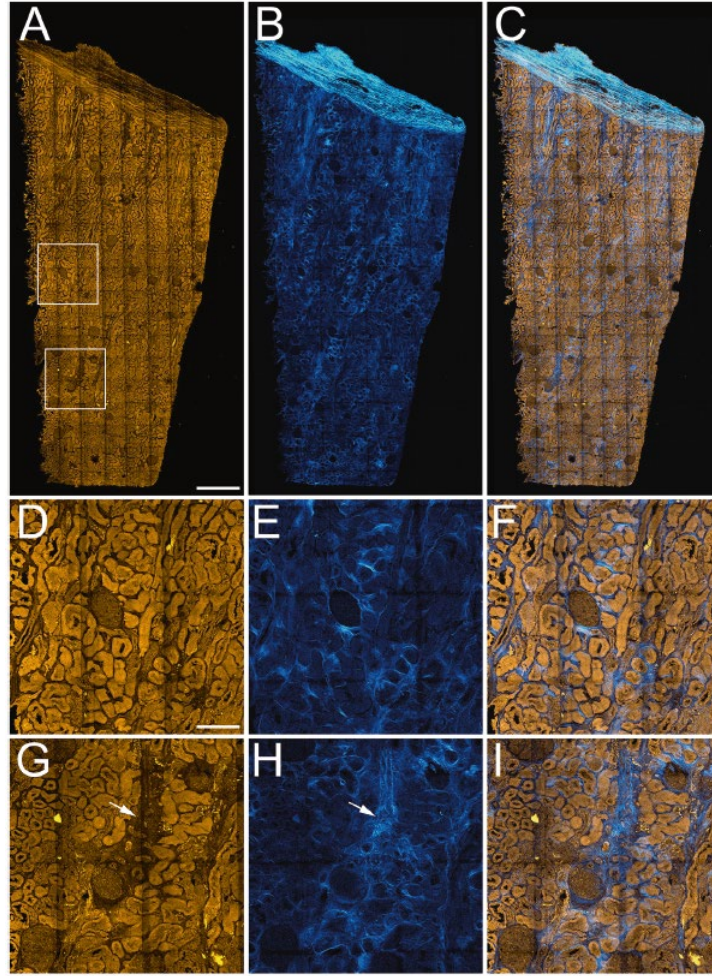


Figure 2.2: 3D multiphoton microscopy of unlabeled nephrectomy. Mosaic of high resolution image volumes collected from a 4 mm by 9 mm, 50 micron thick section of paraformaldehyde-fixed human nephrectomy tissue. A) Maximum projection image of 3D volume of tissue autofluorescence. B) Maximum projection of 3D volume of second-harmonic generation (SHG) images. C Overlay of autofluorescence and SHG. D–F Show corresponding  $\times 4$  magnification images of the region indicated in the upper box in (A), and (G–I) show corresponding  $\times 4$  magnification images of the region indicated in the lower box in (A). Arrows in (G, H) indicate regions of apparent tubular drop out and fibrosis. Scale bar in (A) represents 1 mm. Scale bar in (D) represents 250 microns in (D–I).

Sample	% Cortex	Tissue Volume mm <sup>3</sup>	SHG+ area % total	Total cell	Cell density cells/mm <sup>3</sup>	THP+ cells/mm <sup>3</sup> (%)	AQP1+ cells/mm <sup>3</sup> (%)	MPO+ cells/mm <sup>3</sup> (%)	CD68+ cells/mm <sup>3</sup> (%)	CD3+ cells/mm <sup>3</sup> (%)	Siglec8+ cells/mm <sup>3</sup> (%)
1	90.5	1.73	11.7	248,050	143,506	4495 (3.1)	21,807 (15.2)	2,152 (1.5)	551 (0.3)	5481 (3.8)	15 (0.0001)
2	89.9	0.62	10.9	154,471	249,772	14,166 (5.7)	21,81 (8.5)	864 (0.3)	11 (0.0)	298 (0.1)	0 (0)
3	60.4	1.03	12.3	214,769	207,947	38,840 (18.7)	40,221 (19.4)	5852 (2.8)	435 (0.2)	4131 (2.0)	0 (0)
4	100	0.45	10.4	112,360	250,786	23,826 (9.5)	31,533 (12.6)	11,595 (4.6)	1129 (0.5)	16,452 (16.6)	0 (0)
5	44.7	0.72	7.7	234,685	326,625	99,141 (30.4)	63,357 (19.4)	3592 (1.1)	1063 (0.3)	8,706 (2.7)	0 (0)

Table 2.1 - Results of label free and VTEA analysis of five nephrectomy samples

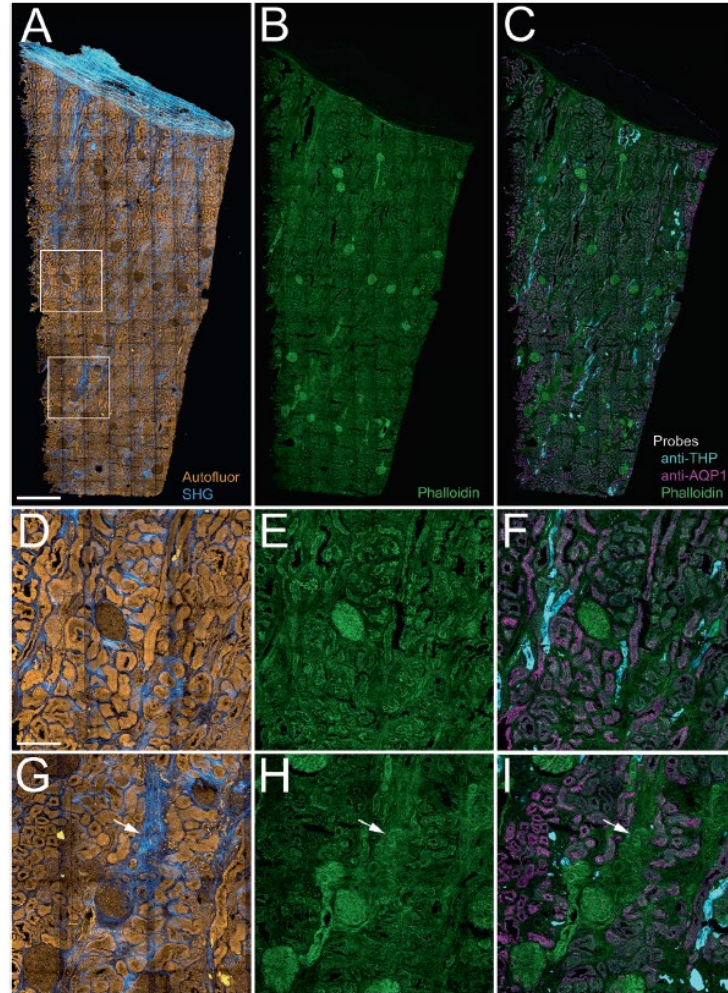


Figure 2.3: 3D confocal immunofluorescence of structural markers. A) Maximum projection of combined autofluorescence and SHG images. B) Maximum projection of mosaic of confocal fluorescence image volumes of Oregon-Green phalloidin. C) Overlay of maximum projection confocal fluorescence images of phalloidin (green) and antibodies to Tamm–Horsfall Protein (THP, cyan) and aquaporin-1 (AQP1, magenta). D–F Show corresponding  $\times 4$  magnification images of the region indicated in the upper box in (A), and (G–I) show corresponding  $\times 4$  magnification images of the region indicated in the lower box in (A). Arrows in (G–I) indicate regions of fibrosis and apparent tubular drop out. Scale bar in (A) represents 1 mm. Scale bar in (D) represents 250 microns.



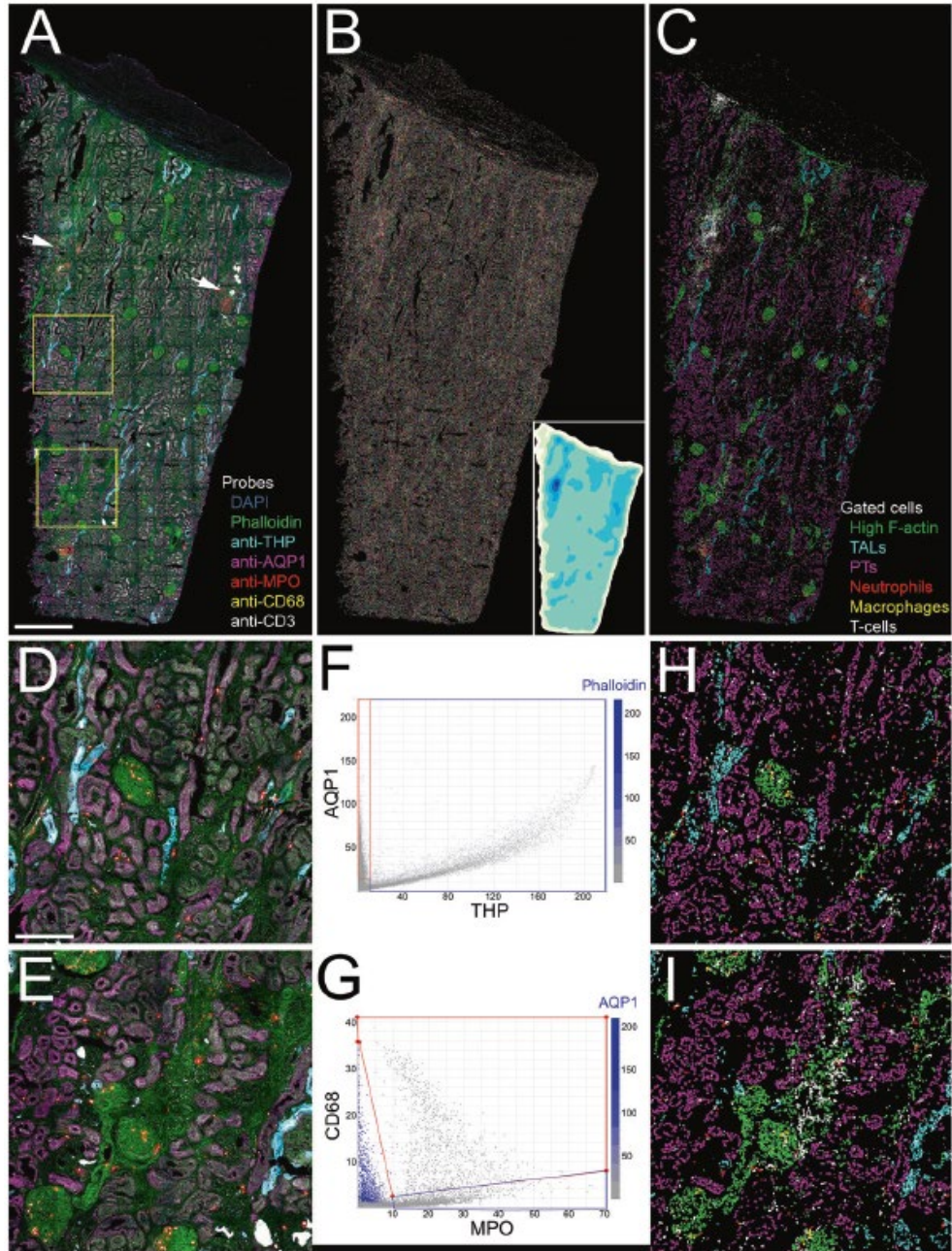


Figure 2.4: 3D confocal fluorescence microscopy and cytometry of structural and immune cell markers. A Maximum projection of combined fluorescence images of DAPI (gray), phalloidin (green) and antibodies to THP (cyan), AQP1 (magenta), myeloperoxidase (MPO, red), CD68 (yellow) and CD3 (white). Arrows indicate two regions of immune cell infiltrates. (continued on next page)

(Figure 2.4 cont.): B) Projection of 3D image volume of binary map of nuclei following image segmentation using VTEA. Each segmented nucleus is presented in an arbitrary color. Inset is an isomap of cell density with darker colors depicting higher cell densities. C) Distribution of different cell types following scatterplot gating. Green—phalloidin, Cyan—thick ascending limb, and Magenta—proximal tubules. Red—neutrophils, Yellow—macrophages, White—T cells. D, E Show corresponding  $\times 4$  magnification images of the regions indicated in the two boxes shown in (A). F, G Show scatterplots of the fluorescence intensity of THP vs. AQP1 and MPO vs. CD68, respectively. In each scatterplot, the color of each point represents the fluorescence intensity of a third probe (phalloidin and AQP1, respectively were chosen for these examples). H, I Show the locations of the different cell types in the regions shown in (F, G), respectively, as determined by scatterplot gating. Scale bar in (A) represents 1 mm and 250 microns in (D).

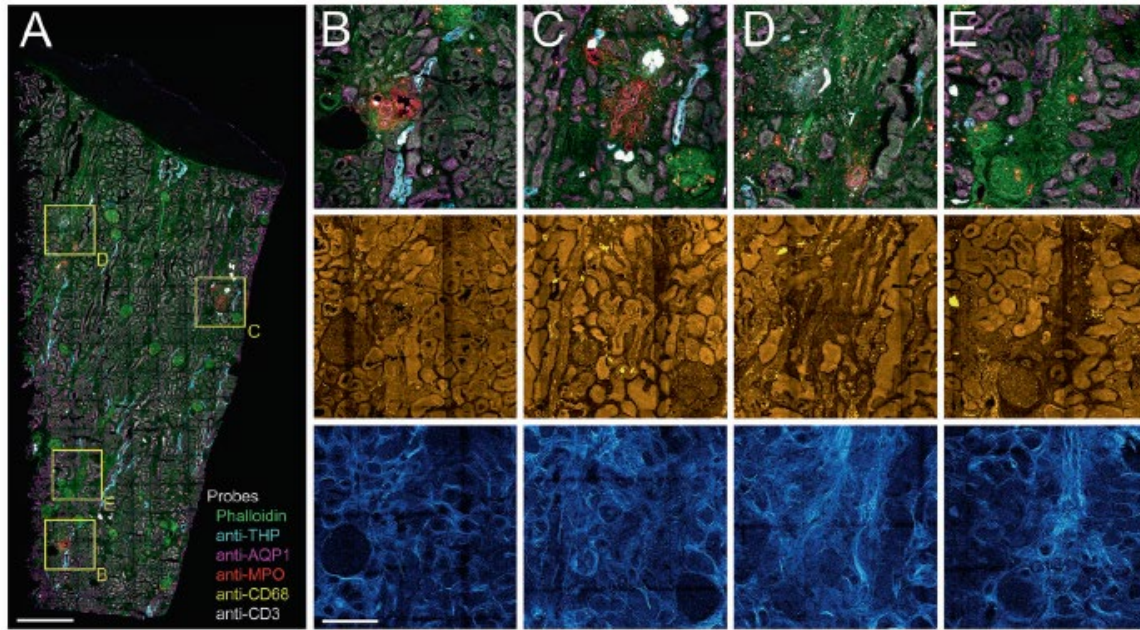


Figure 2.5: 3D confocal fluorescence and multiphoton autofluorescence/SHG microscopy of regions of apparent injury. A) Maximum projection of combined 3D fluorescence image volume of phalloidin (green) and antibodies to THP (cyan), AQP1 (magenta), myeloperoxidase (MPO, red), CD68 (yellow), and CD3 (white). B–E  $\times 4$  magnifications of regions indicated in boxes in (A). Top row— confocal fluorescence images. Middle row—corresponding autofluorescence images. Bottom row— corresponding SHG images. Scale bar in (A) represents 1 mm and in (B) 250 microns for (B–E).



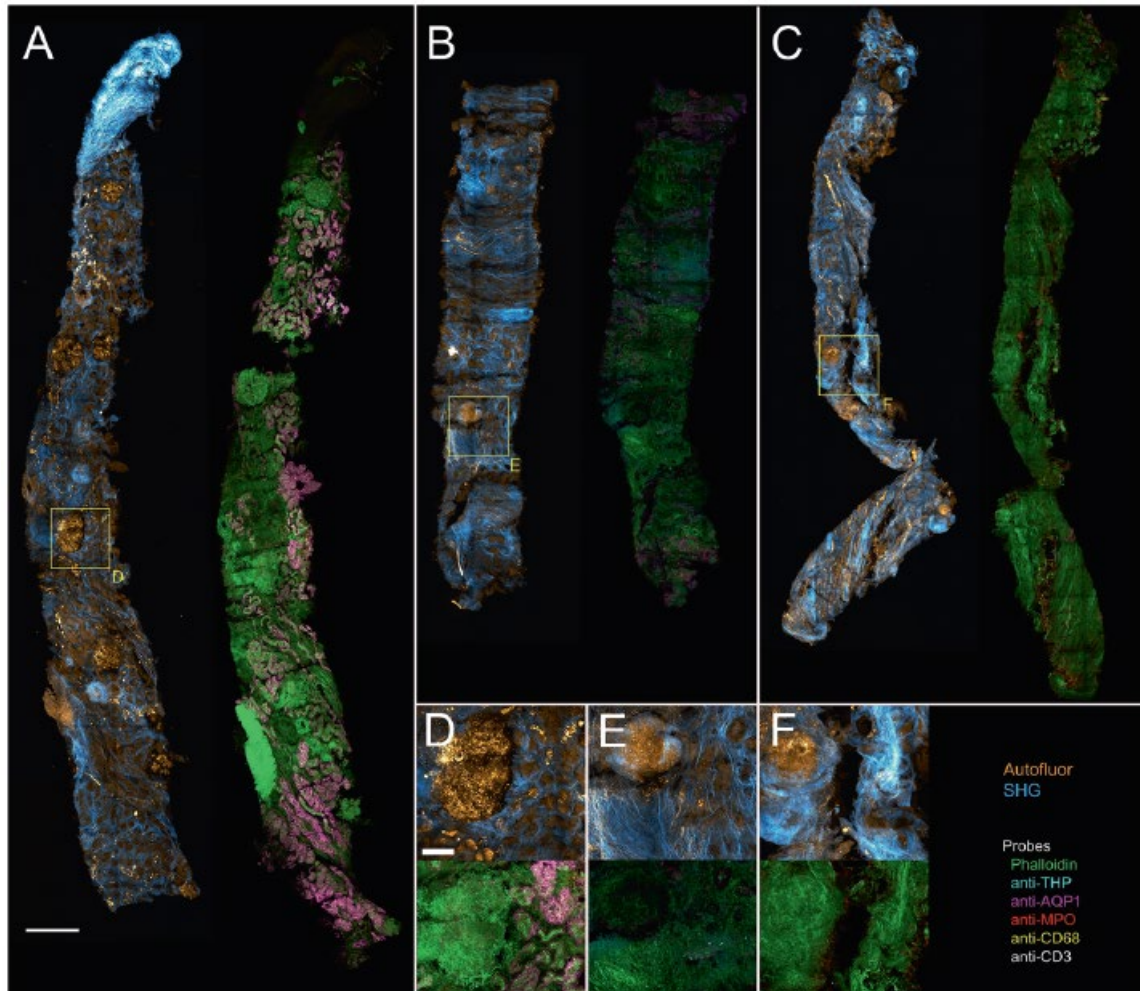


Figure 2.6: 3D Multiphoton autofluorescence/SHG and confocal immunofluorescence microscopy of diabetic renal biopsies. Gallery of 50 microns sections of diabetic biopsies. A–C) Maximum projections of combined 3D label-free autofluorescence and SHG images (Autofluor/SHG) (left) and immunofluorescence confocal images (right). Phalloidin (green), THP (cyan), AQP1 (magenta), myeloperoxidase (MPO, red), CD68 (yellow), and CD3 (white). D–F) Insets from biopsies representing highlighted regions in (A) through (C), respectively. The top row shows maximum projections of combined autofluorescence and SHG images and the bottom row shows corresponding immunofluorescence images. Scale bar in (A) represents 2 mm and in (D) represents 100 microns (D–F).

Sample	% Cortex	Tissue Volume mm <sup>3</sup>	SHG+ area % total	Total cell	Cell density cells/mm <sup>3</sup>	THP+ cells/mm <sup>3</sup> (%)	AQP1+ cells/mm <sup>3</sup> (%)	MPO+ cells/mm <sup>3</sup> (%)	CD68+ cells/mm <sup>3</sup> (%)	CD3+ cells/mm <sup>3</sup> (%)	Siglec8+ cells/mm <sup>3</sup> (%)
DN 1	90.8	0.1281183	9.4	59,852	467,163	343 (0.07)	52,131 (11.2)	991 (0.2)	4355 (0.9)	0 (0)	47 (0.001)
DN 2	100	0.01018575	12.6	48,827	479,365	2926 (0.6)	88 (0.02)	2258 (0.05)	216 (0.05)	0 (0)	30 (0.006)
DN 3	100	0.0729754	27.3	41,536	569,178	260 (0.05)	96 (0.02)	2480 (0.3)	12443 (2.2)	0 (0)	41 (0.007)

Table 2.2 - Results of label free and VTEA analysis of three diabetic biopsies

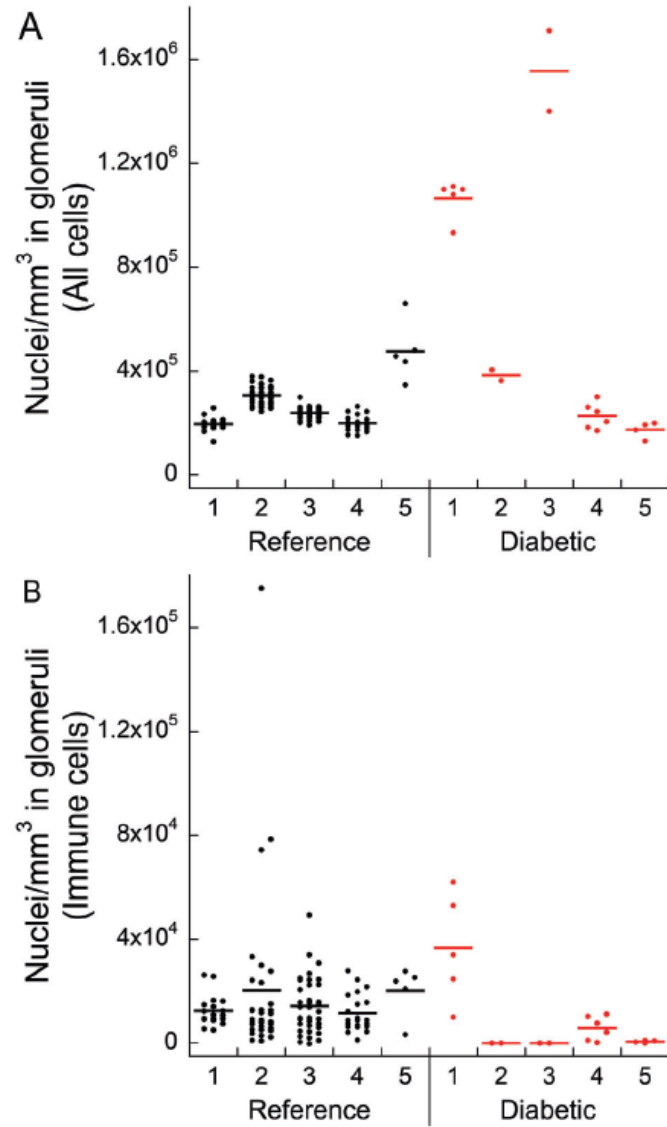


Figure 2.7: Scatterplots of glomerular nuclear density and immune cell density. A) Total cell densities for five reference (black dots) and five diabetic (red dots) cases. B) Density of all probed immune cells (myeloperoxidase (MPO), CD68, CD3, and SIGLEC8 positive cells) from the same samples. Each dot represents a single glomerulus.

<b>Antibody</b>	<b>Significance</b>
CD45	Leukocytes
CD90	Differentiation
CD3	Pan T Cells
CD4	CD4+ T Cells
CD11c	Res. Dendritic
CD45R0	Mem T Cells
MPO	Neutrophils
CD68	Macrophages
HLA-DR	APCs
AQP1	PT, TDL
E-cadherin	DCT, CD, Loop
B-catenin	Tubular epithelium
LRP2	PT
Podocalyxin	Podocytes
Uromodulin	TAL
$\alpha$ -SMA	Arterioles
CD31 (PECAM1)	Endothelium
Cytokeratin 8	CNT and CD
IGFBP7	Injury
pcJUN	Stress kinase
PROM1 (CD133)	Fibrosis

Table 2.3 - Antibodies used for CODEX multiplexed imaging

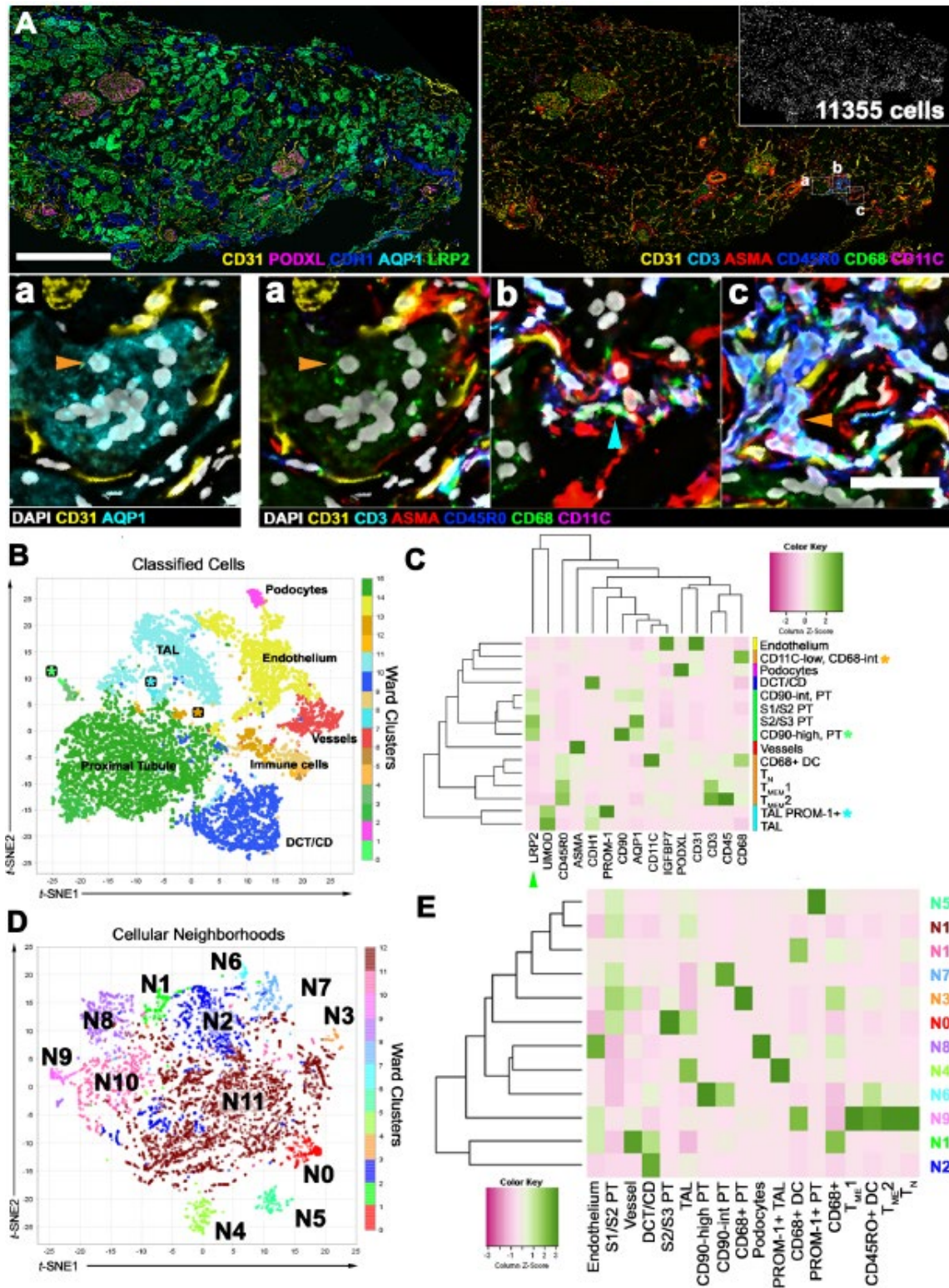


Figure 2.8: Automated detection, classification of cell-types and assessing cellular microenvironments in CODEX data with VTEA. Multiplexed immunofluorescence image dataset of human reference kidney was processed, segmented, and analyzed with VTEA. A) Maximum projects of subsets of channels highlighting tubular epithelium or immune cells in the renal cortex. Left panel indicates three regions given in Aa, Ab and Ac and segmentation mask (inset). Scale bars are 500  $\mu$ m and 30 microns. B) Segmented cells with associated marker intensity with clustered using hierarchical clustering and projected into *t*-SNE space using the average intensity of associated markers. Putative cell-types as indicated. C) Marker intensity for clusters identified in B, normalized by marker. Cell types include subclasses of epithelial and leukocytes. TMEM and TN are putative memory and novel T-cells. epithelium identified included proximal tubule (PT) S1, S2 and S3 subsegments, loop of Henle thick ascending limb (TAL) and the distal nephron subsegments distal convoluted tubule (DCT) and collecting duct (CD). Markers are given at bottom. A subset of clusters had overlapping proximal tubule (LRP2-positive green arrowhead) and TAL (cyan asterisk) or leukocyte signatures (green and orange asterisks). D) Using cell-types defined in C) and Figure 2.9, neighborhoods were defined in VTEA for every cell within 50 microns. The cell census for all neighborhoods was used to cluster and map the neighborhoods to *t*-SNE space in VTEA. E) The distribution of cell-types was plotted by neighborhood as a heatmap to identify unique microenvironments in the tissue volume.



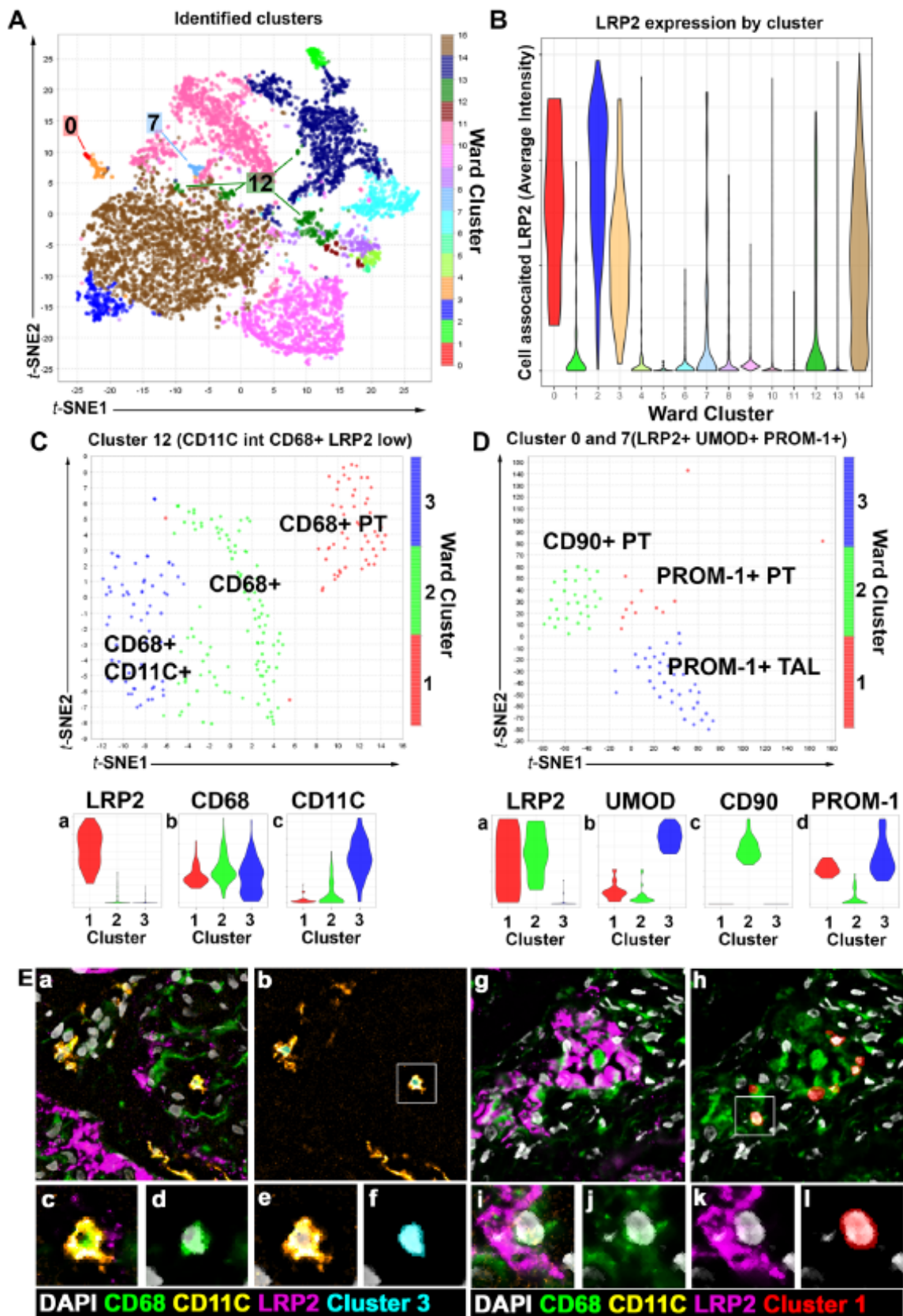


Figure 2.9: Subclustering of epithelial cells in CODEX data uncovers novel cell states in the proximal tubular (PT) and thick ascending limb (TAL). A-B) Clusters 12 or clusters 0 and 7 from Figure 2.8 were subgated based on intermediate LRP2 expression and either CD68 or PROM-1 or UMOD expression. C) Cluster 12 was reclustered separating CD68+ DCs, putative macrophages and CD68-positive PT cells. D) Clusters 0 and 7 were subgated and reclustered identifying two PT cell-types (PROM-1-positive vs. CD90+). E) CD68-positive DC-cells and putative epithelium are readily identifiable (Ea-f vs Eg-m). Ec-f and Ei-l are insets for Ea and Eh respectively.



## Chapter 3- CODEX Multiplex Imaging of the Murine Kidney

### **Introduction**

CODEX multiplex imaging is a unique technology in that it expands the usability of a single tissue section beyond the limitations of standard imaging practices. With standard protein-based imaging, the number of probes that can be imaged at one time is limited to around four to eight probes, depending on the expertise of the user. In order to image multiple cell types in the kidney with standard imaging practices, numerous tissue sections would be necessary, which is not always possible with renal biopsy specimens, as discussed in the first chapter of this work. CODEX multiplex imaging removes the need for multiple tissue sections via its cyclic staining and imaging procedure.

Imaging with the CODEX system starts with a two-day staining process, where the tissue is subjected to a multi-step fixation followed by the addition of the primary antibodies. These antibodies have a unique oligonucleotide tag that is complimentary to only one specific barcode attached to a reporter that gets added later, during the imaging process. Once tissue imaging begins, the reporters are added to the tissue in sets of three, incubated, imaged, and then stripped from the tissue so the next set of three can be added.

Another benefit to the CODEX imaging process is that all probes of interest are being imaged on the same tissue slice at the same time. This allows for the most accurate cell association studies to be conducted, as it eliminates the need to superimpose consecutive sections on one another. While serial sectioning is a common practice for obtaining spatial relationship information on multiple cell types, there is the potential for artifacts to be introduced by incomplete alignment of the consecutive sections. There is also the possibility that sections could be skipped during sectioning, thereby increasing the chances of indirect correlations being made.

In our early studies where CODEX multiplexed imaging was used to validate findings from spatial transcriptomics, we showed that the distribution of infiltrating macrophages and neutrophils shifted towards the medulla with injury (Ferreira 2021). In order to further characterize these finding, we expanded both the antibody panel and the number of samples being analyzed. Mice from four different groups were selected, including wildtypes from sham and 22-minute clamp/6-hour recovery IRI surgery, as well as THP knockout mice from sham and surgery groups. THP has a diverse repertoire of functions in the kidney, including but not limited to water impermeability and ion-channel activity of the TAL cells, homeostasis of calcium, magnesium and mononuclear phagocytes, and – most importantly for this study - susceptibility and response to kidney injury (Micanovic 2020).

THP is a protein uniquely made in the TAL cells of the kidney. During AKI, the production of THP is reduced at both the RNA and protein levels, therefore inducing a state of THP deficiency (Micanovic 2020). Due to this, THP knockout mice experience more severe injury than wildtype mice when they undergo IRI surgery. Because of THP's role in signaling and other homeostatic regulatory processes (neutrophil and macrophage regulation, suppression of inflammation), the total loss of THP that is seen in the knockout state leads not only to a more severe injury, but also a longer lasting inflammatory state. Therefore, when looking at both wildtype and THP knockout mice that have undergone IRI surgery, one could hypothesize that there would be differences, not only in the amount of inflammation present, but also in the number and distribution of immune cells that are present.

In this study we investigated eleven different samples, two wildtype sham, three wildtype IRI, three THP knockout sham, and three THP knockout IRI tissues. Each tissue was stained with 33 different antibodies, which are listed in Table 3.1, and imaged using CODEX multiplexed imaging. After imaging, unsupervised analysis of the segmented cells was utilized to facilitate their classification within the specimens. A unique aspect of this study is that all eleven datasets were combined into a single analytical space and investigated for changes in immune cell counts and distributions throughout the kidney. This was done using a scaling and normalization algorithm within the R software using cell objects derived from the VTEA analytical pipeline. With this approach, major cell classes were identified, including all tubule sections, broad immune cell classes, and different types of vasculature. In addition to the identification of major cell classes, such analysis allowed us to define the changes in immune populations between injury and sham, as well as between knockout and wildtype samples.

## **Results**

### *Identifying major cell types and classes present in the mouse kidney*

The first goal of this experiment was to create an atlas of the murine kidney, identifying all of the major cell types present, including tubule segments, vasculature, resident immune cells, and other interstitial cells. In order to achieve this, all eleven samples were analyzed in one space to allow for direct comparisons between injury and sham, as well as THP knockout versus wildtype. This approach also allowed us to detect and correct for any batch effect between groups. Twenty-three cell clusters were identified, including five unique immune cell classes and three classes of non-defined cell types (Figure 3.1). All cell classes indicated were first identified using violin plots to

determine which clusters contained cells positive for specific markers (Figure 3.1). After putative cell classes were determined, we then validated these identities through a process of back-mapping, where clusters were overlaid onto the original image and the staining could be displayed next to the positive cells found. An example of this validation is shown in Figure 3.1 for three different cell classes.

Cell types from each segment of the nephron were identified. For example, in proximal tubules we were able to distinguish S1, S2, and S3 segments. Podocytes were identified by their unique nephrin staining, and LRP2 (megalin) was used to identify the proximal tubules. Other markers that were used include the following: THP (uromodulin) for the thick ascending limbs (in wildtype mice), AQP2 for the collecting ducts, and Na<sup>+</sup>/K<sup>+</sup>-ATPase for the distal nephron segments. The different components of the vascular system of the kidney were identified based on staining with endomucin, CD31 (PECAM1), and von Willebrand factor for the endothelium, and  $\alpha$ -SMA for arterioles.

For the immune cells, multiple antibodies were selected which ranged from pan markers to specific immune cell subtypes. CD45, MHCII, CD74, and CD3 were chosen to distinguish major immune cell types. Specifically, CD45 is present in almost all immune cells, MHCII is a marker for all antigen presenting cells, CD74 marks macrophage and myeloid cells, and CD3 is a pan T cell marker. We also included specific markers for immune subtypes such as T helper cells (CD4), cytotoxic T cells (CD8a), natural killer cells (Nkp46), neutrophils (CD11b and Ly6G), and dendritic cells and M1/M2 macrophage differentiators (CD11c, CD206, CD169, and Chil3).

### *Subsetting the immune populations*

The parent clustering using Louvain methods (a graph based unsupervised clustering using community-based detection) provided five immune cell clusters. These were not very distinct clusters, leading us to believe many immune cell subtypes were consolidated into one cluster. Because of this, we decided to pull the five main immune cell clusters from the parent Louvain and re-clustered them with a new feature space that was specific to immune cells. Doing this resulted in 12 unique classes, as shown in Figure 3.2. Figure 3.2 also shows the immune cell Louvain clustering broken down by condition, in order to see any shifts in abundance from one condition to another between the clusters. The T cell and neutrophil clusters both showed an increase in injury, as well as in the absence of THP. There were nine different monocyte populations uncovered as well, including two classes of dendritic cells and seven macrophage classes. The two dendritic cell classes differed in their CD11c intensities, as well as CD74 and MHCII levels (Figure 3.2). For the seven macrophage classes, the distinctions were more subtle. There was one CD169<sup>+</sup> macrophage class identified (Cluster 1, Figure 3.2), but the other six classes only differed in their levels of CD74 and MHCII staining (Figure 3.2).

To help elucidate the types of macrophages, we then mapped each of the clusters back onto the image to see their distributions and how injury effected their location. Mac.2 and Mac.3, for example, were dispersed through the cortex of the WT Sham sections, but shifted towards the medulla of the kidney in IRI (Figure 3.3). While the abundance of Mac.2 and Mac.3 decreased in the THP knockout mice, the same shift towards the medulla was noted, leading us to believe that these are infiltrating macrophages. Mac.1, Mac.4, Mac.5, and Mac.6 showed less obvious distribution changes

when looking at the WT Sham and IRI sections. They did, however, show an increase in abundance in the THP knockout mice (Figure 3.3).

#### *Niche analysis of monocyte populations*

Due to the distribution changes noted in some of the immune cell classes, neighborhood analysis was conducted to quantify the associations and cell to cell interactions between macrophage populations of interest and tubule segments. With this analysis, we focused on the CD169+ macrophages, Mac.2, Mac.3 and Mac.5 clusters. Pearson's correlation showed that Mac.2 and Mac.3 had a positive correlation with S1/S2 PT's, TAL.1 and TAL.2 in the WT Sham tissues (Figure 3.4). In the WT IRI samples, the positive S1/S2 PT correlation became negative, the TAL.1 positive correlation decreased, and the TAL.2 association markedly increased (Figure 3.4). CD169+ macrophages showed an increased positive correlation in WT IRI samples as well, as did Mac.5. Mac.5 however, showed an interesting association with the KIM1+ S3 PT's that persisted in both the WT Sham and IRI groups. This population did however show the same increase in correlation with TAL.2 as the other macrophage clusters in the WT IRI sections.

When looking at the THP knockout tissues, Mac.2, Mac.3 and Mac.5 followed the same changes in correlations as the wildtype tissues. While they started as a scattered population in both the cortex and medulla in the THP knockout sham, they showed an increase in positive correlations with the more medullary-based TAL populations after injury (Figure 3.4). The CD169+ macrophages, however, showed a different pattern. Rather than shifting towards the TAL populations like the WT IRI samples, this population stayed associated with the PT populations, especially the S3 PTs, and also showed a shift towards the glomeruli in the knockout samples (Figure 3.4).

## Discussion

Using CODEX multiplexed imaging, we were able to image 33 different markers on a single tissue specimen, eliminating the need for serial sectioning and overlaying images onto one another to see associations of cell types. With this method, we identified each segment of the nephron, multiple types of vasculature, as well as twelve different immune cell subtypes. Within sections of the nephron, we were also able to subdivide the proximal tubules into four different classes, two of which were positive for KIM1. S1/S2 segments were able to be differentiated from the S3 segments based on LRP2 staining intensity, which is known to be lower in the S3 segments. We were also able to identify the thick ascending limbs of the loop of Henle within the THP knockout mouse, even though THP was not present. To do so, Na<sup>+</sup>/K<sup>+</sup>-ATPase staining intensity was evaluated, as the thick ascending limbs have a lower Na<sup>+</sup>/K<sup>+</sup>-ATPase signal than that of the distal tubule segments. The classes identified as potential TAL clusters were also mapped back onto the tissues in order to confirm the location of these segments, as TALs are in both the cortex and early medullary regions.

For the immune cells, we created an expansive panel to be able to identify not only the major immune cell classes but also the specific subtypes within each group. This analysis provided twelve unique immune cells classes, including neutrophils, T cells, NK cells, dendritic cells, and macrophages. The neutrophils were identified by the presence of Ly6G, T cells by the presence of CD3, NK cells by the presence of NKp46, and macrophages were broadly identified by the presence of MHCII and CD74. In order to identify the B cells and fully separate the T cell subtypes, there is some optimization needed with both the antibody selection and analysis. The dendritic cells and

macrophages, however, were able to be sub-classified with more resolution. There were two dendritic cell populations identified, clusters 3 and 10, that differed in their expression levels of CD11c. The seven macrophage clusters were able to be distinguished by levels of CD11b, CD169, and CD206 as well as the initial CD74 and MHCII levels. Immune cell cluster 1 was called CD169+ macrophage because of its high CD169 intensity, setting it apart from the other macrophage classes. The other macrophage clusters were labelled Mac.1 – Mac.6, as the distinguishing features became less apparent. The Mac.1 population (Cluster 5) had some CD11b staining that the other populations did not have. Due to their response to injury and THP deficiency, the Mac.2 and Mac.3 populations are likely infiltrating macrophages. Clusters 9, 11, and 12 (Mac.4, Mac.5, and Mac.6) were harder to distinguish, as their staining differences were only seen in MHCII and CD74. Mac.5 in particular is a population of interest, as it doesn't respond to injury or THP deficiency as one would have expected. Mac.5 not only increased in the THP knockout mice, but it also stayed associated with the KIM1+ S3 PTs in both the wildtype and THP knockout IRI mice. This suggests that rather than being regulated by THP, this population could be responding to the presence of KIM1.

In this study, we were able to characterize the mouse kidney using a novel methodology. Characterizing the renal space of the mouse as extensively as we did can provide an almost endless amount of information, focusing on the immune cells was only the start of the possible routes that could be taken. Future directions for this project include looking into the other immune cell subtypes that were not explored yet, further classifying the proximal tubule classes and studying areas of injury, as well as analyzing changes in vasculature and its association with injury. The three non-defined classes that



were found could also be further studied to see what cell types might be present in those classes. This study could also be expanded to examine at other recovery time points, as the six-hour recovery is still early. Including later time points could help provide more information on the immune cell response, as more population changes may occur as recovery progresses.

## **Methods**

### *Tissue Sectioning*

10-micron sections were cut onto Poly-L-Lysine coated coverslips and stored at -80C overnight until staining the next day.

### *Tissue Staining*

Upon removal from -80C coverslips were placed on dririte beads for two minutes to thaw. Samples were then placed in acetone for ten minutes to remove the rest of the OCT from around the tissue and the coverslip. After washing in acetone, coverslips were placed in a humidity chamber for two minutes, then rehydrated in a two-step hydration buffer wash. Tissues were then fixed in a mixture of PFA and hydration buffer for ten minutes. After fixing, residual fixative solution was rinsed with hydration buffer, and then coverslips were placed in staining buffer for thirty minutes, during which the antibody cocktail was made for the samples. Tissues were allowed to incubate in the antibody cocktail overnight at 4C. After overnight incubation, tissues were washed of the staining solution in staining buffer, and then placed in a pos-label fixative solution for ten minutes. Tissues were washed again, fixed in methanol for five minutes, washed, and placed into a final fixative solution for twenty minutes. Coverslips were then stored in storage buffer and stored at 4C until imaging.

### *Reporter Plate*

Reporter stock solution was created using nuclease free water, assay reagent, DAPI, and 10x CODEX buffer. Solution was distributed into the appropriate number of wells for the number of cycles, and up to three reporters were added to each well.

Imaging and Image Processing – Imaging of the coverslips was conducted using a Keyence BZ-X810 epifluorescence microscope, a 20x air objective, and filter cubes for DAPI, GFP, TRTIC, and Cy5. Images were stitched and processed using the CODEX Processing software. Processing included background subtraction to correct for autofluorescence, tissue drift compensation (cycle alignment), and deconvolution.

### *Image visualization and analysis*

Visualization of images was conducted using ImageJ/FIJI, and initial analysis used VTEA, a free plugin for ImageJ. In order to combine datasets into one analytical space, the data was imported into R studio, and was normalized and scaled before being analyzed.

<b>Antibody</b>	<b>Significance</b>
CD11b	Macrophage
CD45	Pan Immune Cells
CD11c	Dendritic Cells
B220	B Cells
CD3	T Cells
CD169	Monocytes & Macs
Ly6G	Neutrophils
CD206	M2 Macrophages
Chil3	M2 Macrophages
CD4	T Helper
CD8a	Cytotoxic T Cells
Ly6C	Bone Marrow Macs
NKp46	NK Cells
CD74	MHC Class II
MHC-II	APC's
CD90	Differentiation
pMLKL	Necroptosis
CD71	Transferrin
VCAM1	Non-repairing Cells
pcJUN	Stress Kinase
Ki67	Proliferation
KIM1	Injury
ATF3	Injury
Nephrin	Podocytes
LRP2	PT
THP	TAL
NaK ATPase	Distal Nephron
AQP2	Collecting Ducts
CD31	Vasculature
VWF	Endothelial
a-SMA	Arterioles
Endomucin	Endothelium

Table 3.1 - Antibodies used for CODEX multiplexed imaging of mouse kidney specimens

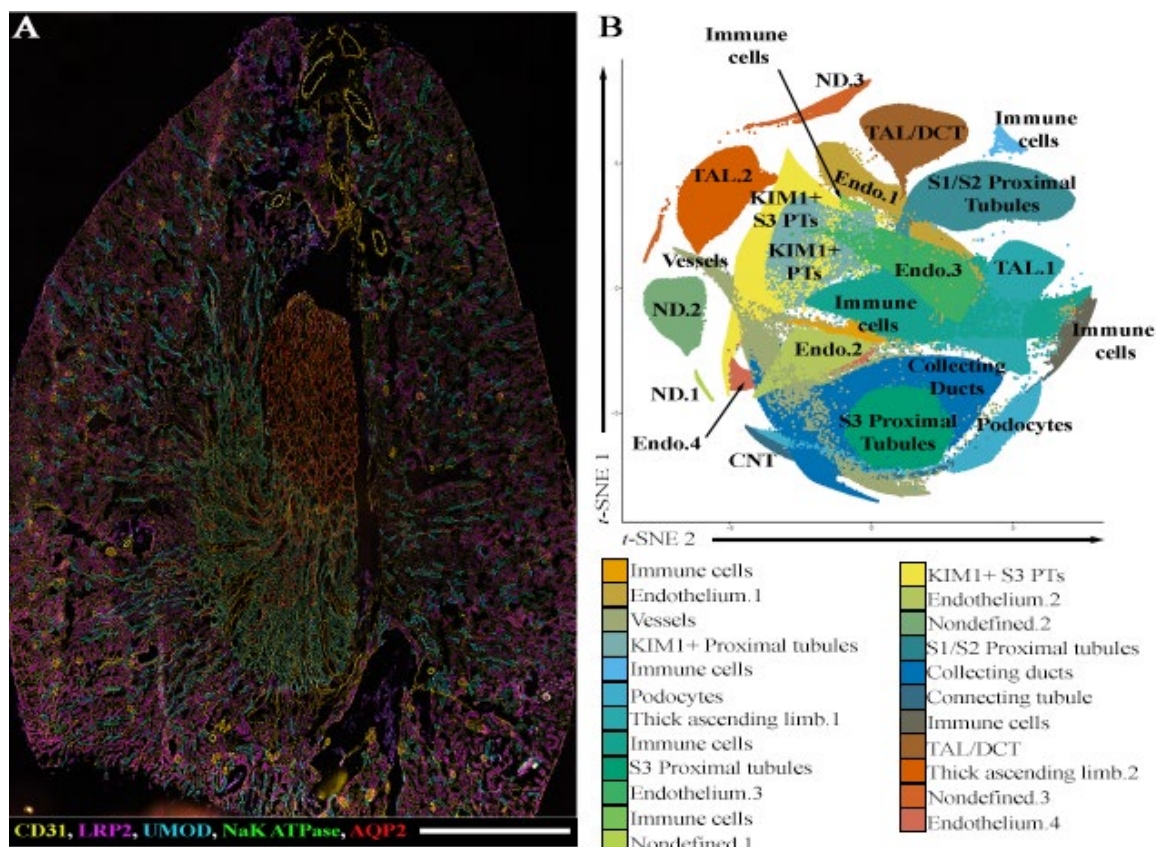


Figure 3.1: CODEX multiplex imaging allows for the identification and classification of all major cell types present within the kidney, including immune cells and injured populations. A) Representative image of a wildtype sham kidney that was analyzed in this dataset. Channels included are CD31 (endothelium), LRP2 (proximal tubules), UMOD (thick ascending limbs), NaK ATPase (distal nephron), and AQP2 (collecting ducts). Scale bar is 1 mm. B) tSNE plot of the Louvain clusters from the eleven datasets analyzed. C) Violin plots showing the average intensity of specific markers across the different Louvain clusters determined in B. D) Back mapping of three different clusters to show the validation steps that are taken to confirm the identities of each cluster proposed in B.

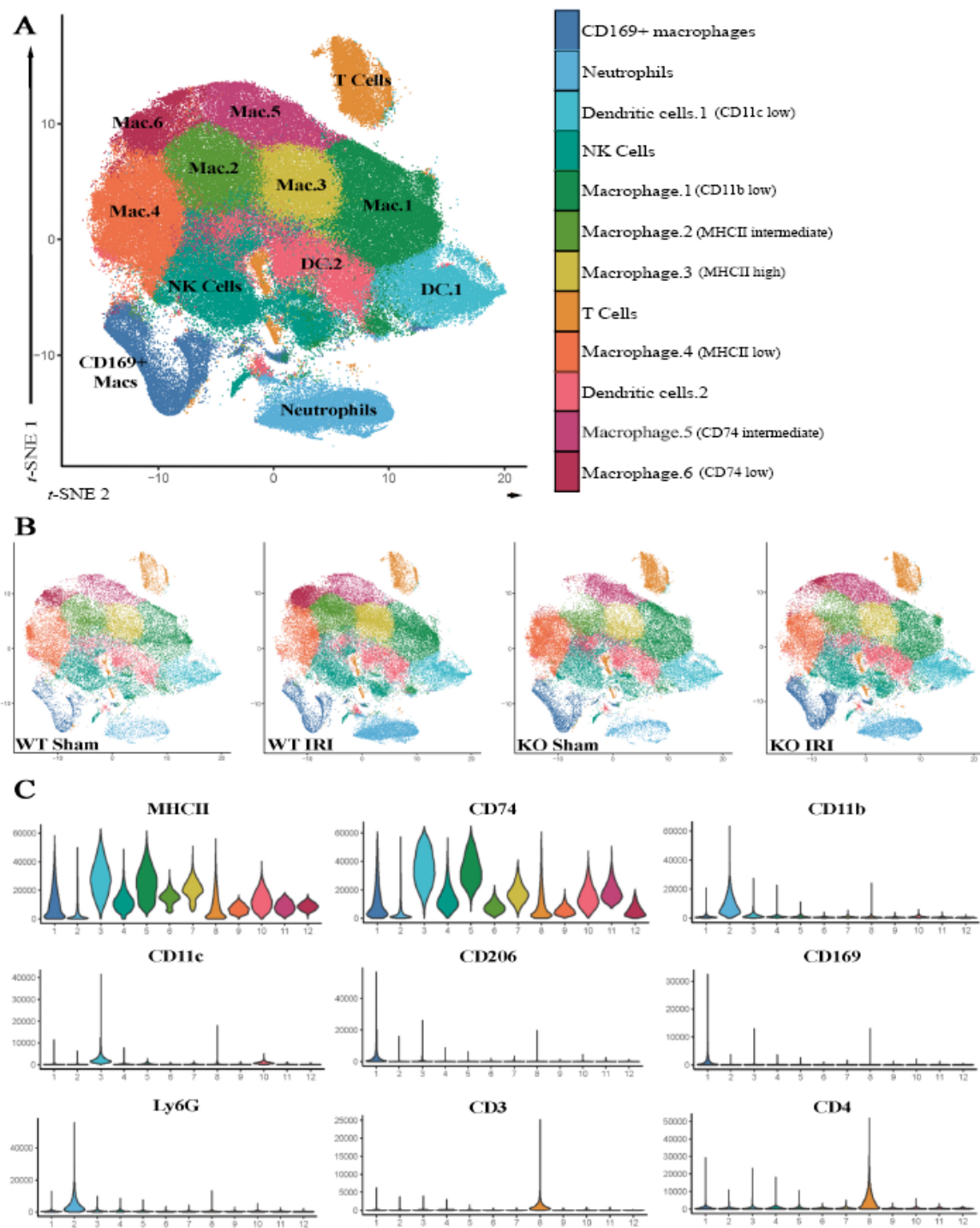


Figure 3.2: Subclustering and identifying immune cell populations. A) tSNE plot of the immune subclustering results from the immune populations pulled from the parent Louvain in Figure 3.1B. B) The immune tSNE plot broken down by condition to show changes in the abundance of each cluster across the conditions. C) Violin plots showing the average fluorescence intensity of major immune cell markers.



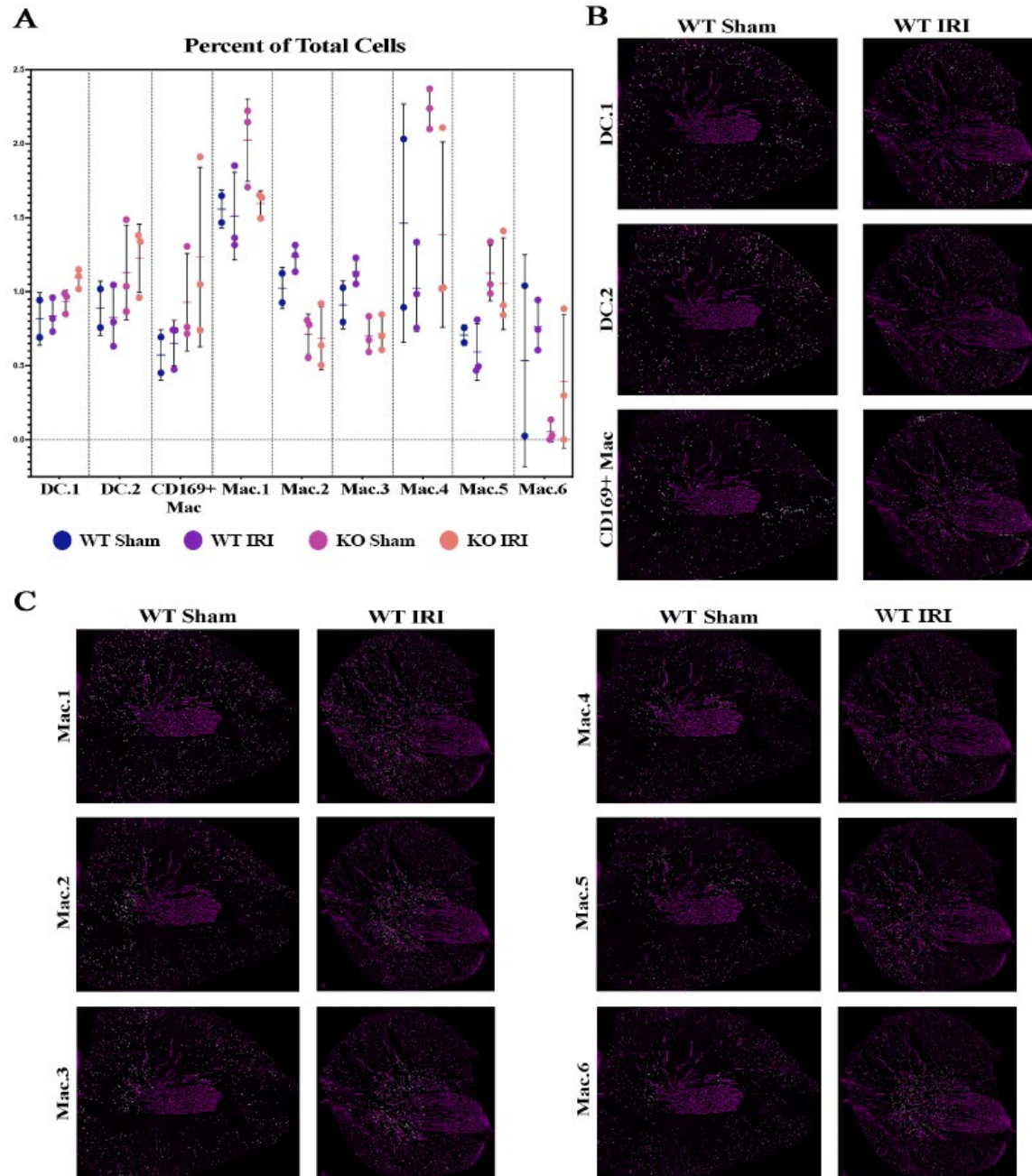


Figure 3.3: Changes in abundance and distribution of myeloid cells in injury and THP -/- mice. A) The percent of the total cell count from each specimen per condition of the eight myeloid cell subclusters found in this analysis. B, C) Back mapping of each of the myeloid cell clusters are shown in white with AQP2 staining in magenta. Representative tissues from the wildtype sham and IRI groups are shown.



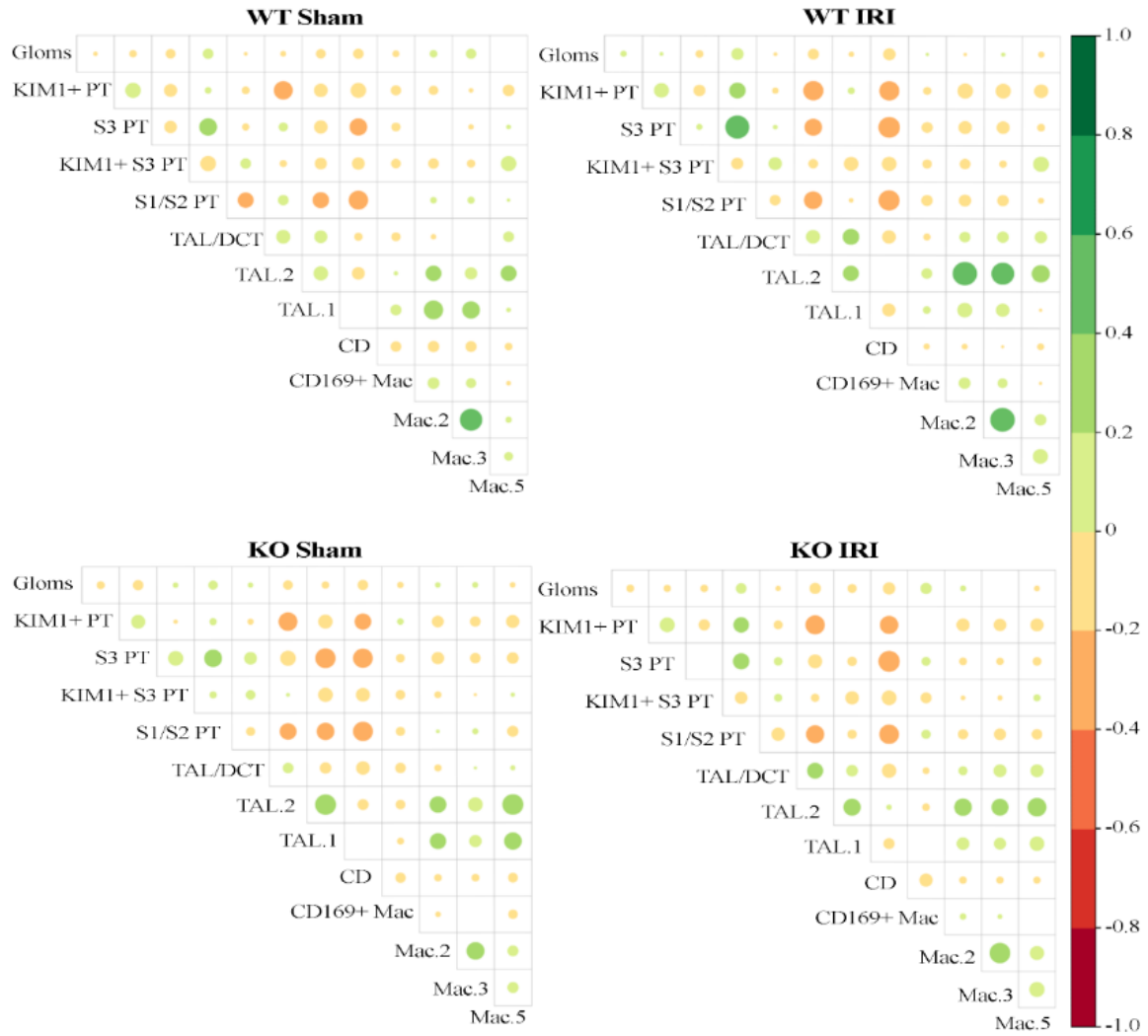


Figure 3.4: Myeloid niches change in injury and THP  $-/-$ . Pearson correlation plots show the associations of macrophage classes of interest with different sections of the nephron and their shifts in injury and THP  $-/-$

## Chapter 4 - Surveying the heterogeneity in the human renal cortex and its changes with disease

### Introduction

In order to elucidate the changes that occur in the renal cortex during disease, the CODEX multiplex imaging and analysis pipeline was applied to human kidney tissue specimens. We created a panel of antibodies, shown in Table 4.1, to not only annotate the cell populations and niches present in healthy reference tissue, but also to understand the changes that may occur in patients with AKI, as well as a variety of other diseases, including CKD, IgA nephropathy, and Systemic Lupus Erythematosus (SLE). Samples from patients with stone disease were considered “reference” tissues for this study, as those patients had no comorbidities or evidence of disease aside from stone formation. Stone disease samples with no comorbidities have been validated as a good source of reference tissue in previous studies (Winfree 2022, Sabo 2022).

With the five reference samples analyzed in this study, all major tubule segments were able to be accurately identified, as well as endothelial and vasculature cell types, and major classes of immune cells. When comparing reference tissue to any of the disease states, changes were seen in the proportions of immune cell populations, an increase in a class of stromal cells (potential features of fibroblasts versus altered endothelial cells) with disease, and a decrease in a population of proximal tubules that were also positive for thymocyte differentiation antigen-1 (also known as CD90) in disease. CD90 is a regenerative cell marker and is often associated with damaged or actively repairing cells. Studies that have been conducted on specimens from patients with DKD showed that while serum and urinary levels of CD90 went up with disease,

protein levels in renal tissue were significantly decreased (Wu 2020). A significant correlation between tubular CD90 and renal function was noted as well, indicating that CD90 is shed from proximal tubules as disease progresses (Wu 2020). Characterization of these cell types at the protein level using an imaging approach in the human kidney has not been previously performed.

## **Results**

### *Creating an atlas using reference tissue specimens*

In order to create a comprehensive protein-based imaging library of healthy renal cortex, five reference tissue specimens underwent CODEX multiplex imaging using the marker panel shown in Table 4.1 and combined into a single analytical space, as described in the previous chapter. Examples of each of the antibodies used are also shown in Figure 4.1. Using the Louvain unsupervised clustering method, we found a total of sixteen unique classes of cells (Figure 4.2). Within these sixteen classes, the expected major cell types were identified, including all sections of the nephron, vessels and other endothelial cells, and various immune cells. As was described in Chapter 3.2 with the mouse studies, putative cell classes were determined using violin plots of average marker intensity and then validated with back-mapping in the imaging data (not shown).

For the nephron segments, podocalyxin was used to mark the podocytes, LRP2 and AQP1 for proximal tubules, THP for the thick ascending limbs, E-cadherin for the distal nephron, and Cytokeratin 8 for the connecting tubules and collecting ducts.  $\beta$ -catenin was also used to mark the tubule epithelium through the whole nephron. For the vasculature,  $\alpha$ -SMA was selected to identify the arterioles and CD31 for other endothelial cells. Along with the major tubule segments, we also uncovered some

unexpected tubule subclasses, including a class of CD90+ proximal tubules and a class of PROM1+ (prominin-1 or CD133) proximal tubules (Figure 4.2). There were also two immune cell populations that were identified: one resident macrophage population, and a T cell population.

Using the cell classes defined in Figure 4.2, we then performed cell-centric neighborhood analysis in order to determine cell associations within niches and the distribution of specific cells, based on distance. Each tubule segment had their own niche, including the CD90+ proximal tubules (neighborhood 1, Figure 4.3). In total, there were four different neighborhoods with significant levels of at least one proximal tubule class. Another niche of interest was neighborhood 5, which showed a significant association between the resident macrophage population and the PROM1+ S1/S2 PT population, along with some of the endothelial classes. Based on recent data from the KPMP, PROM1+ proximal tubules may be associated with altered repair states (Lake 2022).

#### *Combining reference and disease specimens*

Four specimens from patients with different renal diseases were imaged in the same manner as the reference tissues and were added to the combined analytical space. Adding these disease specimens expanded the dataset to 169,802 cells, and the number of clusters identified with Louvain clustering increased to seventeen (Figure 4.4). The same major cell classes were identified, including the CD90 and PROM1+ proximal tubule clusters. The combined Louvain set was then separated to show changes in cell abundance in each cluster between the reference and disease tissues. Doing this showed a significant difference in two populations: the CD90+ proximal tubule population and a

population of stromal cells (Figure 4.4). The CD90+ proximal tubule population showed a decrease, whereas the stromal cell class showed a prominent increase with disease.

As was done with the reference tissues, neighborhood analysis was conducted on the combined dataset in order to see changes in the niches present in the various types of diseases included. Figure 4.5 shows a breakdown of the neighborhoods found in the combined dataset. Notable neighborhoods include 1, 3, 4, and 5, all of which have a high proportion of the stromal cells class and neighborhood 11, which contains the CD90+ proximal tubule population. For the neighborhoods containing stromal cells, distinctions can be made by the distribution of cells present. Neighborhood 1 has the largest proportion of this stromal cell class and contains DC/myeloid cells. Neighborhood 3 shows a correlation between stromal cells and PROM1+ proximal tubules. Neighborhood 4 contains a large proportion of CD4+ T cells. Lastly, neighborhood 5 indicates these stromal cells can also be associated with S1 and S2 proximal tubules.

#### *Changes in neighborhood proportions in disease*

When comparing the distribution of neighborhoods between reference and disease, neighborhood 1 shows a large increase in the disease group, while almost absent in the reference group (Figure 4.5). The proportion of neighborhoods 4 and 5 was also increased in the disease group, though not as dramatically as is seen with neighborhood 1. The CD90+ proximal tubule-specific neighborhood (neighborhood 11) was not present in the disease tissues but was very prominent in the reference set. Neighborhood 3 was the only neighborhood of interest that showed no significant change in disease.

To see if these changes were consistent between the four disease groups studied, we also examined the neighborhoods for each disease sample separately (Figure 4.5).

Neighborhood 1 was increased in all four disease samples, with IgA showing the largest increase. For neighborhood 4, the AKI sample showed the largest increase, and the IgA sample was similar to that of the reference sample. Neighborhood 5 showed a decrease in the IgA sample compared to reference, but the other three disease samples were increased compared to reference. As expected, neighborhood 11 was either small or nonexistent in all four disease samples, and neighborhood 3 only showed an increase in the CKD sample.

## **Discussion**

This study provided new insight into the renal cortex in both healthy reference and disease specimens. We were able to identify multiple cell types, encompassing each major segment of the nephron, vasculature and vessels, major immune cells, and injured cell types as well. There was a unique CD90+ proximal tubule population that was only present in the reference samples, a PROM1+ proximal tubule population that was present in both reference and disease groups, and a stromal cell population that was prominently present in the disease samples. CD90 has been associated with mesenchymal stem cells and a regenerative potential (Wu 2021). Therefore, a decrease in the abundance across all disease states included in our analysis could be explained by advanced disease and loss of repair potential. This decreased presence could also support what was suggested by Wu et al, that severe injury may cause a shedding of CD90 from the tubular epithelium (Wu 2020).

The PROM1+ proximal tubule population was present in both reference and disease tissues, with a slight increase in the disease tissues. This population was present in neighborhood 3, which also had a prominent association with the stromal cell class.

PROM1 has similar proposed functions to CD90 and has been seen in association with regeneration and repair (Shrestha 2021). Since the CD90+ proximal tubules and the PROM1+ proximal tubules were seen in separate populations and neighborhoods, this could indicate that these markers are labelling different cell types, the function of which is linked to their spatial distribution and the interacting cells within that microenvironment.

Another interesting population that was uncovered with the addition of disease specimens was the stromal cell population. When studying reference tissue alone, this population was not present, but it had a prominent presence in the disease tissues, indicating a potential association with injury or inflammation. Future studies that incorporate additional antibodies could uncover whether this population is made of several cell subtypes. With the current panel of markers used, we hypothesize that these are a stromal cell population, and the increased presence in disease tissue may be consistent with changes in fibrosis and inflammation.

There are a handful of weaknesses that come with this study, the first of which is the low number of samples investigated for each disease state. As this is one of the first studies using CODEX multiplex imaging to survey the human kidney, our primary goal was to create a representative sampling of healthy cortical tissue, and then expand the technology to study disease and validate its use on non-healthy tissue. We were successful with both parts of this goal, and future work will be to increase the sample size for each disease state, as well as include other pathologies such as diabetic kidney disease or focal segmental glomerulosclerosis. We also aim to expand the antibody panel and incorporate markers that could provide additional insights into pathways of disease.

While we created a robust structural panel, the immune and injury markers have room for improvement. The major immune cell classes were able to be identified with the current panel, but the specific cell subclasses were not investigated. Similarly, the injury markers were not fully investigated in this study, aside from CD90 and PROM1.

Because of the richness and depth of information present in this dataset, focusing on the proximal tubules and their injured subtypes represented one possible way to guide the analysis. With the nature of this methodology, the analysis could easily be adjusted to look at specific aspects of each disease state as well. Rather than focusing on damaged tubules, immune cells could be targeted for analysis, or the glomeruli. Vasculature could also be analyzed for changes in density or evidence of injury across various disease states.

## **Methods**

### *Tissue Sectioning*

10-micron sections were cut onto Poly-L-Lysine coated coverslips and stored at -80C overnight until staining the next day. Serial sections were collected for each biopsy.

### *Tissue Staining*

Upon removal from -80C coverslips were placed on dririte beads for two minutes to thaw. Samples were then placed in acetone for ten minutes to remove the rest of the OCT from around the tissue and the coverslip. After washing in acetone, coverslips were placed in a humidity chamber for two minutes, then rehydrated in a two-step hydration buffer wash. Tissues were then fixed in a mixture of PFA and hydration buffer for ten minutes. After fixing, residual fixative solution was rinsed with hydration buffer, and then coverslips were placed in staining buffer for thirty minutes, during which the



antibody cocktail was made for the samples. Tissues were allowed to incubate in the antibody cocktail overnight at 4C. After overnight incubation, tissues were washed of the staining solution in staining buffer, and then placed in a pos-label fixative solution for ten minutes. Tissues were washed again, fixed in methanol for five minutes, washed, and placed into a final fixative solution for twenty minutes. Coverslips were then stored in storage buffer and stored at 4C until imaging.

#### *Reporter Plate*

Reporter stock solution was created using nuclease free water, assay reagent, DAPI, and 10x CODEX buffer. Solution was distributed into the appropriate number of wells for the number of cycles, and up to three reporters were added to each well.

Imaging and Image Processing – Imaging of the coverslips was conducted using a Keyence BZ-X810 epifluorescent microscope, a 20x air objective, and filter cubes for DAPI, GFP, TRTIC, and Cy5. Images were stitched and processed using the CODEX Processing software. Processing included background subtraction to correct for autofluorescence, tissue drift compensation (cycle alignment), and deconvolution.

#### *Image visualization and analysis*

The resulting images were visualized using ImageJ/FIJI, and initial analysis was conducted using VTEA. Images were visually assessed for tissue and staining quality, before using unsupervised analysis to remove any potential artifacts. After sections were visually checked for staining and imaging quality, each sample underwent semi-supervised classification in order to ensure similar major cell types could be identified between each sample, using VTEA. After samples were validated, the resulting data was

combined into one analytical space in  $\mathbb{R}$ , allowing us to directly compare the samples to one another.

<b>Antibody</b>	<b>Significance</b>
CD8	CD8+ T Cells
CD20	B cells
CD45	Leukocytes
CD90	Differentiation
CD3	Pan T Cells
CD4	CD4+ T Cells
CD11c	Res. Dendritic
CD206	M2
CD45R0	Mem T Cells
MPO	Neutrophils
CD68	Macrophages
HLA-DR	APCs
AQP1	PT, TDL
E-cadherin	DCT, CD, Loop
B-catenin	Tubular epithelium
LRP2	PT
Fibronectin	Pre-collagen
Podocalyxin	Podocytes
Uromodulin	TAL
a-SMA	Arterioles
CD31 (PECAM1)	Endothelium
Cytokeratin 8	CNT and CD
Citruline H3	Netosis
OPN (SPP1)	Osteopontin
Ki67	Prolif. Cells
Vimentin	Fibroblasts
IGFBP7	Injury
KIM-1	Injury
pMLKL	Necroptosis
VCAM1	Non-repairing
ERG	Endothelial Nuclei
EGFR	Growth Factor
pcJUN	Stress kinase
PROM1 (CD133)	Fibrosis
FOXP3	T Regs
LC3	Autophagy

Table 4.1 - Antibodies used for CODEX multiplexed imaging on human renal cortex

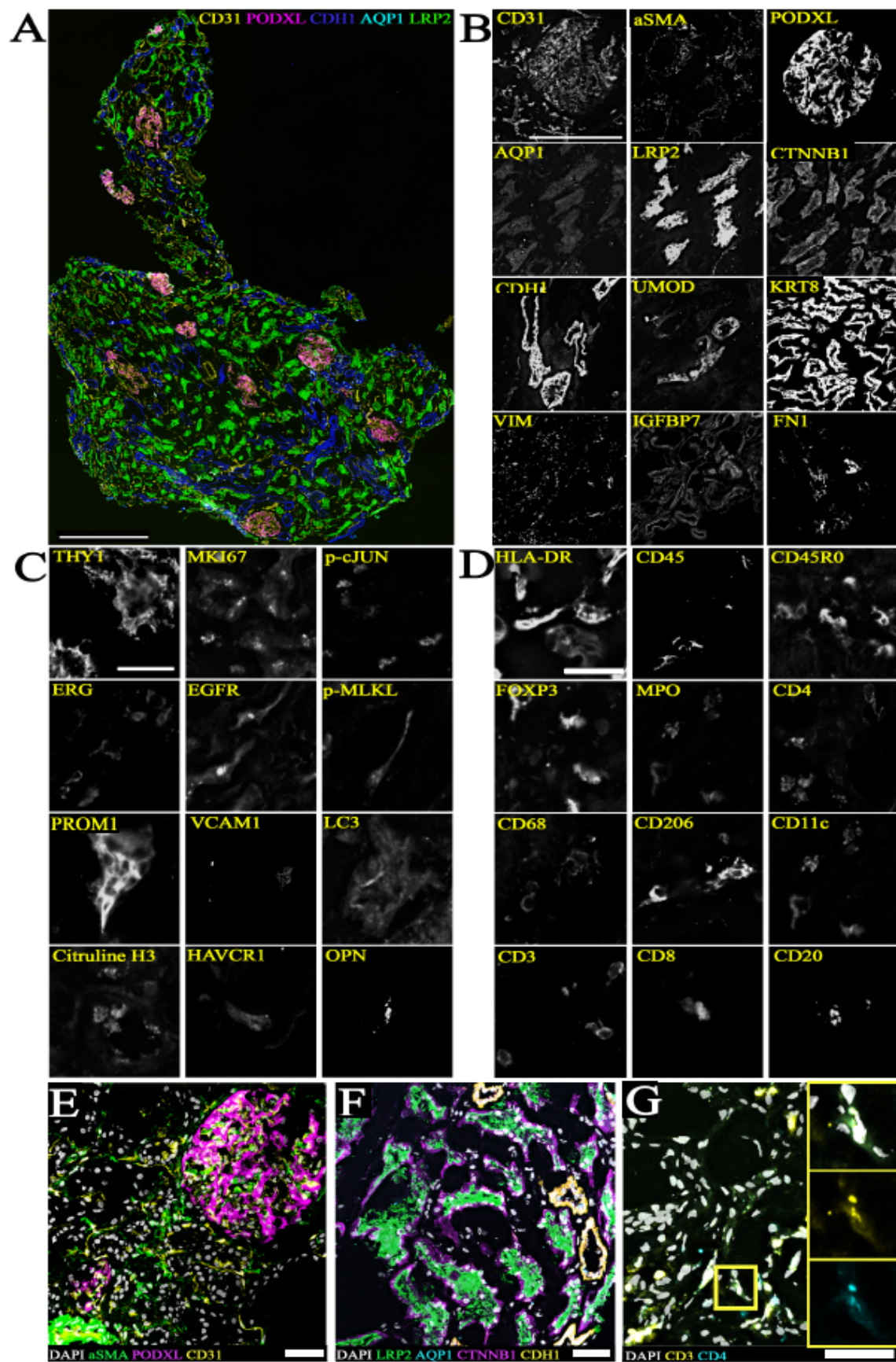


Figure 4.1: Staining panel utilized for the human CODEX experiments. A) Representative image from one of the reference specimens imaged. Channels included are CD31 (endothelium), PODXL (podocytes), CHD1 (tubular epithelium), AQP1 (proximal tubules) and LRP2 (proximal tubules). Scale bar is 500 microns. B) Example images of all of the structural antibodies used in the staining panel. All images are scaled the same, scale bar is 500 microns. C) Example images of cell state markers included in the staining panel. Scale is 200 microns. D) Example images of immune cell markers included in the staining panel. Scale is 200 microns. E) Composite image of the vascular-specific stains included in the staining panel. Scale is 50 microns. F) Composite image showing an example of tubule staining of both proximal tubules and distal convoluted tubules. Scale is 50 microns. G) Example region showing T Cell staining using CD3 and CD4. Insets highlight an example of overlapping staining between CD3 and CD4. Scale bar is 20 microns.

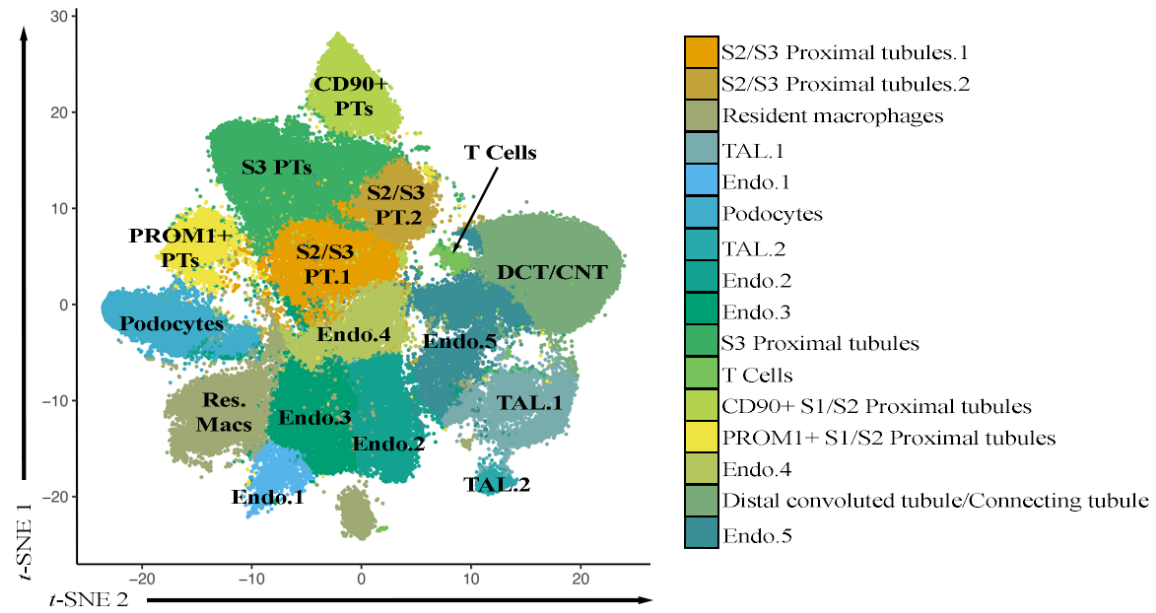


Figure 4.2: Louvain clustering of reference tissue identifies major cell types. tSNE plot showing the classes that were determined using Louvain clustering methods with segmented cells. Class identities label each cluster, and are listed with their cluster color association.

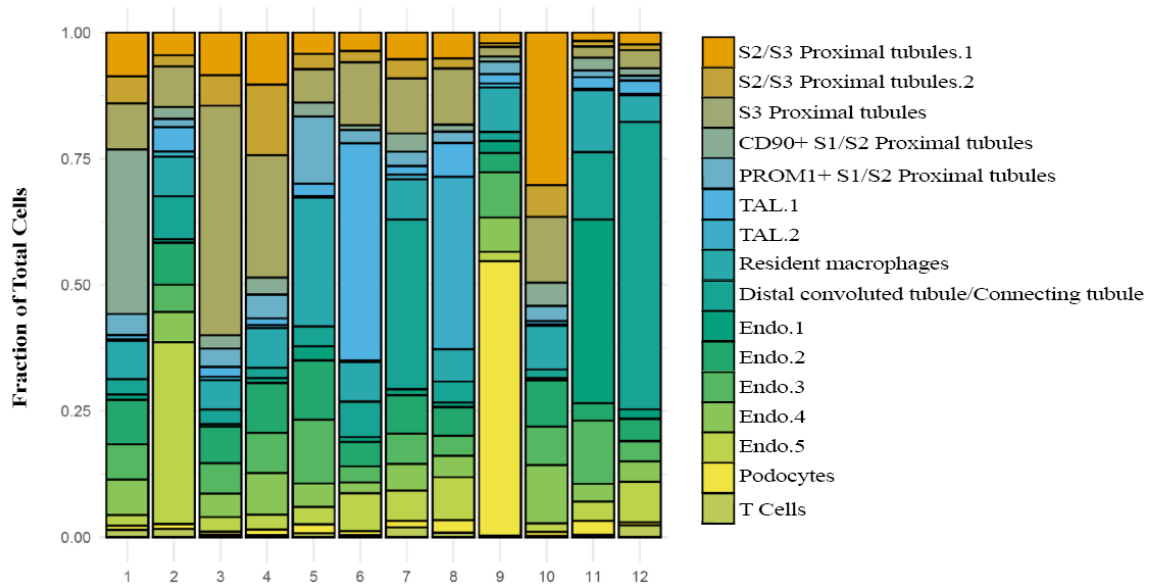


Figure 4.3: Neighborhood analysis of reference tissues. Stacked bar plot showing the distribution of cell classes from Figure 4.2 across 12 different niches. Bars represent proportion of each niche a specific group makes up.

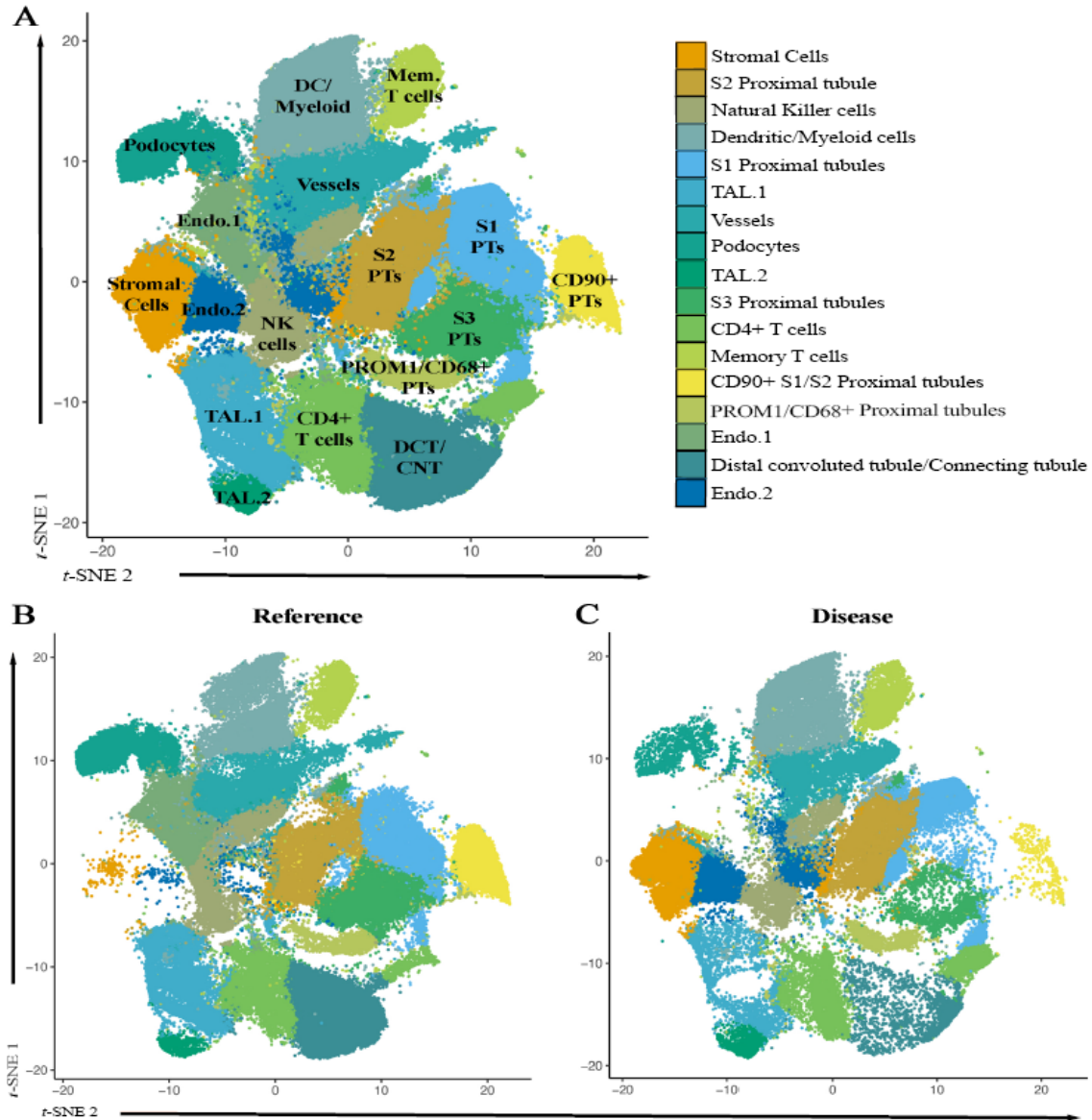


Figure 4.4: Louvain clustering of reference and disease tissues show changes in abundance of clusters A) tSNE plot showing the Louvain clusters found when combining reference and disease specimens. B) tSNE plot from A displaying cells from reference tissue specimens only. C) tSNE plot from A displaying cells from disease tissue specimens only



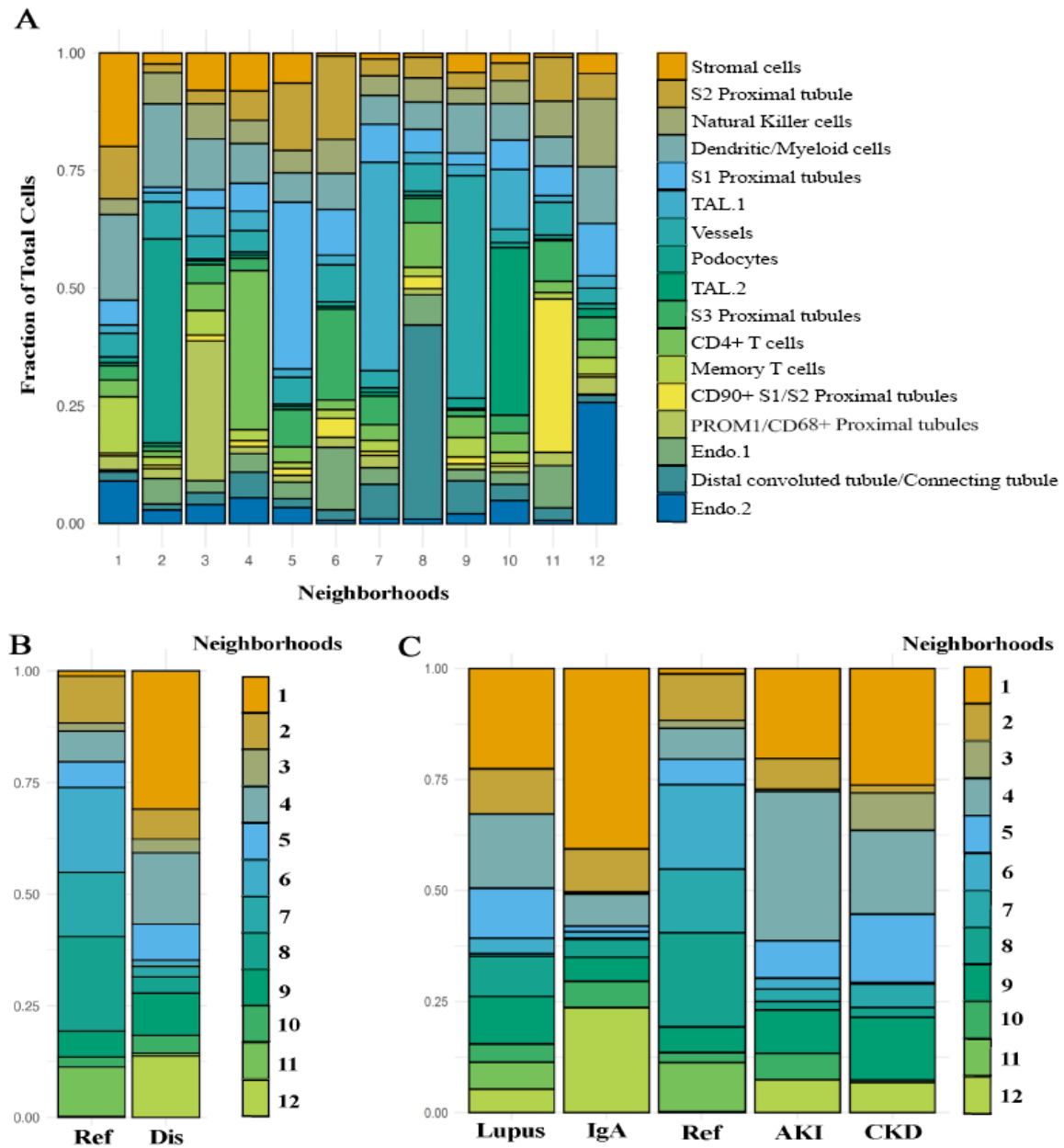


Figure 4.5: Neighborhood analysis of reference and disease specimens so unique injury niches. A) Stacked bar plot showing the niches present in the reference and disease specimens combined. B) Stacked bar plot showing niches of all reference versus all disease. C) Stacked bar plot showing niches of all reference versus each disease specimen individually

## Chapter 5 - CODEX Multiplex Imaging of the Renal Papilla

### **Introduction**

As mentioned in previous chapters, the human kidney is made up of distinct regions, each performing a specific and important role in maintaining proper kidney function. Of these regions, the papilla is one of the least studied and little is known about its exact role. Collecting ducts and the thin limbs of the loops of Henle are the main structural components of the papilla, along with vasculature and interstitial space. Some studies have found that the papilla may contain a niche of stem cells, though there is still some debate on this topic (Vanslambrouck 2011). There is a limited amount of information available on the papilla, leaving it an understudied mystery.

Understanding the structure of the papilla and the way cells interact with one another will be crucial in answering a lot of the questions surrounding the growth and development of RP and kidney stones. One of the main questions that remains unanswered is what happens to the papillary tissue when plaque starts to develop in the kidney. Current theories suggest that as plaque forms, it eventually breaks through the epithelial lining of the renal papilla and becomes exposed to the urine space, allowing stones to develop overtime (Kahn 2015). There are some persons that form plaque without ever having a stone event, though the true prevalence of that is unknown. Determining what changes in the papilla that allow the plaque to breach the epithelial layer is an important step in understanding the events leading to stone formation.

Included in this chapter is a manuscript summarizing work that was conducted in order to help characterize the papilla and elucidate the roles of the cells present in the space. Spatial transcriptomics and CODEX multiplex imaging were once again utilized in

tandem, this time on human papillary samples from either reference nephrectomies or kidney stone former that underwent surgery for stone removal. For this manuscript, I conducted all of the CODEX experiments, including development of the antibody panel and setting up/initiating the analytical pipeline. I was also tasked with overseeing the final interpretations of the data included in the following manuscript. (*Italicized text below is used by permission of the authors.*)

**5.1 – A spatially anchored transcriptomic atlas of the human kidney papilla identifies significant immune injury and matrix remodeling in patients with stone disease**

**Introduction**

The prevalence of kidney stone disease, or nephrolithiasis, is increasing in the US and around the world. Nephrolithiasis is associated with significant morbidity, impaired quality of life and significant health care utilization. This disease is complex, with a multifactorial etiology influenced by genetic and environmental factors (Worcester 2010) (Howles 2020). Despite decades of innovation and efforts by researchers to describe its pathophysiology, the precise mechanisms contributing to kidney stone formation remain poorly understood (Khan 2021). A key factor leading to this knowledge deficit is the paucity of data on the cellular and molecular makeup of the kidney papilla and its alteration with stone disease. In addition, the spatial distribution of various cell types and their association with mineral deposition (such as Randall’s plaque) during stone disease is largely unknown.

Experimental studies in rodent models of crystal formation and mineral deposition suggest that stone disease may be driven by inflammation, oxidative stress and osteogenic-like changes in the kidney papilla (Khan 2012, Joshi 2015, Khan 2016,

Taguchi 2017). However, human data in stone patients are often limited (Khan 2021). There is some evidence to suggest a role of the immune system in the pathogenesis of stone disease. For example, proteins associated with immune cell activation have been discovered in proteomic studies of kidney stones from patients (Mushtaq 2007, Canales 2010, Okumura 2013, Kusmartsev 2016, Tang 2019, Xia et al. 2021). However, it remains unclear if the identified proteins are directly involved in the formation of CaOx stones or if they are simply a byproduct of non-stone related events (Witzmann 2016). The enrichment of specific immune proteins can depend on the type of stone, such as the preponderance of neutrophil proteins in brushite compared to CaOx stones (Makki 2020).

Renal papilla samples from stone formers are very challenging to obtain as they require a biopsy during a nephrolithotomy surgical procedure. Molecular data from such specimens is more limited. In CaOx stone formers, Taguchi et. al. showed enriched gene expression of pro- inflammatory M1 macrophages by bulk microarray analysis of human papillary samples, thereby supporting an important role of macrophage activity in kidney stone disease (Taguchi 2016, Taguchi 2021). However, the complexity of immune cell types, their distribution and spatial neighborhoods are not known in humans. Such knowledge could be important to understand the mechanisms of stone pathogenesis, particularly to determine if immune activation is widespread or limited to cell niches associated with mineral deposition in the papilla.

Indeed, it is unclear if the underlying pathology in stone disease is limited to areas of plaque deposition or if it is more diffuse across the papilla. Technological advances such as single cell and spatial transcriptomics, and large-scale high-resolution imaging, allow for the spatial definition of cell types and states based on transcriptomics and

protein markers. These technologies can advance our understanding of the pathogenesis of nephrolithiasis by defining spatial niches of various cell types/states in stone disease and address existing gaps.

In this work, we procured difficult to obtain human kidney papilla biopsy specimens from stone formers and reference nephrectomy tissues to create a spatially anchored transcriptomic atlas of the renal papilla using integrated single nuclear RNA sequencing (snRNAseq) and spatial transcriptomic (ST). By using high-resolution large-scale multiplexed 3D and CODEX imaging, we defined the spatial localization and niches of specific cell subtypes of the human papilla and the changes in this landscape with stone disease. We discovered that areas of mineral depositions are immune active zones consisting of immune injury and matrix remodeling genes that affect multiple cell types extending beyond areas surrounding mineralization. Our studies also identified MMP7 and MMP9 as potential urinary biomarkers associated with stone disease and its activity.

## **Results**

### *Identification and localization of cell types in the kidney papilla*

We recently reported a comprehensive single nuclear RNA sequencing (snRNAseq) profile (over 200,000 cells) of the adult human kidney from the HuBMAP and KPMP consortia (Figure 5.1A) (Lake 2021). We leveraged this dataset to gain a deeper understanding of cell type diversity in the human kidney papillae and unique features compared to the cortical- medullary cell types. Renal papilla samples contributed 20,338 nuclei to this dataset (Figure 5.1B). These samples were acquired from papillary biopsies of CaOx stone formers or were dissected from reference nephrectomies. In

addition to the expected papillary cell types such as principal and intercalated collecting duct cells, descending and ascending thin limbs, papillary surface epithelial, stromal and endothelial cells (Figure 5.1C), notable differences in gene expression were observed between papillary and cortico-medullary principal (PC) and intercalated (IC) cells (Figure 5.1D). For example, the urea transporter UT2 (SLC14A2) and Aquaporin 2 (AQP2) were both upregulated in papillary PCs and ICs. In contrast, the expression of the epithelial sodium channel ENaC (SCNN1G, SCNN1B) and PTH receptor (PTH2R) were more abundant in the cortico-medullary nuclei. Further, the gene RALYL, encoding the RNA-Binding Raly-Like Protein and responsible for the cystic Bardet-Biedl Syndrome 1, was predominantly expressed in PCs outside the papilla (Figure 5.1D). Distinct sodium bicarbonate transporters were also expressed in papillary as compared to cortico-medullary cells. These findings highlight the unique physiological role of these papillary cells in regulating water and urea transport and acid base balance in this unique environment and may have relevance to the pathogenesis of cystic disease.

We then sought to orthogonally validate these cell types and spatially resolve them in papillary tissue from controls and nephrolithotomies of subjects with CaOx stones. We used snRNA-seq labels to resolve the ST gene expression profiles obtained from 10X Visium (Figure 5.1E-P). The integrated analysis showed the mapping of the appropriate histological structures with the papillary tubules (Figure 5.1F-G). The majority of papillary surface epithelial cells (PapE) mapped to the outer edge as expected (Figure 5.1E, H, N). Fibroblast and immune signatures were identified in all the samples tested. We found a unique population of undifferentiated cells that were enriched in injury associated genes and lacked a transcriptomic signature specific to a unique cell

identity (Figure 5.1B). Undifferentiated cells were more abundant in stone disease samples (Figure 5.1Q). ST data showed that these cells frequently localized near areas of mineralization and are likely a result of localized injury to the adjoining tubules (Figure 5.1H-J).

Further characterization of the PCs showed that in addition to the healthy PC1 population, a PC2 population enriched with stress/injury genes was identified. These principal cell subtypes were compared to the undifferentiated epithelial cell type that also exhibited an injury signature (Figure 5.1B). Stone samples had a higher proportion of PC2 (compared to PC1) and undifferentiated cells by both snRNAseq and ST (Figure 5.1Q). Both PC1 and PC2 cells expressed canonical papillary PC markers; however, PC2 cells also expressed injury markers such as VIM, JUNB, JUND, LCN2 and MAP1LC3B (LC3) (Figure 5.1R). The undifferentiated epithelial cells had greater expression of injury markers such as PROM1, IGFBP7 and SPP1 and likely represents a degenerative state.

To extend the transcriptomic cell type prediction to the protein level, we performed highly multiplexed CODEX imaging of reference tissues using 32 cell markers (Figure 5.1S-X). Applying unsupervised analysis and classification based on the markers used, the presence of various expected cell types was confirmed, mapped within the tissue, and aligned with the cell types from the transcriptomic datasets (Figure 5.1T and 5.1U). We confirmed the presence of a significant resident immune cell population, with a predominance of macrophages with high expression of CD206 (M2-Macrophages). CODEX analyses uncovered two populations of collecting duct cells in the papilla, CD1 and CD2, which predominantly consist of principal cells based on the distribution outlines in Figure 5.1C. These two populations were differentiated by the

expression of injury and renewal markers in CD2 such as LC3, p-MLKL, PROM1 and Ki67 and were consistent with the transcriptomic injury signature uncovered in PC2 cells. We also uncovered a population of undifferentiated epithelial cells (Figure 5.1T, 1U) whose protein expression profile also overlaps with the undifferentiated population uncovered by ST (high expression of IGFBP7 and PROM1). Thus, using snRNAseq, ST and CODEX we validated the cellular diversity in the papilla and identified new cell populations with plausible biological significance (see below).

Using CODEX, we then explored the population of stromal cells localized in the papillary interstitium, which was divided into separate cell classes based on an unsupervised analysis (Figure 5.1W). We uncovered and spatially mapped two populations of fibroblasts based on the expression of fibronectin (FN1), vimentin (VIM) and osteopontin (SPP1 or OPN). We also identified a population of myofibroblasts with high expression of  $\alpha$ -SMA (Figure 5.1X). The presence of fibroblasts in the papilla is consistent with our snRNAseq and ST findings in Figure 5.1E-1P.

#### *Transcriptomic signatures of CaOx stone formation within the renal papilla*

Using the snRNAseq data, we determined the differentially expressed genes (DEGs) between CaOx stone and reference samples for each cell type in the papilla (Figure 5.2 A-D). Multiple cell types in stone samples expressed increased levels of injury and stress genes such as SPP1, CLU, LCN2, S100A11, MMP7 and CD74. These injury genes were similarly upregulated in the cell signatures and global gene expression in the ST stone samples (Figure 5.2E-F). Pathway analysis detected significant enrichment of common pathways related to protein translation, among the cells from patients with stone disease. We also observed enrichment of pathways of interest (Figure



5.2 A- D), such as: leukocyte activation, response to oxidative stress, ossification, extracellular matrix organization in most cell types, which overlapped with enriched pathways obtained independently from the spatial transcriptomic analysis. The concordant results between technologies increase the confidence in the biological relevance of these pathways in the pathogenesis of stone disease.

To further gain insights into the pathogenesis of injury in stone disease, we looked in more detail at MMP7 expression, a gene involved in injury and matrix remodeling and consistently upregulated in the papillae from patients with stone disease. Figure 5.3 shows the spatial and relative gene expression maps of MMP7. Interestingly, in reference tissue, MMP7 was confined to CDs, but in stone patients MMP7 showed a diffuse expression pattern, which was consistent with the generalized increased expression observed in most cell types from the snRNAseq and combined analysis (Figure 5.2E and 5.2F).

#### *Regional analysis of mineralized and non-mineralized tissues*

Mineral deposition such as Randall's plaque formation is thought to play an important role in the formation of stone disease. However, plaque formation is frequently focal, and the cellular and molecular alterations present in the microenvironment of mineral deposits could be important in the pathogenesis of this disease. Supervised analysis of spatial transcriptomic profiles based on the selection of mineral deposits in a stone forming papilla are shown in Figure 5.4. The results indicate that transcript signatures of genes such as NEAT1, CHIT1, LYZ, SPP1 and MMP9 are upregulated in areas contiguous to mineralized tissue compared to regions more distant (non-contiguous) to mineral (Figure 5.4). These genes are also associated with pathways of leukocyte

activation and response to oxidative stress. The expression of genes involved in macrophage activation such as MMP9 and CHIT1 (Figure 5.4B) was upregulated in the area of mineralization as compared to the non-contiguous region.

We next wanted to better define the niche of the mineralization nidus and understand its contribution to injury, particularly with our findings of enrichment of immune cell marker genes and their association with mineral deposition. We used CODEX multiplexed imaging in conjunction with a panel of antibodies directed to different immune cell types (Figure 5.5). We took advantage of the autofluorescence properties of mineral deposits (Figure 5.5A-B), whereby the plaque can be identified without staining (Makki 2020, Winfree 2021). The main cell clusters identified in reference tissue (Figure 5.1T-U) were also identified here, except that there was marked expansion of the immune clusters (Figure 5.5B). Additional unsupervised analysis (Figure 5.5C) was performed on the CD45<sup>+</sup> cell clusters from the initial analysis (Figure 5.5B), which resolved immune cells into major lymphocyte and myeloid clusters. The latter can be broadly divided into three categories based on markers such as CD68 and CD206, which correspond to an inflammatory (M1), alternatively activated (M2) and intermediate phenotype (M1/M2). Mapping back immune cells to the tissue images reveals that certain areas of plaque deposition serve as a nidus for immune activation (Figure 5.5D), where the deposited mineral is surrounded by inflammatory macrophages (M1 and M1/M2), which are known to be antigen presenting cells (APCs) (Figure 5.5E).

At the periphery of this immune nidus, these APCs interact with CD4<sup>+</sup> T and B cells, a phenomenon consistent with classic immune activation and synapse formation (Figure 5.5E). Interestingly, not all the plaque areas are involved with immune activation,

and neighboring areas with mineral did not have significant immune cells. We then examined the distribution of other interstitial cell populations such as fibroblasts and myofibroblast in these areas (Figure 5.5F-G). The plaque areas without immune activity had significant fibroblast infiltration (Figure 5.5H). Cumulatively, these data demonstrate that the presence of plaque is immunogenic. It elicits a varied immune response with a defined progression from myeloid to a mixed lymphocytic infiltrate and a non-overlapping fibrogenic response consisting of activated fibroblasts and myofibroblasts for repairing the injured tissue.

*Large scale 3D imaging and tissue cytometry establishes inflammatory stress signaling and macrophage activation as cardinal features of stone disease*

Next, we wanted to determine if immune activation and oxidative injury are cardinal features in the papilla of CaOx stone forming patients, independent of large mineral deposits. Using quantitative large-scale 3D imaging and tissue cytometry on papillary tissue specimens from controls and subjects with CaOx stone disease and no visible mineral deposits (N=4 each group), we quantified the expression and distribution of phosphorylated c-JUN (p-c-JUN, marker of oxidative stress and stress kinase activation) and CD68 (marker for inflammatory macrophages) (Figure 5.6). Patients with CaOx stones compared to controls had a significantly higher abundance of CD68+ macrophages (3.4 +/- 1.4 vs. 1.2 +/- 1.1 % of total cells, respectively; p=0.03) and p-c-JUN+ cells (12.4 +/- 4.0 vs 4.0 +/- 3.8 % of total cells, respectively, p=0.01) than non-stone formers. Macrophage infiltration was diffuse, and activation of c-JUN was not restricted to a specific cell type (Figure 5.6D), which is consistent with the findings from

snRNAseq and transcriptomic analyses suggesting increased stress signaling across multiple cell types in the papillae of stone patients.

*MMP7 and MMP9 levels are increased in urine of kidney stone patients and correlate with disease activity*

The snRNAseq and ST datasets revealed upregulation of MMP7 gene expression in the papillae of patients with stone disease and the upregulation of MMP9 gene expression in regions of mineralization. While these two matrix remodeling genes could explain some of the mechanisms behind papillary stone-associated injury, we next asked if their urinary secretion can also screen for stone disease activity. To this end, we assayed for MMP7 and MMP9 in urine sample from a cohort of 55 patients with normal kidney function separated into 3 groups (Figure 5.7): 1) healthy controls with no known clinical history of stones, 2) inactive CaOx stone formers with a known clinical history of stones but without a recent stone event and 3) active CaOx stone formers undergoing surgery for stone removal. Our results show that the levels of MMP7 are increased in the urine of CaOx stone patients without active disease compared to healthy subjects ( $4.8 \pm 6.1$  vs.  $1.6$  ng/mg Cr, respectively;  $p=0.01$ ). MMP9 was also significantly higher in the urine of inactive stone patients compared to healthy controls ( $1.8 \pm 3.7$  vs.  $0.18 \pm 0.17$  ng/mg Cr, respectively;  $p=0.02$ ). In active stone formers, we observed even higher levels of urinary MMP7 ( $8.1 \pm 6.6$  ng/mg Cr;  $p=0.0004$  vs. controls and  $p=0.47$  vs. inactive stone formers) and MMP9 ( $8.0 \pm 10.7$  ng/mg Cr;  $p < 0.01$   $p < 0.0001$  vs. controls and  $p=0.01$  vs. inactive stone formers). These results suggest that both MMP7 and MMP9 are potentially important markers to monitor stone disease activity.

## Discussion

In this work, we utilized snRNA sequencing, spatial transcriptomics, and large-scale multiplexed imaging to establish a spatially anchored cellular and molecular atlas of the renal papilla in non-stone and kidney stone disease tissues. A full landscape of papillary cells was defined, including the presence of papillary surface epithelial cells, stromal and immune cells, unique subtypes of principal cells, and an undifferentiated epithelial cell type which localized to regions of injury or mineral deposition. Despite the focal nature of mineral deposition in stone disease, we showed that injury pathways are globally upregulated across multiple cell types within the papilla. Commonly enriched signaling pathways in stone disease such as leukocyte (myeloid) immune activation, oxidative stress and matrix remodeling were demonstrated using orthogonal approaches, thereby enhancing our confidence in the findings. We defined the microenvironment of plaque as an active immune zone with antigen presenting inflammatory macrophages interacting with T cells, but also demonstrated the presence of an immune lifespan around mineral deposition ranging from inflammation to fibrosis. Finally, MMP7 and MMP9 were identified as two proteins linked to active stone disease and mineralization within the papilla. The levels of MMP9 and MMP7 in the urine were significantly higher in patients with history of stone disease compared to healthy controls, and correlated with disease activity.

Defining the cellular and molecular landscape in the human papilla is an important first step to understand the pathogenesis of nephrolithiasis and identify potential targets for therapy. An important strength of our study is the utilization of rare and highly valuable papillary biopsy specimens obtained from stone patients. The

uncovered atlas of the renal papilla harbored expected cell types such as the principal, intercalated, ascending and descending thin limbs, and endothelial cells. Compared to cortico-medullary cells, papillary collecting duct cells displayed a unique gene expression signature that is consistent with the physiological milieu within the papilla. For example, the high expression of urea transporters is consistent with gene expression data from rodents (Fenton 2005). Interestingly, the papilla was enriched in two types of principal cells, PC1 and PC2, which frequently co-localize in the same collecting ducts. PC2 exhibited a transcriptomic signature of cell stress and was more prevalent in specimens from subjects with stone disease. The biological significance of these two populations requires further investigation, particularly in establishing whether the injury signature of PC2 is a key contributor to the immune activation observed in stone disease.

Another cell type of interest was the “undifferentiated” snRNAseq epithelial cell cluster. Its signature did not align completely with a specific epithelial cell type but exhibited gene expression features of injury and degeneration. We posit that that this cluster may represent a final common injury phenotype derived from epithelial cells with multiple origins. This cell type was more frequently mapped in the stone samples and was associated with areas of mineralization in ST. In an orthogonal approach with CODEX, we uncovered an undifferentiated cell population with protein signatures overlapping with the transcriptomic features of the snRNAseq cluster. Spatial mapping suggested that these cells are likely a mixture of injured thin limbs and papillary epithelium, which is consistent with the location of these cells in the UMAP space. A signature of injury in thin limbs is concordant with previous data from our group showing

that Randall's plaque begins in thin limb cells (Evan 2003). This injured population and its potential association with pathology in the papilla needs further exploration.

Comparing stone to reference samples using snRNA and spatial transcriptomics independently uncovered common DEGs and enriched pathways in stone disease. In snRNA and ST analyses, many of the genes and injury pathways uncovered were common among various cell types (epithelia, stromal and immune), suggesting that the injury signature associated with stone disease could reflect a global injury to the stone forming papilla. Our data provide important human tissue context to the previously reported hypotheses, and some of the experimental models of stone formation which involved inflammation, leukocyte activation (macrophage activity), ROS and ossification-like events (Khan 2012, Khan 2014, Joshi 2015, Joshi 2015, Taguchi 2016, Taguchi 2017). Our spatial transcriptomic mapping of gene expression in stone disease agrees with, and extends the work of Taguchi and colleagues, who explored genome-wide analysis of gene expression on renal papillary RP and non-RP, and showed upregulation of LCSN2, IL11, and PTGS1 in the RP patient tissue (Taguchi 2017). RP has been previously described as the interstitial mineral deposition at the tip of the renal papillae that can serve as the origin for CaOx stone growth (Evan 2006, Daudon 2015). This immune active state in the regions of papillary mineralization has a molecular profile comparable to vascular inflammation leading to atherosclerotic disease, which has been proposed to play a pathogenic role in mineral deposition and stone disease (Kumada 2004, Abbas 2014, Bird 2017, Li 2020).

Our work particularly underscores the importance of immune system in the pathogenesis of stone disease, mapping significant populations of both the inflammatory

M1 macrophage and the alternatively activated M2 macrophage within the papilla. An intermediate phenotype M1/M2 was particularly abundant in areas around mineral deposition, highlighting that these two phenotypes likely represent a spectrum that may modulate disease activity (Yunna 2020, Taguchi 2021, Taguchi 2021). This is consistent with previous reports by Khan and others from experimental models (de Water 1999, Khan 2004, Joshi 2015, Taguchi 2016, Xi 2019, Taguchi 2021), but is uniquely demonstrated here in the human papilla. The presence of inflammatory macrophages and antigen presenting cells, surrounding by CD4+ T cells suggest a nidus for antigen presentation around plaque. Interestingly, in the same papillary specimen, we also uncovered a significant population of fibroblasts around an area of RP with less immune activity. This finding agrees with the matrix remodeling transcriptomic signature observed, which frequently results from chronic non- resolving inflammation. This is also consistent with recent findings by Canela et al. showing fibrosis and immune signature derived from imaging of CaOx stones with RP (Canela 2021).

Cumulatively, these findings indicate that mineral deposits likely trigger a canonical immune injury pattern, which extends beyond the areas of mineralization and affect multiple cell types. Our data suggest that there could be various stages and biological responses to mineral deposition, ranging from an active acute inflammatory reaction, to established fibrosis secondary to chronic inflammation. Injury and inflammatory macrophage infiltration were demonstrated in biological replicates using 3D imaging and cytometry. Heavy mineral deposition was not obvious in the tissues analyzed by 3D imaging which raises a possibility of factors other than heavy mineral deposition leading to injury and immune activation, or could reflect earlier stages of



diffuse papillary injury that precedes plaque deposition. Our data suggest that papillary injury triggers pro-fibrotic signaling and a vigorous matrix remodeling program. Indeed, our studies uncovered two matrix metalloproteinase molecules, MMP7 and MMP9, that are associated with stone disease and mineral deposition, respectively.

Matrix metalloproteinases (MMPs) degrade extracellular matrix proteins during growth, tissue remodeling and disease processes, and are secreted by various cell types including fibroblasts and leukocytes (including macrophages) (Cui 2017). Some MMPs control leukocyte migration and can modulate the immune response by biochemical cleavage of cytokines and chemokines (Elkington 2009). MMP7, or matrilysin, is thought to modulate innate immunity and leukocyte influx, and plays a critical role in extracellular remodeling (Manicone 2008, Bulow 2019, Burke 2004).

However, it is typically not expressed at the protein level in the renal cortex in healthy states (Zhou 2017, Fu 2019) but its expression and activity are increased in the setting of kidney disease. There are no previous studies that have investigated MMP7 in the human papilla. Furthermore, there are conflicting data about the role of MMP7 in experimental models of kidney disease. MMP7 is thought to mediate kidney fibrosis in unilateral ureteral obstruction models, and its levels are elevated in patients with CKD (Zhou 2017, Surendran 2004). However, MMP7 can also protect against acute kidney injury. In our papillary, non-stone, reference tissue, the transcriptomic signature of MMP7 was predominantly localized to collecting duct cells. In stone biopsy specimens, the expression of MMP7 was no longer limited to the collecting duct cells. snRNA and spatial transcriptomics were consistent in showing upregulation of MMP7 expression in various cell types within the papilla. We propose that induction and release of MMP7 in

various cell types is likely part of the matrix remodeling program induced by injury. The induction of MMP7 could therefore be a valuable indicator of papillary injury associated with stone disease.

MMP9 (macrophage gelatinase) is another MMP that was uncovered by our studies in association with mineral deposition. Our spatial transcriptomic analysis showed enriched expression of MMP9 in areas of mineral deposition, which co-localizes with OPN expression. Indeed, MMP9 gene polymorphisms are associated with nephrolithiasis (Mehde 2018). MMP9 is upregulated by classically activated macrophages during an inflammatory response, and is also expressed by other inflammatory cells and osteoclasts (Hanania 2012, Wang 2013, Jager 2016). MMP9 is proposed to play a role in renal fibrosis and epithelial to mesenchymal transition (Tan 2010, Tan 2013). It also interacts with OPN to enhance macrophage chemotaxis and fibrosis (Tan 2013). More recently, experimental studies by Wu et. al. suggested that activation of ROS in kidney tubular epithelial cells by way of the NK- $\kappa$ B/MMP-9 pathway promotes crystal deposition in the kidney (Wu 2021). Therefore, upregulation of MMP9 could be an indicator of crystal deposition, immune activation, and transition towards a profibrotic phenotype.

Since our tissue work suggested a potential role for MMP7 and MMP9, we investigated whether measuring these molecules in the urine could be useful in patients with stone disease. We found that both MMP7 and MMP9 are increased in patients with stone disease and their levels correlate with disease activity. MMP7 has been previously studied as a potential biomarker for predicting risk of acute kidney injury and CKD progression (Liu 2020). MMP7 correlated with fibrosis scores on kidney biopsies and was also found useful to predict IgA nephropathy progression (Yang 2020). More

recently, MMP7 levels were also elevated in patients with hypertension who developed CKD (Sarangi 2022). MMP9 levels have also been studied in the setting of diabetic kidney disease and found to be elevated in patients with macroalbuminuria (Pulido-Olmo 2016, Garcia-Fernandez 2020). To our knowledge, our study is the first to show that the urine levels of MMP7 and MMP9 are elevated in patients with stone disease compared to non-stone forming kidney subjects, particularly in the absence of a clinically detectable kidney function impairment. MMP7 and MMP9 urine levels are higher, particularly for MMP9, in patients with symptomatic active stone disease. Large studies are needed to define the utility of these markers in the management of patients with kidney stone disease. For example, longitudinal measurements of these markers and their changes may help predict stone recurrence and response to therapy, supplementing computed tomography to reduce lifetime radiation exposure in stone formers. Indeed, our results provide a solid rationale to study these markers in the context of a large clinical trial.

Our study has limitations. Renal papilla samples from stone formers are challenging to obtain as they require a biopsy during a nephrolithotomy surgical procedure. Fortunately, our investigative team has substantial experience obtaining these samples (Evan 2006, Evan 2018). The number of tissue specimens used to generate the transcriptomic and imaging datasets was relatively small, underscoring the importance and scarcity of these samples. Despite the sample size, the findings were validated by orthogonal methods and the importance of the pathways and molecules uncovered were ultimately linked to urinary measurements in a larger clinical cohort. Further, the co-clustering of nuclei from the renal papilla with a publicly available snRNAseq whole kidney atlas (of more than 200,000 nuclei) allowed substantially more power to

distinguish granular cell subtypes and cell states. Due to the cost prohibitive nature of multi- omics studies, our approach of discovery in a small sample size and validation in a larger cohort serves as a viable model for hypothesis driven future studies economizing on tissue and maximizing validation efforts on samples collected through non-invasive methods over time. As discussed, the findings of elevated MMPs could also be observed in other forms of kidney disease. However, the cohorts used here had normal kidney function, and the potential utility of these markers in tracking stone disease activity, particularly in patients with normal kidney function, is thereby not diminished. We studied CaOx kidney stone formers, which is the most common type of kidney stones. The applicability of our findings to other types of stone disease will need to be established by additional studies.

In conclusion, our integrated multi-omics investigation uncovered the complexity of the human kidney papilla and provides important insights into the role of immune system activation and mineral deposition. We established the diffuse injury associated with nephrolithiasis and highlight the importance of a matrix remodeling program in the kidney papilla. Particularly, we identified MMP7 and MMP9 as potential molecules that may serve as noninvasive markers of kidney stone disease course and activity. This investigation provides a strong foundation for future studies that explore the pathogenesis of kidney stone disease and the application of precision medicine to patients with nephrolithiasis.

## Methods

### *Human samples sources*

***Single nuclear RNA sequencing sample sources*** snRNAseq data from 36 subjects comprising 203,702 nuclei were obtained from the HuBMap (<https://hubmapconsortium.org/hubmap-data/>) and KPMP (<https://www.kpmp.org>) datasets that are now publicly available (GSE169285) (Lake 2021). Single cells were isolated from frozen tissues as previously described (Lake 2021). Of the 36, five subjects provided two samples each for a total of 41 samples. The presence of cortex, medulla, or papilla was defined by adjacent cross sectional Periodic Acid Schiff-stained histological sections. In these 41 samples, there were 29 samples with cortex, 14 samples with medulla, and five samples with papilla. Seven subjects' samples contained both cortex and medulla. Of the five papilla samples, three were from CaOx stone formers obtained at Indiana University (see below) and two were from non- stone formers.

***Human kidney papillae samples*** Patients with idiopathic CaOx stones underwent a renal papillary biopsy procedure during a clinically indicated percutaneous nephrolithotomy for stone removal (Evan 2003), approved by the IRB of Indiana University (IRB # 1010002261). Informed consent was obtained from all study participants. Human reference (non-stone formers) nephrectomy papillary specimens without evidence of renal disease were obtained from the Biopsy Biobank Cohort of Indiana (Eadon 2020) (IRB #1906572234). Following extraction, papillary tissues were frozen on dry ice in OCT medium. For ST and CODEX imaging studies, two reference and three CaOx papillary specimens were used. For validation studies with 3D imaging,

kidney papillary sections were obtained from four additional reference and four CaOx biopsy specimens.

***Cohorts for urine MMP7 and MMP9 measurements*** Urine specimens from 20 healthy participants (Normal) with no personal or family history of kidney stones and 18 patients with a history of CaOx stones (Non-active stone formers) were obtained from an ongoing study at the University of Chicago (IRB protocol 09-164B). Participants were studied in the General Clinical Research Center at the University of Chicago, and the urine specimens used in these studies were obtained during the same morning period. Urine samples from 18 patients with active stone disease were obtained during elective percutaneous nephrolithotomy for stone disease at Indiana University (IRB protocol 1010002261).

***snRNAseq and processing***

From an integrated HuBMAP and KPMP atlas of renal cell types (Lake 2021), the snRNAseq portion of the Seurat object, including papilla samples, was reproduced to identify cell type clusters. For quality control, 10X snRNAseq cell barcodes passing 10X Cell Ranger filters were used for downstream analyses. All mitochondrial transcripts were removed. Doublets were identified and removed with DoubletDetection software (v2.4.0) (Gayoso 2020). The 41 samples were merged and only nuclei barcodes with more than 400 and less than 7500 genes detected were maintained in the merged atlas. A gene unique molecular identifier (UMI) ratio filter was applied using Pagoda2 to remove low quality nuclei ([github.com/hms-dbmi/pagoda2](https://github.com/hms-dbmi/pagoda2)) (Barkas 2021). Expression was calculated in 10X Cell Ranger v3 after demultiplexing and barcode processing. The

GRCh38 (hg38) reference genome was used for the snRNAseq and subsequent spatial transcriptomic datasets.

*snRNAseq clustering and annotation*

snRNAseq cluster definitions were adopted from the current version of the combined HuBMAP and KPMP atlas (Lake 2021). Briefly, nuclei were clustered with pagoda2. Total counts per nucleus were normalized, batch effect was corrected, and principal component analyses were performed using all significant variant genes (N= 5526). Initial cluster identities were determined by the infomap community detection algorithm. Using a primary cluster resolution of  $k = 100$ , all principal components and annotations were imported into Seurat v4.0.0 to create a merged uniform manifold approximation and projection (UMAP). Standardized anatomical and cell type nomenclature was used to annotate cell types and subtypes, based on the collaborative KPMP and HuBMAP definitions. These definitions were based on published datasets and the expertise of consortium pathologists, biologists, nephrologists and ontologists (El-Achkar 2021, Lake 2019, Gerhardt 2021, Chen 2021, Ransick 2019, Borner 2021). Specifics of the cluster decision tree algorithm have been previously described (Lake 2021). Within the integrated HuBMAP and KPMP atlas, putative adaptive and degenerative cell states were identified in epithelial sub-clusters with at least one of the following: reduced genes detected, higher mitochondrial transcript amount, higher ER associated transcript number, increased expression of known injury markers (e.g., IGFBP7, HAVCR1, LCN2, CST3, etc.), or enrichment in samples with acute or chronic kidney disease. Markers of these cell states were identified using the Seurat function “FindConservedMarkers” with the following parameter settings: `grouping.var =`

"condition.11", min.pct = 0.25, and max.cells.per.ident = 300. The gene set for the adaptive and degenerative cell states were trimmed to include only enriched genes at a p value < 0.05 and mean log2 fold change > 0.6. Due to the consistent loss of epithelial cell type specific markers, all nuclei within the adaptive and degenerative cell state clusters were merged into a single undifferentiated epithelial cluster within the papilla snRNAseq UMAP.

#### *Visium Slide preparation, mRNA extraction and sequencing*

Frozen 10 micron sections were mounted onto etched frames of the Visium spatial gene expression (VSGE) slides according to 10x Genomics protocols (Visium Spatial Protocols—Tissue Preparation Guide, Document Number CD=G000240 Rev A, 10x Genomics). Tissue sections were fixed with methanol, subsequently stained with H&E and imaged by bright-field microscopy. Microscopic images were acquired according to protocols described in 10x Genomics protocols (Technical Note - Visium Spatial Gene Expression Imaging Guidelines, Document Number CG000241, 10x Genomics). H&E-stained sections were imaged with a Keyence BZ-X810 microscope equipped with a Nikon 10× CFI Plan Fluor objective at 0.7547 um/pixel and image resolution of 1920x1440. Images were collected as mosaics of 10x fields. Stained tissues were permeabilized for 12 minutes. mRNA bound to oligonucleotides on the capture areas of the Visium slides was extracted. cDNA libraries were prepared with second strand synthesis and sequenced utilizing the NovaSeq 6000 Sequencing system (Illumina) in the 28 bp + 120 bp paired-end sequencing mode.



### *Spatial transcriptomics expression analysis*

Using Space Ranger 1.2.0 with the reference genome GRCh3-2020-A, samples were mapped, and counts were generated that corresponded to the barcoded 55 micron spot coordinates within each fiducial frame. This allowed association of read counts with their location within the H&E image. Space Ranger calculated differential expression between assigned clusters using sSeq and edgeR. The data were normalized by SCTransform and merged to build a unified UMAP and dataset as previously described (Melo Ferreira 2021). All feature plots show expression after normalization.

### *Selection of histologic phenotypes*

Kidney stone papillary tissue biopsies were manually annotated utilizing the 10x Genomics Loupe Browser (10x Genomics Loupe Browser 5.0.0). Specific regions of the stone tissue papilla were categorized as either non-mineralized, contiguous to mineral, or mineralized regions. Spots directly overlying evident mineral precipitation were designated as mineralized; spots falling within a three-spot radius of the annotated mineral precipitation were categorized as “contiguous” to mineral; all remaining spots were designated as non-mineralized.

### *Pathways and gene expression analysis*

Differential expression comparisons across samples were performed using R and the R packages ReactomePA and ClusterProfiler as previously described by Ferreira et al. (Melo Ferreira 2021). The DEGs in each comparison were found with the Seurat function FindMarkers and tested with a Wilcoxon’s rank sum test. Pathway enrichment for those genes was performed with the R packages ReactomePA (Yu 2016) and ClusterProfiler (Yu 2012).

### *Label Transfer*

Seurat v3.2 was used to accomplish label transfer from snRNA-Seq cell types and cell states to spatial transcriptomic spots in each sample. For deconvolution analyses, a Seurat v3.2 anchor methodology was used to transfer single-cell cluster information to Visium data as described (Melo Ferreira 2021). Each spot receives a probability or transfer score for its association with a given snRNA-Seq cell type or cell state cluster. The transfer scores are summed, and each spot is deconvoluted with the fractions of the spot corresponding to the relative proportion of transfer score of each contributing snRNAseq cluster. A pie chart is displayed over the spatial transcriptomic sample image.

### *Tissue Processing, Immunofluorescence Staining and Large-Scale 3D Confocal Imaging*

Papillary biopsies were immediately immersed in OCT medium and frozen on dry ice. For immunofluorescence analysis, tissues were cryosectioned (Leica Biosystems, Wetzlar, Germany) at 20 micron thick sections. Sections were washed in PBS, fixed for 4 hours at room temperature in 4% PFA. Next, the sections were washed in PBS two more times, and then blocked in 10% normal donkey serum for two hours at room temperature. Primary antibodies were added in blocking buffer and tissues were incubated at room temperature overnight. When targeting intracellular antigens, permeabilization was performed using 0.2% Triton X (Santa Cruz Biotechnology, Inc., Dallas, TX) (Gildea, 2017) (El-Achkar et al. 2007). The following primary antibodies were used for detection: anti-aquaporin 1 (Santa Cruz Biotechnology, Inc., Dallas, TX; sc-9878), anti-CD68 (Agilent Technologies, Santa Clara, CA; M087601), anti-phospho-c-JUN (Cell Signaling Technology, Danvers, MA; 9261). After washing with PBS, the following Alexa Fluor (ThermoFisher Scientific, Waltham, MA) dye-conjugated secondary antibodies were

added: donkey anti-mouse-488, anti-mouse-568 and anti-rabbit-647. 4',6-Diamidino-2-phenylindole (DAPI) (Abcam, Cambridge, United Kingdom; ab228549) was used for staining nuclei. Subsequently, sections were washed three times for 30 minutes each in PBS and then fixed in 4% paraformaldehyde for an additional 15 minutes. After a final wash in PBS for 30 minutes, sections were mounted on a glass slide using ProLong<sup>TM</sup> Glass Antifade Mountant, (Thermo Fisher Scientific, Waltham, MA; REF# P36980). Images were sequentially acquired in four separate channels using the Leica SP8 confocal microscope and collecting whole volume stacks using 20xNA 0.75 objective with 1.0-micron spacing. Stacks were stitched using Leica LAS X software to generate large-scale 3D images. A negative control without primary antibody was used to ensure the absence of nonspecific binding of secondary antibodies. Microscope settings were identical among imaging sessions for each specimen.

### *3D Tissue Cytometry*

3D tissue cytometry was performed on image volumes using the VTEA software (Winfree 2017). Segmentation settings were adjusted to yield the best result which was verified visually by sampling random fields within each image stack. Fluorescence from phospho-c-Jun and CD68 was associated with nuclei by 3D morphology and displayed on a scatterplot as individual points, allowing gating of specific cell populations based on fluorescence intensities. Results were reported as percentage of total cells segmented in each large-scale image volume (Makki 2020).

### *CODEX Antibody Conjugation and Validation*

A total of 32 antibodies were used for CODEX and 19 of them were conjugated in-house using a protocol outlined by Akoya Biosciences (Akoya Biosciences, Inc.

CODEX® User Manual, Menlo Park, CA). Conjugation of antibodies to their assigned barcodes, they were first reduced using a “Reduction Master Mix” (Akoya Biosciences, Menlo Park, CA). Lyophilized barcodes were then resuspended using the Molecular Biology Grade Water and Conjugation Solution. The barcode solution was then added to the appropriate reduced antibody and incubated for two hours at room temperature. After incubation, the newly conjugated antibody-barcode was purified in a three-step wash/spin process and stored at 4°C. Successful conjugation was validated via gel electrophoresis as well as immunofluorescent staining and confocal imaging.

### *CODEX Imaging*

Human renal tissue sections of 10 micron were cut from OCT blocks onto poly-L-lysine coated coverslips. Sections were prepared as detailed by the manufacturer’s instructions (Akoya Biosciences, Menlo Park, CA). Tissue retrieval was conducted with a three-step hydration process, followed by a PFA fixation. During fixation, an antibody cocktail of the 32 antibodies listed in Table 5.1 was made and then dispensed onto the coverslip. Tissues were allowed to incubate with the staining solution overnight at 4°C. The following day, the staining solution was washed from the tissues and a multi-step fixation occurred (Schurch 2020).

The imaging of tissues was conducted at 20x resolution using the CODEX system from Akoya Biosciences and a Keyence BZ-X810 slide scanning microscope (Keyence Corporation, Itasca, IL). The resulting images were processed using the CODEX processing software (Akoya Biosciences, Menlo Park, CA) and visualized using FIJI/ImageJ.)

### *Unsupervised analysis, clustering and mapping of cell types*

CODEX images were segmented and analyzed using VTEA version 1.0.3, (Winfree 2022). Cell clusters were identified using unsupervised Ward clustering and dimensionality reduction visualization using t-distributed stochastic neighborhood embedding (t-SNE). The identity of the cell clusters was verified by plotting their mean intensities for specific makers and directly mapping on the image volumes using nuclear overlays.

#### *ELISA and Urine Collection*

Urine samples were collected from patients with a history of CaOx stone formation (non-active stone formers), from CaOx stone patients immediately before undergoing surgery for stone removal (active stone formers) or from non-stone formers as described above. The urine samples were immediately frozen at -80°C. At the time of analysis, samples were thawed and cleared by centrifugation for 5 minutes at 1000xg and assayed for urine MMP7 and MMP9 by ELISA according to manufacturer's instructions (R&D Systems, DMP700/DMP900, Minneapolis, MN). Urine creatinine was used to normalize MMP7 and MMP9 levels between non-active, active, and non-stone formers.

#### *Statistics*

Statistics were used within transcriptomics analyses are described above. Student's t-test was used to compare the phospho-c-JUN and CD68 positive cells between patient samples and reference tissues. Urine levels of MMP7 and MMP9 were compared using ANOVA with the Tukey-Kramer post hoc test.

### *Data Availability*

Raw snRNAseq data generated as part of the KPMP has been accessed from [atlas.kpmp.org](https://atlas.kpmp.org) and from the HuBMAP at [portal.hubmapconsortium.org](https://portal.hubmapconsortium.org). Visium spatial transcriptomic data is available in GEO as GSE206306.

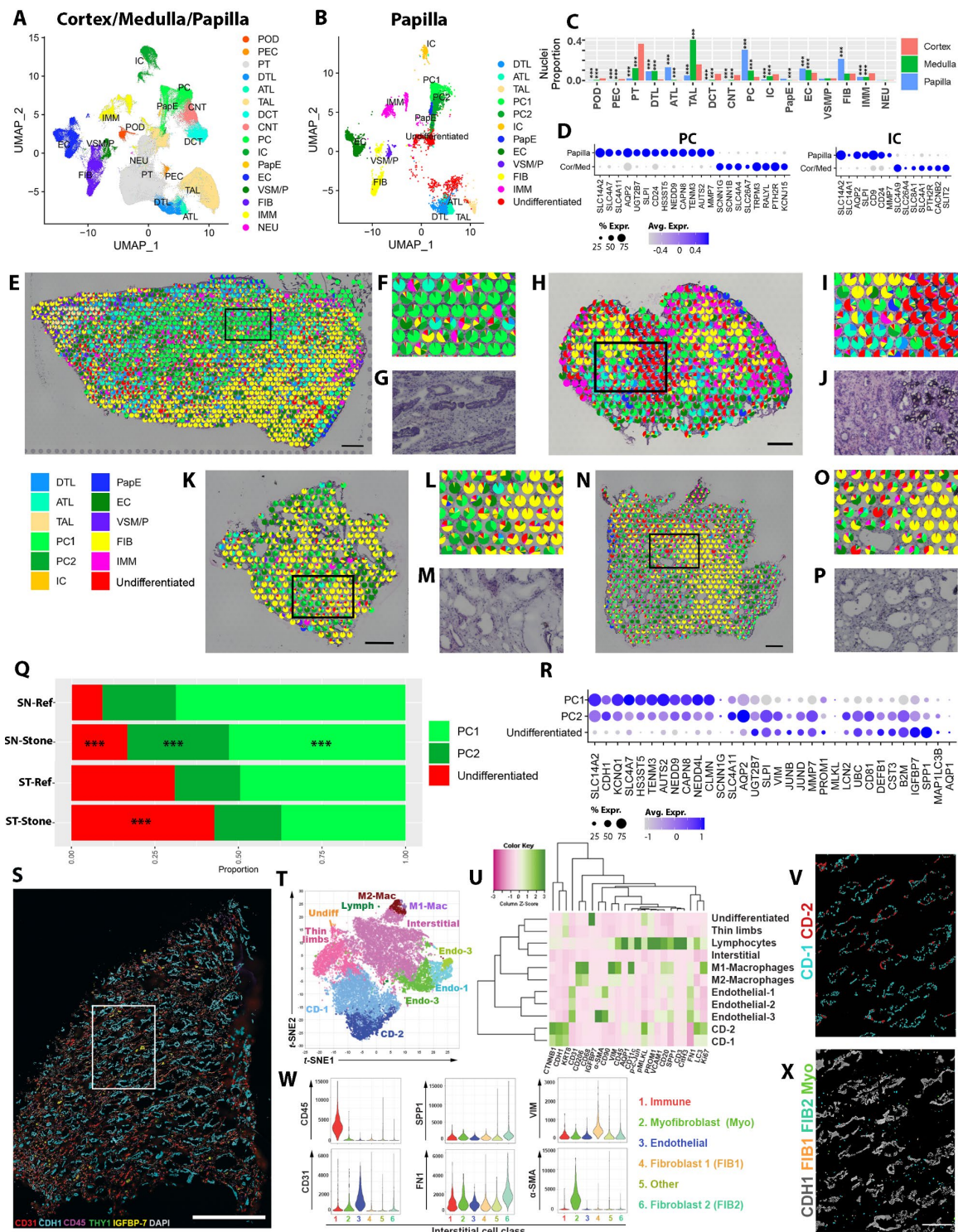


Figure 5.1: Spatially anchored cellular and molecular characterization of the human kidney papilla. A) An integrated snRNA sequencing atlas from the KPMP and HuBMAP consortia presented as a Uniform Manifold Approximation and Projection (Umap) combining nuclei from the renal cortex, medulla and papilla. B) A subset of nuclei specific to the papilla alone. C) The proportion of cell type representation among nuclei in each kidney region. D) Both papillary principal (PC) and intercalated (IC) cells had increased expression of the urate 2 transporter (SLC14A2) and other differentially expressed genes (DEGs) as compared to their counterparts in the renal cortices and medullae. E) Label transfer and mapping of the snRNAseq cell classes onto spatial transcriptomic spots within a reference papilla tissue. F) An enlarged area denoted by the box in (E) showing principal cells mapping on histologically identified collecting ducts in (G). H) Label transfer and mapping of cell classes onto ST spots in a papilla of a stone former. I) An enlarged area from (H) showing the undifferentiated cell signature localizing to areas of mineralization (J). K-P) ST of additional stone papilla specimens showing the signatures of fibroblasts and PC2 (L and M) and undifferentiated cells (O and P). Q) distribution of PC1, PC2 and undifferentiated cells between reference and stone samples across the snRNAseq and ST data. PC2 and undifferentiated cells were relatively more abundant in stone samples. R) Gene expression signatures of PC1, PC2 and undifferentiated cells, showing a spectrum of injury in the PC2 and undifferentiated cell types. S) Co-detection by Indexing (CODEX) multiplex imaging of a reference papilla tissue sample. (Continued on next page)



(Figure 5.1 cont): T) Unsupervised clustering and dimensionality reduction in a t-SNE plot showing various cells classes, which were validated by the level of fluorescence intensity (U) and mapping back on the image. V) localization of CD-1 and CD-2. CD-2 cells express higher levels of injury markers (U) but are not segregated into separate tubules. W) Re-clustering of interstitial cells based on specific markers identifies populations of fibroblasts (2 subtypes, FIB1 and FIB2) and myofibroblasts (Myo), which were mapped into the interstitium around the epithelium (X). \*\*\* denote  $P < 0.01$ . Scale bars: (0.5 mm in E and K, 0.25 mm in H and N, 1 mm in S and 100 microns in X)

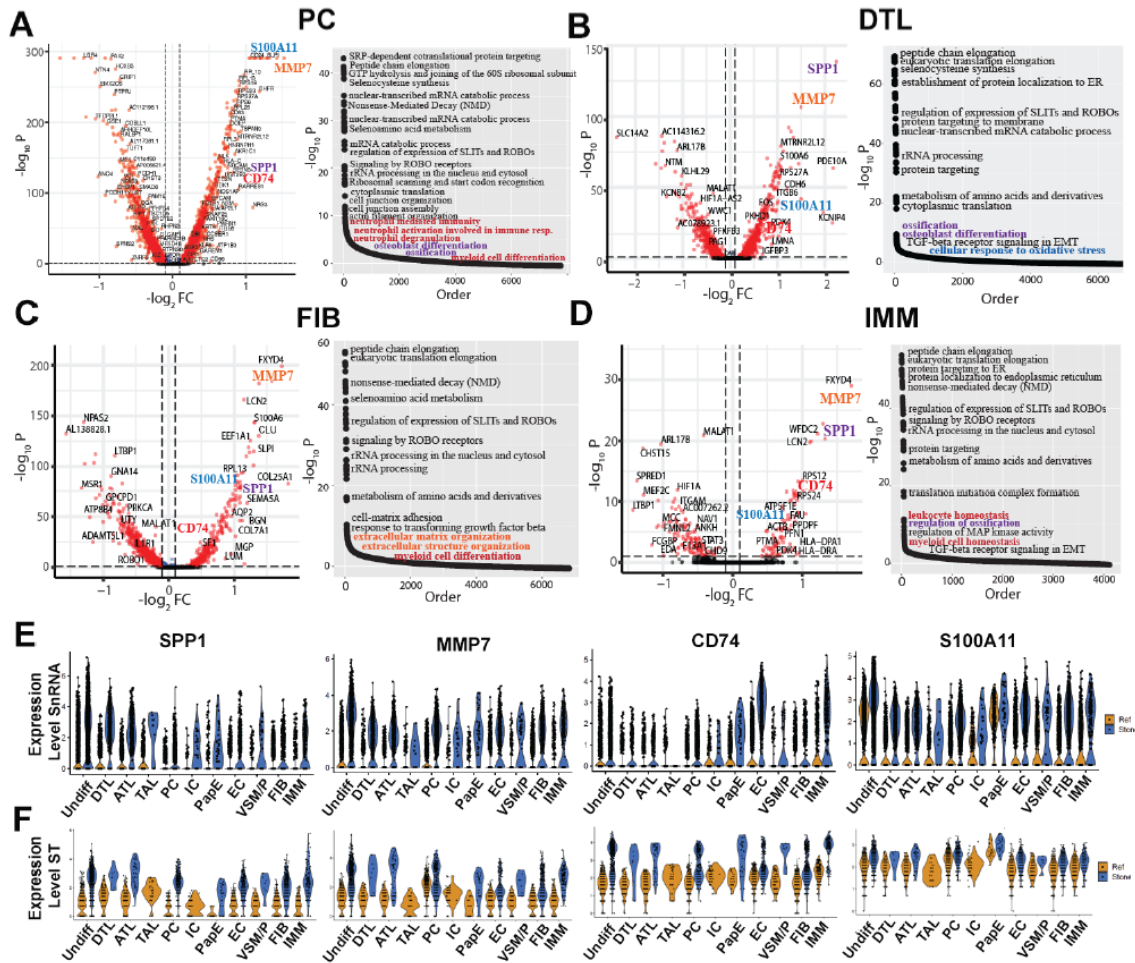


Figure 5.2: Differentially expressed genes (DEGs) induced by stone disease in various cells within the human papilla. A-D) DEGs and enriched pathways in papillary cells by snRNAseq, showing few examples: principal cells (PC), descending thin limbs (DTL), fibroblasts (FIB) and immune cells (IMM). CaOx stone disease induces similar increases in gene expression in various papillary kidney cells. Pathway analysis of snRNA expression detected significant upregulation of ossification (purple text), extracellular matrix organization (orange text), response to oxidative stress (blue text) and leukocyte activation pathways (red text) (Continued on next page)

(Figure 5.2 cont.): E) Violin plots showing differential expression in reference and stone specimens across all papillary cell types of major genes consistently induced by stone disease. F) Expression levels of the genes shown in (E) in the cell signatures mapped on the spatial transcriptomics data in the reference and stone samples.

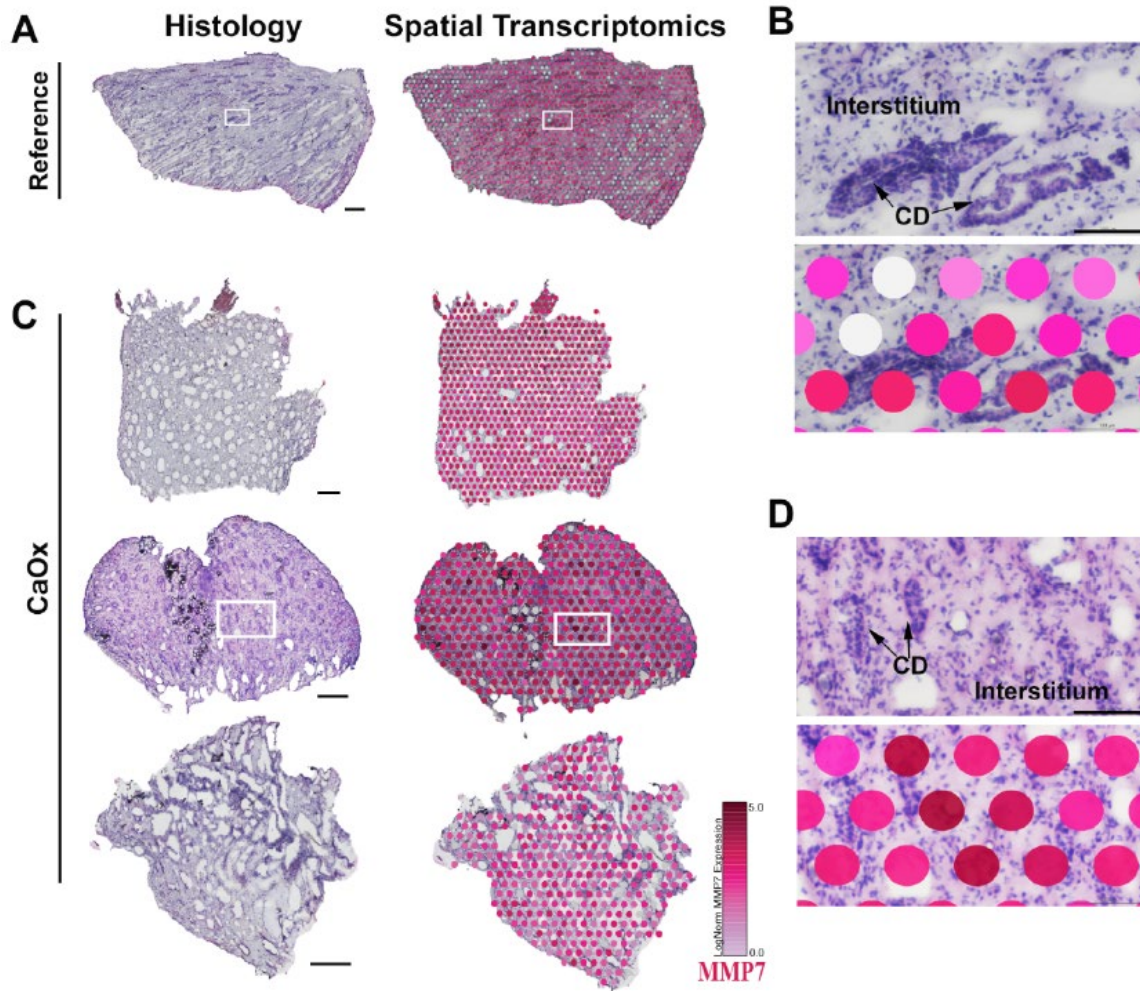


Figure 5.3: MMP7 expression in the papilla. Spatial transcriptomics analysis comparing control (Reference) and three different CaOx stone patient biopsies. In reference tissue, MMP7 expression is localized to collecting ducts. In stone disease, MMP7 expression is diffusely increased and encompasses various papillary cells and structures, which is consistent with the snRNAseq expression and the expression signature mapping on ST shown in Figure 2E and F. Scales bars in (A) and (C): 0.5 mm for reference and top stone sample, 0.25 mm for other 2 specimen; for (B) and (D): 0.1 mm.

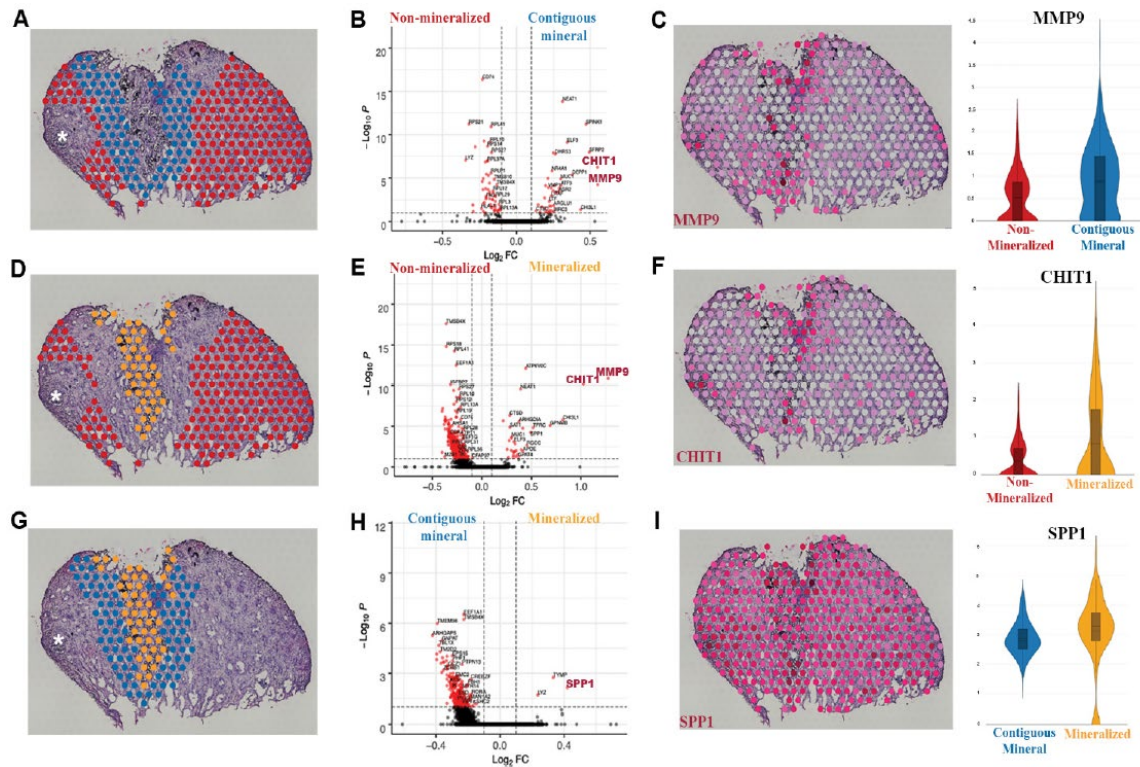


Figure 5.4: Signatures of injury and inflammation are localized to regions of mineralization in the kidney papilla from stone disease. (A) Regions of non-mineralization compared to areas contiguous to mineral display differentially expressed genes (DEGs) associated with pathways leukocyte activation such as MMP9 and CHIT1 (B). MMP9 expression localizes in areas contiguous to mineral and in regions of mineralization (C). Comparisons between areas of non-mineralization and areas of mineralization (D) also display DEGs such as MMP9 and CHIT1 (E). CHIT1 expression also appears to be more robust in areas of mineralization (F). Regional comparison between areas contiguous to mineral and areas of mineralization is shown in (G). SPP1, TYMP and LYZ were differentially expressed in areas of mineralization in this CaOx biopsy specimen (H). (Continued on next page)

(Figure 5.4 cont) SPP1 appears to be localized to regions of mineralization but also displays relatively high expression throughout this stone forming papilla (I). Violin plots show Log-Normalized values. Asterisk in A, D and G denote that the analysis excluded the areas of mineralized plug and was restricted to Randall's plaque.



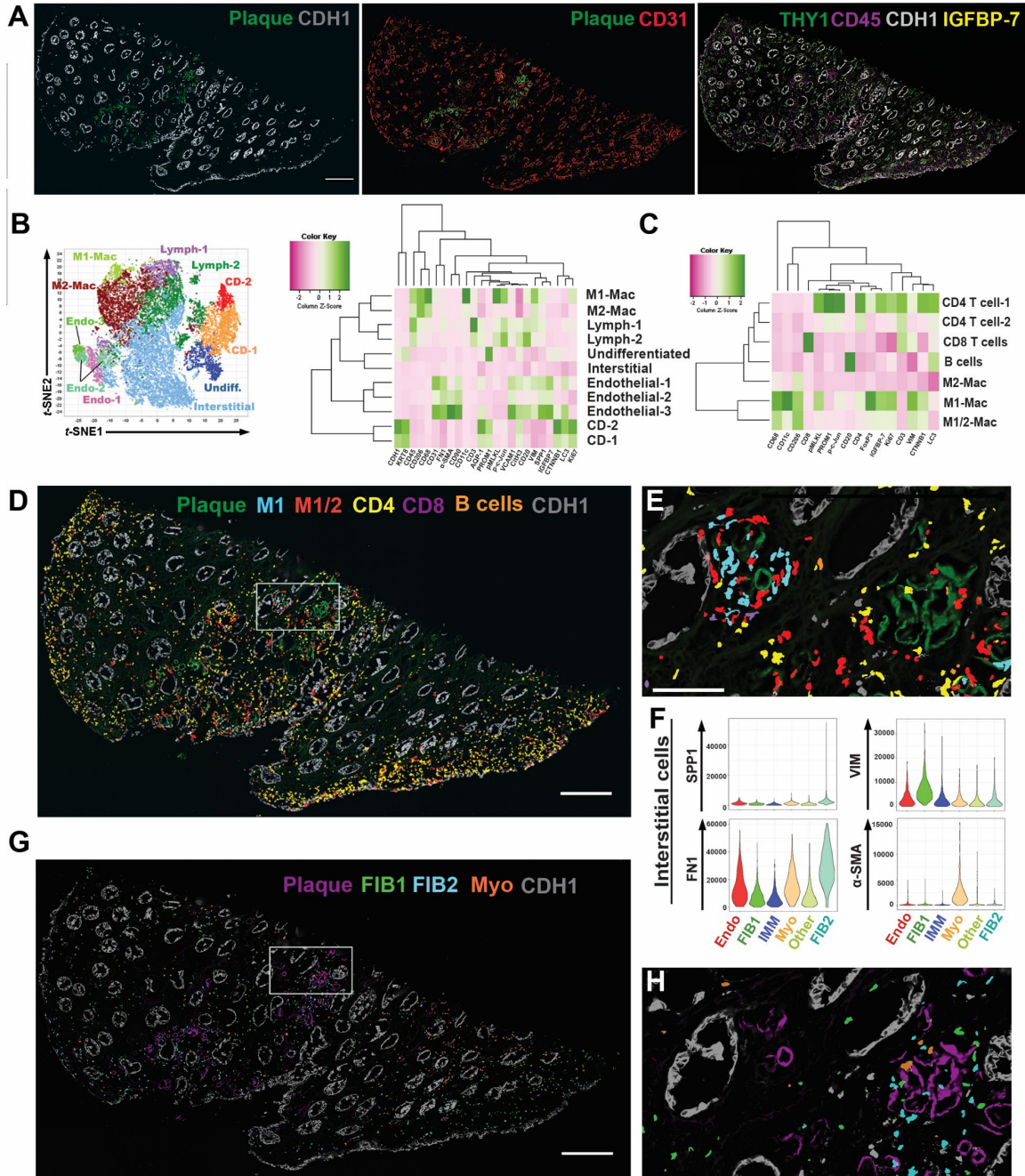


Figure 5.5: CODEX imaging of a papilla with mineral deposition identifies various stages of immune activation and fibrosis around the plaque. (A) CODEX imaging showing a unique autofluorescence of the plaque, which can be easily delineated from the epithelial and vascular cells. (Continued on next page)

(Figure 5.5 cont) B) Unsupervised analysis and clustering identify similar clusters as in the reference specimen (Figure 1), with extensive expansion of the immune clusters. C) Re-clustering and analysis of the immune cells identifies all the major subtypes of leukocytes. Macrophages had an intermediate phenotype between M1 and M2 based on the co-expression of specific markers. D) Mapping of immune cells in the tissue reveals niches of immune activity in certain plaque areas (area of mineral on left in (E), which is a high magnification view of the boxed area in (D) with features of antigen presentation (interaction of antigen presenting macrophages with T and B cells) and a diffuse activated T cells response, particularly towards the papillary endothelium. Interstitial cells F), particularly fibroblasts and myofibroblasts, were abundant throughout the tissue (G), but fibroblasts were concentrated in certain areas of mineral deposition with reduced immune activity (area of mineral on right in (H), which is a high magnification view of the same boxed area in (D) and (G)), suggesting progression from inflammation to fibrosis in neighboring areas within the same tissue. Scales bars: 500 $\mu$ m in (A), (D) and (G); 100 microns for (E).



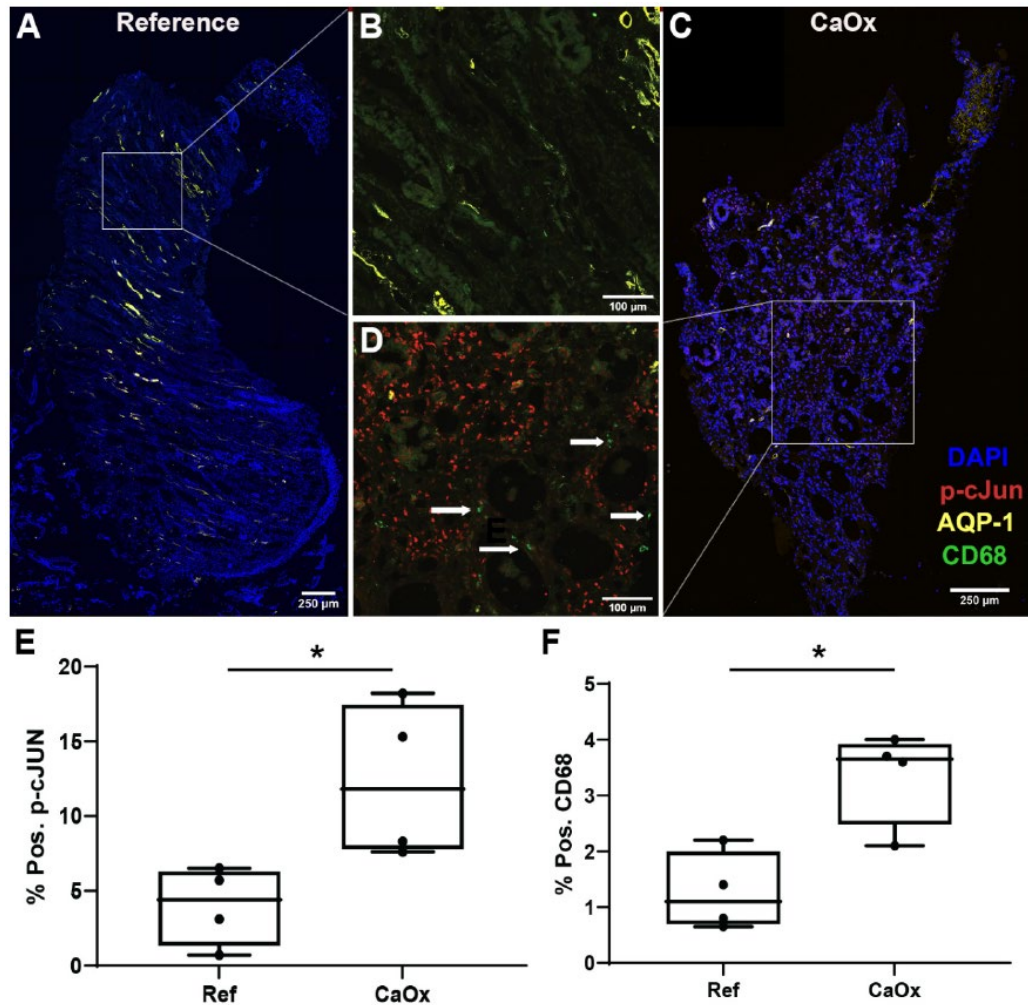


Figure 5.6: Protein markers of oxidative stress (ROS) and macrophage activation are diffusely increased in biopsies of stone patients. (A-D) Representative multi-fluorescence confocal images of kidney papillary biopsies from stone patients and reference nephrectomies tissue specimens (N=4 per group) stained for phospho-c-JUN (p-c-Jun, marker of ROS), CD68 (activated macrophages) and Aquaporin1 (AQP-1, marker for thin descending limbs and descending vasa recta). Images were analyzed using volumetric tissue exploration and analysis (VTEA) software and the resulting outcomes are shown in (E) and (F) for p-c-JUN and CD68 as percentages of total cells in each tissue. Boxed areas in (A) and (C) are enlarged in (B) and (D), respectively.

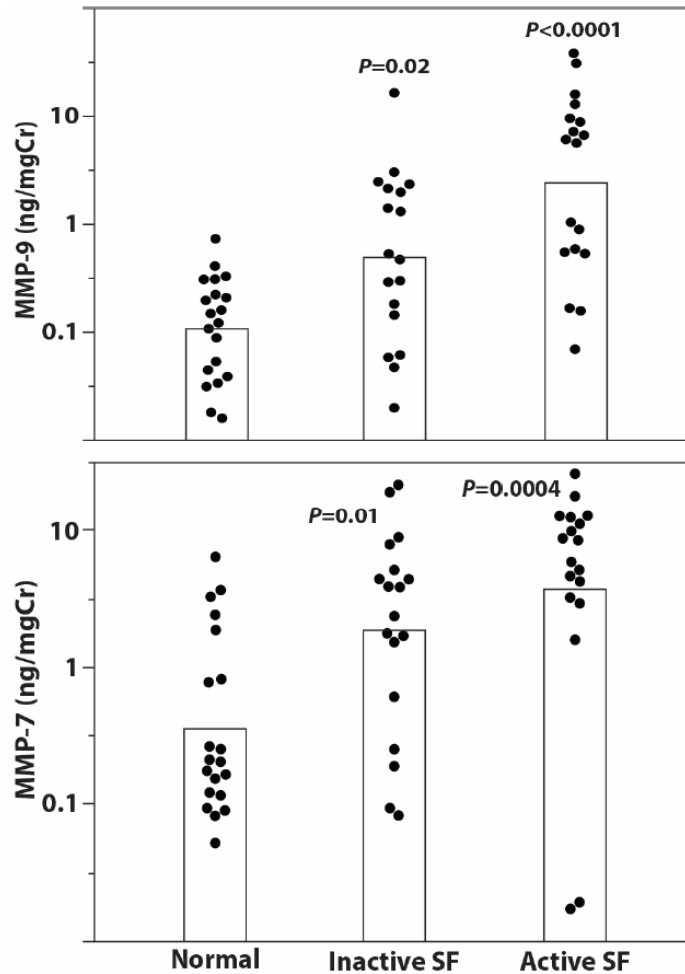


Figure 5.7: MMP7 and MMP9 levels are increased in urine of CaOx stone patients and correlate with disease activity. Urine samples were taken either from CaOx stone patients undergoing surgery for stone removal (active stone formers, SF) or from patients who had previously been stone formers (Inactive SF) or from healthy volunteers. Demographics and relevant clinical variables for each group are presented in Supplemental Table 2. Samples were assayed for urine (A) MMP7, (B) MMP9 and urine creatinine (Cr) by ELISA according to manufacturer's instructions. Samples are plotted as  $\log_{10}(\text{ng MMP/mg Cr})$ .

<b>Antibody</b>	<b>Significance</b>
CD3	Pan T cells
CD4	CD4+ T cells
CD8	CD8+ t cells
CD11c	resident dendritic cells
CD20	B cells
CD45	pan leukocyte markers
CD45RO	memory T cells
HLA-DR	antigen presenter cells
MPO	neutrophils
CD68	macrophages
CD206	M2 macrophages
PROM1 (CD133)	fibrosis
IGFBP7	injury
p- c-Jun	stress kinase pathway
CitruLine H3	netosis
FOXP3	injury
VCAM1	non-reparining epi cells
phosphoMLKL	necroptosis
Fibronectin	Injury, pre-collagen
LC3	autophagy
Ki67	Proliferating cells
CD90	Differentiation
ERG	Endothelial Nuclei
Vimentin	Fibroblasts
OPN	SSP1/osteopontin
AQP1	PT, TDL
E-cadherin	DCT, CD, loop of henle
b-catenin	Tubular epethelium
Cytokeratin8	CNT and CD
Uromodulin	TAL
a-sma	myofibroblast, arterioles
CD31 (PECAM1)	endothelial cells

Table 5.1 - Antibodies used for CODEX multiplexed imaging on human renal papilla

## Chapter 6 - Summary of Work

In this work, we were able to demonstrate numerous avenues of imaging the kidney, from brightfield microscopy to more advanced imaging techniques such as confocal microscopy or highly multiplexed imaging. Along with imaging techniques, we also explored ways of analyzing the resulting images and how to obtain the most information from a single section of a biopsy as we could. Due to limited amounts of renal tissue being available for research purposes, getting as much information as possible from a single biopsy is important, and we showed multiple analytical pathways that allow for robust assessment of a single specimen.

We also explored multiple different disease states throughout the projects described in this work, including diabetic kidney disease (DKD), focal segmental glomerulosclerosis (FSGS), and acute kidney injury (AKI), to highlight a few of the recurring topics. With the numerous imaging and analytical techniques that were utilized in this paper, unique aspects of each disease state were able to be uncovered. When looking at DKD and FSGS samples that were still paraffin embedded with widefield epifluorescence, tubules from the disease specimens had a different average fluorescence intensity compared to the healthy controls, and a similar trend was seen in the average intensity of the glomeruli as well.

We also looked at thick (50 micron) sections from patients with diabetes or healthy reference samples using confocal microscopy and spectral unmixing of eight different probes. VTEA was used to perform supervised classification of the main tubule segments and three immune cell types, as well as f-actin content. The glomeruli were chosen as a focal point again and analyzed for total cell density and immune cell density

as well to assess changes in disease. When looking at the whole tissue, many of the structural markers were less abundant, but the cellular density of the glomeruli increased.

For a more hands-off analytical technique, we introduced machine learning and unsupervised clustering to tissues imaged as described above, as well as brought in highly-multiplexed imaging techniques such as CODEX multiplex imaging. With eight probes combined with unsupervised learning, we were able to identify more cells within each class, catching the lower intensity cells that may have been missed in the supervised analysis. When combining unsupervised learning with CODEX multiplex imaging allowed us to identify more cell types, which uncovered interesting class subtypes such as PROM1+ proximal tubules and immune cell subtypes. We were also able to conduct neighborhood analysis to see what cells interact with one another and form niches within the kidney.

We applied this imaging and analysis technique to mouse samples as well and expanded the CODEX antibody panels in the human cortex and papilla. In the mouse specimens, we studied the immune response to ischemia reperfusion injury and THP deficiency. Multiple changes in macrophage abundance and distribution were seen in response to both injury and THP deficiency. There are more studies that need to occur to fully characterize these macrophages, as well as the other immune cells that changes were noted in, such as neutrophils and T cells. For the human CODEX experiments, the cortical studies expanded on the PROM1+ populations seen in the preliminary studies, as well as uncovered a CD90+ proximal tubule population and an increase in a possible stromal cell population in disease specimens. The studies conducted on the human papilla were combined with single nuclear RNA sequencing and spatial transcriptomics in order

to combine nuclear-based data with protein-based data. A unique fibroblast population that was seen in association with Randall's plaque was uncovered in this study, as well as subtypes of collecting duct cells and an undifferentiated cell type.

All of these experiments combined, both human and mouse, provided a unique look into the cellular heterogeneity of the kidney, and how that heterogeneity changes with disease. We not only surveyed numerous disease states throughout the works described, but we also analyzed these disease states in multiple ways in order to fully characterize the samples. By using state of the art techniques and pioneering new analytical pipelines, we were able generate an atlas of all regions of the kidney and identified all major components of each region, as well as the immune and injury components that many studies may miss.

## References

1. Abbas, A., Aukrust, P., Russell, D., Krohg-Sørensen, K., Almås, T., Bundgaard, D., Bjerkeli, V., Sagen, E. L., Michelsen, A. E., Dahl, T. B., Holm, S., Ueland, T., Skjelland, M., & Halvorsen, B. (2014). Matrix Metalloproteinase 7 Is Associated with Symptomatic Lesions and Adverse Events in Patients with Carotid Atherosclerosis. *PLOS ONE*, 9(1), e84935. <https://doi.org/10.1371/journal.pone.0084935>
2. Agasti, S. S., Wang, Y., Schueder, F., Sukumar, A., Jungmann, R., & Yin, P. (2017). DNA-barcoded labeling probes for highly multiplexed Exchange-PAINT imaging [10.1039/C6SC05420J]. *Chemical Science*, 8(4), 3080-3091. <https://doi.org/10.1039/C6SC05420J>
3. Alex B. Renjin. Published online 2013. <https://github.com/bedatadriven/renjin/>
4. Anders, H. J., & Ryu, M. (2011, Nov). Renal microenvironments and macrophage phenotypes determine progression or resolution of renal inflammation and fibrosis. *Kidney Int*, 80(9), 915-925. <https://doi.org/10.1038/ki.2011.217>
5. Angelo, M., Bendall, S. C., Finck, R., Hale, M. B., Hitzman, C., Borowsky, A. D., Levenson, R. M., Lowe, J. B., Liu, S. D., Zhao, S., Natkunam, Y., & Nolan, G. P. (2014, Apr). Multiplexed ion beam imaging of human breast tumors. *Nat Med*, 20(4), 436-442. <https://doi.org/10.1038/nm.3488>
6. Ashkar T, Ferkowicz M. Sample preparation and imaging for large scale 3D spectral confocal imaging of tissues v1. doi:10.17504/protocols.io.9avh2e6

7. Balzer, M. S., Rohacs, T., & Susztak, K. (2022, Feb 10). How Many Cell Types Are in the Kidney and What Do They Do? *Annu Rev Physiol*, 84, 507-531.  
<https://doi.org/10.1146/annurev-physiol-052521-121841>
8. Barkas, Nikolas, Viktor Petukhov, Peter V. Kharchenko, and Evan Biederstedt. 2021. 'pagoda2: Single Cell Analysis and Differential Expression. R package version 1.0.8.'
9. Barwinska, D., El-Achkar, T. M., Melo Ferreira, R., Syed, F., Cheng, Y. H., Winfree, S., Ferkowicz, M. J., Hato, T., Collins, K. S., Dunn, K. W., Kelly, K. J., Sutton, T. A., Rovin, B. H., Parikh, S. V., Phillips, C. L., Dagher, P. C., & Eadon, M. T. (2021, Feb). Molecular characterization of the human kidney interstitium in health and disease. *Sci Adv*, 7(7). <https://doi.org/10.1126/sciadv.abd3359>
10. Bhuiyan, S., Shen, M., Chelvaretnam, S., Tan, A. Y., Ho, G., Hossain, M. A., Widdop, R. E., & Samuel, C. S. (2021). Assessment of renal fibrosis and anti-fibrotic agents using a novel diagnostic and stain-free second-harmonic generation platform. *The FASEB Journal*, 35(5), e21595.  
<https://doi.org/https://doi.org/10.1096/fj.202002053RRR>
11. Bird, V. Y., & Khan, S. R. (2017, Jan). How do stones form? Is unification of theories on stone formation possible? *Arch Esp Urol*, 70(1), 12-27.
12. Black, L. M., Farrell, E. R., Barwinska, D., Osis, G., Zmijewska, A. A., Traylor, A. M., Esman, S. K., Bolisetty, S., Whipple, G., Kamocka, M. M., Winfree, S., Spangler, D. R., Khan, S., Zarjou, A., El-Achkar, T. M., & Agarwal, A. (2021, Dec 1). VEGFR3 tyrosine kinase inhibition aggravates cisplatin nephrotoxicity. *Am J Physiol Renal Physiol*, 321(6), F675-f688. <https://doi.org/10.1152/ajprenal.00186.2021>



13. Black, L. M., Winfree, S., Khochare, S. D., Kamocka, M. M., Traylor, A. M., Esman, S. K., Khan, S., Zarjou, A., Agarwal, A., & El-Achkar, T. M. (2021, Sep). Quantitative 3-dimensional imaging and tissue cytometry reveals lymphatic expansion in acute kidney injury. *Lab Invest*, 101(9), 1186-1196.  
<https://doi.org/10.1038/s41374-021-00609-2>
14. Bonsib, S. M., & Reznicek, M. J. (1990, Mar). Renal biopsy frozen section: a fluorescent study of hematoxylin and eosin-stained sections. *Mod Pathol*, 3(2), 204-210.
15. Börner, K., Teichmann, S. A., Quardokus, E. M., Gee, J. C., Browne, K., Osumi-Sutherland, D., Herr, B. W., Bueckle, A., Paul, H., Haniffa, M., Jardine, L., Bernard, A., Ding, S.-L., Miller, J. A., Lin, S., Halushka, M. K., Boppana, A., Longacre, T. A., Hickey, J., Lin, Y., Valerius, M. T., He, Y., Pryhuber, G., Sun, X., Jorgensen, M., Radtke, A. J., Wasserfall, C., Ginty, F., Ho, J., Sunshine, J., Beuschel, R. T., Brusko, M., Lee, S., Malhotra, R., Jain, S., & Weber, G. (2021, 2021/11/01). Anatomical structures, cell types and biomarkers of the Human Reference Atlas. *Nature Cell Biology*, 23(11), 1117-1128. <https://doi.org/10.1038/s41556-021-00788-6>
16. Boudierlique, E., Tang, E., Perez, J., Coudert, A., Bazin, D., Verpont, M. C., Duranton, C., Rubera, I., Haymann, J. P., Leftheriotis, G., Martin, L., Daudon, M., & Letavernier, E. (2019, Nov). Vitamin D and Calcium Supplementation Accelerates Randall's Plaque Formation in a Murine Model. *Am J Pathol*, 189(11), 2171-2180.  
<https://doi.org/10.1016/j.ajpath.2019.07.013>

17. Bülow, R. D., & Boor, P. (2019, Sep). Extracellular Matrix in Kidney Fibrosis: More Than Just a Scaffold. *J Histochem Cytochem*, 67(9), 643-661.  
<https://doi.org/10.1369/0022155419849388>
18. Burke, B. (2004). The role of matrix metalloproteinase 7 in innate immunity. *Immunobiology*, 209(1-2), 51-56. <https://doi.org/10.1016/j.imbio.2004.04.005>
19. Canales, B. K., Anderson L Fau - Higgins, L., Higgins L Fau - Ensrud-Bowlin, K., Ensrud-Bowlin K Fau - Roberts, K. P., Roberts Kp Fau - Wu, B., Wu B Fau - Kim, I. W., Kim Iw Fau - Monga, M., & Monga, M. Proteome of human calcium kidney stones. (1527-9995 (Electronic)).
20. Canela, V. H., Bledsoe, S. B., Worcester, E. M., Lingeman, J. E., El-Achkar, T. M., & Williams, J. C., Jr. (2022, Jul). Collagen fibrils and cell nuclei are entrapped within Randall's plaques but not in CaOx matrix overgrowth: A microscopic inquiry into Randall's plaque stone pathogenesis. *Anat Rec (Hoboken)*, 305(7), 1701-1711.  
<https://doi.org/10.1002/ar.24837>
21. Canela, V. H., Bowen, W. S., Ferreira, R. M., Lingeman, J. E., Sabo, A. R., Barwinska, D., Winfree, S., Lake, B., Cheng, Y.-H., LaFavers, K. A., Zhang, K., Coe, F. L., Worcester, E., Jain, S., Eadon, M. T., Williams, J. C., & El-Achkar, T. M. (2022). A spatially anchored transcriptomic atlas of the human kidney papilla identifies significant immune injury and matrix remodeling in patients with stone disease. *bioRxiv*, 2022.2006.2022.497218.  
<https://doi.org/10.1101/2022.06.22.497218>

22. Carney, E. F. (2020). The Impact of Chronic Kidney Disease on Global Health. *Nature Reviews*, 16.
23. Chen, L., Chou, C. L., & Knepper, M. A. (2021, Mar 4). A Comprehensive Map of mRNAs and Their Isoforms across All 14 Renal Tubule Segments of Mouse. *J Am Soc Nephrol*, 32(4), 897-912. <https://doi.org/10.1681/asn.2020101406>
24. Chen, X., Nadiarynkh, O., Plotnikov, S., & Campagnola, P. J. (2012, 2012/04/01). Second harmonic generation microscopy for quantitative analysis of collagen fibrillar structure. *Nature Protocols*, 7(4), 654-669. <https://doi.org/10.1038/nprot.2012.009>
25. Chessa, F., Mathow, D., Wang, S., Hielscher, T., Atzberger, A., Porubsky, S., Gretz, N., Burgdorf, S., Gröne, H. J., & Popovic, Z. V. (2016, Jan). The renal microenvironment modifies dendritic cell phenotype. *Kidney Int*, 89(1), 82-94. <https://doi.org/10.1038/ki.2015.292>
26. Consortium, H. (2019, Oct). The human body at cellular resolution: the NIH Human Biomolecular Atlas Program. *Nature*, 574(7777), 187-192. <https://doi.org/10.1038/s41586-019-1629-x>
27. Coutu, D. L., Kokkaliaris, K. D., Kunz, L., & Schroeder, T. (2017, Dec). Three-dimensional map of nonhematopoietic bone and bone-marrow cells and molecules. *Nat Biotechnol*, 35(12), 1202-1210. <https://doi.org/10.1038/nbt.4006>
28. Coutu, D. L., Kokkaliaris, K. D., Kunz, L., & Schroeder, T. (2018, Jan). Multicolor quantitative confocal imaging cytometry. *Nat Methods*, 15(1), 39-46. <https://doi.org/10.1038/nmeth.4503>

29. Croce, A. C., & Bottioli, G. (2014, Dec 12). Autofluorescence spectroscopy and imaging: a tool for biomedical research and diagnosis. *Eur J Histochem*, 58(4), 2461. <https://doi.org/10.4081/ejh.2014.2461>
30. Croce, A. C., De Simone, U., Freitas, I., Boncompagni, E., Neri, D., Cillo, U., & Bottioli, G. (2010, Jul). Human liver autofluorescence: an intrinsic tissue parameter discriminating normal and diseased conditions. *Lasers Surg Med*, 42(5), 371-378. <https://doi.org/10.1002/lsm.20923>
31. Croce, A. C., Ferrigno, A., Bottioli, G., & Vairetti, M. (2018, Jul). Autofluorescence-based optical biopsy: An effective diagnostic tool in hepatology. *Liver Int*, 38(7), 1160-1174. <https://doi.org/10.1111/liv.13753>
32. Cui, N., Hu, M., & Khalil, R. A. (2017). Biochemical and Biological Attributes of Matrix Metalloproteinases. *Prog Mol Biol Transl Sci*, 147, 1-73. <https://doi.org/10.1016/bs.pmbts.2017.02.005>
33. Daudon, M., Bazin, D., & Letavernier, E. (2015, Jan). Randall's plaque as the origin of calcium oxalate kidney stones. *Urolithiasis*, 43 Suppl 1, 5-11. <https://doi.org/10.1007/s00240-014-0703-y>
34. de Boer, I. H., Alpers, C. E., Azeloglu, E. U., Balis, U. G. J., Barasch, J. M., Barisoni, L., Blank, K. N., Bomback, A. S., Brown, K., Dagher, P. C., Dighe, A. L., Eadon, M. T., El-Achkar, T. M., Gaut, J. P., Hacohen, N., He, Y., Hodgins, J. B., Jain, S., Kellum, J. A., Kiryluk, K., Knight, R., Laszik, Z. G., Lienczewski, C., Mariani, L. H., McClelland, R. L., Menez, S., Moledina, D. G., Mooney, S. D., O'Toole, J. F., Palevsky, P. M., Parikh, C. R., Poggio, E. D., Rosas, S. E., Rosengart, M. R., Sarwal, M. M., Schaub, J. A., Sedor, J. R., Sharma, K., Steck, B., Toto, R. D., Troyanskaya,

- O. G., Tuttle, K. R., Vazquez, M. A., Waikar, S. S., Williams, K., Wilson, F. P., Zhang, K., Iyengar, R., Kretzler, M., & Himmelfarb, J. (2021, Mar). Rationale and design of the Kidney Precision Medicine Project. *Kidney Int*, 99(3), 498-510.  
<https://doi.org/10.1016/j.kint.2020.08.039>
35. de Water, R., Noordermeer, C., van der Kwast, T. H., Nizze, H., Boevé, E. R., Kok, D. J., & Schröder, F. H. (1999, Apr). Calcium oxalate nephrolithiasis: effect of renal crystal deposition on the cellular composition of the renal interstitium. *Am J Kidney Dis*, 33(4), 761-771. [https://doi.org/10.1016/s0272-6386\(99\)70231-3](https://doi.org/10.1016/s0272-6386(99)70231-3)
36. Dong, C. Y., & Campagnola, P. J. (2010, Nov). Optical diagnostics of tissue pathology by multiphoton microscopy. *Expert Opin Med Diagn*, 4(6), 519-529.  
<https://doi.org/10.1517/17530059.2010.525634>
37. Eadon, M. T., Schwantes-An, T. H., Phillips, C. L., Roberts, A. R., Greene, C. V., Hallab, A., Hart, K. J., Lipp, S. N., Perez-Ledezma, C., Omar, K. O., Kelly, K. J., Moe, S. M., Dagher, P. C., El-Achkar, T. M., & Moorthi, R. N. (2020, Sep). Kidney Histopathology and Prediction of Kidney Failure: A Retrospective Cohort Study. *Am J Kidney Dis*, 76(3), 350-360. <https://doi.org/10.1053/j.ajkd.2019.12.014>
38. El-Achkar, T. M., Eadon, M. T., Menon, R., Lake, B. B., Sigdel, T. K., Alexandrov, T., Parikh, S., Zhang, G., Dobi, D., Dunn, K. W., Otto, E. A., Anderton, C. R., Carson, J. M., Luo, J., Park, C., Hamidi, H., Zhou, J., Hoover, P., Schroeder, A., Joanes, M., Azeloglu, E. U., Sealfon, R., Winfree, S., Steck, B., He, Y., D'Agati, V., Iyengar, R., Troyanskaya, O. G., Barisoni, L., Gaut, J., Zhang, K., Laszik, Z., Rovin, B. H., Dagher, P. C., Sharma, K., Sarwal, M. M., Hodgins, J. B., Alpers, C. E., Kretzler, M., & Jain, S. (2021, Jan 1). A multimodal and integrated approach to

interrogate human kidney biopsies with rigor and reproducibility: guidelines from the Kidney Precision Medicine Project. *Physiol Genomics*, 53(1), 1-11.

<https://doi.org/10.1152/physiolgenomics.00104.2020>

39. El-Achkar, T. M., Plotkin, Z., Marcic, B., & Dagher, P. C. (2007, Oct). Sepsis induces an increase in thick ascending limb Cox-2 that is TLR4 dependent. *Am J Physiol Renal Physiol*, 293(4), F1187-1196.  
<https://doi.org/10.1152/ajprenal.00217.2007>
40. Elkington, P. T., Green, J. A., & Friedland, J. S. (2009). Analysis of matrix metalloproteinase secretion by macrophages. *Methods Mol Biol*, 531, 253-265.  
[https://doi.org/10.1007/978-1-59745-396-7\\_16](https://doi.org/10.1007/978-1-59745-396-7_16)
41. Evan, A., Lingeman, J., Coe, F. L., & Worcester, E. (2006, Apr). Randall's plaque: pathogenesis and role in calcium oxalate nephrolithiasis. *Kidney Int*, 69(8), 1313-1318. <https://doi.org/10.1038/sj.ki.5000238>
42. Evan, A. P., Coe, F. L., Lingeman, J., Bledsoe, S., & Worcester, E. M. (2018, Nov 1). Randall's plaque in stone formers originates in ascending thin limbs. *Am J Physiol Renal Physiol*, 315(5), F1236-f1242. <https://doi.org/10.1152/ajprenal.00035.2018>
43. Evan, A. P., Lingeman, J. E., Coe, F. L., Parks, J. H., Bledsoe, S. B., Shao, Y., Sommer, A. J., Paterson, R. F., Kuo, R. L., & Grynpas, M. (2003, Mar). Randall's plaque of patients with nephrolithiasis begins in basement membranes of thin loops of Henle. *J Clin Invest*, 111(5), 607-616. <https://doi.org/10.1172/jci17038>
44. Evan, A. P., Lingeman, J. E., Worcester, E. M., Sommer, A. J., Phillips, C. L., Williams, J. C., & Coe, F. L. (2014, Apr). Contrasting histopathology and crystal deposits in kidneys of idiopathic stone formers who produce hydroxy apatite,

brushite, or calcium oxalate stones. *Anat Rec (Hoboken)*, 297(4), 731-748.

<https://doi.org/10.1002/ar.22881>

45. Evan, A. P., Worcester, E. M., Williams JR., J. C., Sommer, A. J., Lingeman, J. E., Phillips, C. L., & Coe, F. L. (2015). Biopsy Proven Medullary Sponge Kidney: Clinical Findings, Histopathology, and Role of Osteogenesis in Stone and Plaque Formation. *The Anatomical Record*, 298(5), 865-877.  
<https://doi.org/https://doi.org/10.1002/ar.23105>
46. Fenton, R. A., Flynn, A., Shodeinde, A., Smith, C. P., Schnermann, J., & Knepper, M. A. (2005, Jun). Renal phenotype of UT-A urea transporter knockout mice. *J Am Soc Nephrol*, 16(6), 1583-1592. <https://doi.org/10.1681/asn.2005010031>
47. Ferkowicz, M. J., Winfree, S., Sabo, A. R., Kamocka, M. M., Khochare, S., Barwinska, D., Eadon, M. T., Cheng, Y. H., Phillips, C. L., Sutton, T. A., Kelly, K. J., Dagher, P. C., El-Achkar, T. M., & Dunn, K. W. (2021, May). Large-scale, three-dimensional tissue cytometry of the human kidney: a complete and accessible pipeline. *Lab Invest*, 101(5), 661-676. <https://doi.org/10.1038/s41374-020-00518-w>
48. Fonseca, D. M., Hand, T. W., Han, S. J., Gerner, M. Y., Glatman Zaretsky, A., Byrd, A. L., Harrison, O. J., Ortiz, A. M., Quinones, M., Trinchieri, G., Brenchley, J. M., Brodsky, I. E., Germain, R. N., Randolph, G. J., & Belkaid, Y. (2015, Oct 8). Microbiota-Dependent Sequelae of Acute Infection Compromise Tissue-Specific Immunity. *Cell*, 163(2), 354-366. <https://doi.org/10.1016/j.cell.2015.08.030>
49. Fu, H., Zhou, D., Zhu, H., Liao, J., Lin, L., Hong, X., Hou, F. F., & Liu, Y. (2019, May). Matrix metalloproteinase-7 protects against acute kidney injury by priming

renal tubules for survival and regeneration. *Kidney Int*, 95(5), 1167-1180.

<https://doi.org/10.1016/j.kint.2018.11.043>

50. Gao, C., Chen, L., Chen, E., Tsilosani, A., Xia, Y., & Zhang, W. (2021, Oct 19).

Generation of Distal Renal Segments Involves a Unique Population of Aqp2(+) Progenitor Cells. *J Am Soc Nephrol*, 32(12), 3035-3049.

<https://doi.org/10.1681/asn.2021030399>

51. Garcia-Fernandez, N., Jacobs-Cachá, C., Mora-Gutiérrez, J. M., Vergara, A., Orbe, J., & Soler, M. J. (2020, Feb 8). Matrix Metalloproteinases in Diabetic Kidney Disease.

*J Clin Med*, 9(2). <https://doi.org/10.3390/jcm9020472>

52. Gayoso, Adam, Jonathan Shor, and Ambrose J. ; Sharma Carr, Roshan; Pe'er, Dana

2020. 'JonathanShor/DoubletDetection: doubletdetection v3.0'.

53. Gerdes, M. J., Sevinsky, C. J., Sood, A., Adak, S., Bello, M. O., Bordwell, A., Can,

A., Corwin, A., Dinn, S., Filkins, R. J., Hollman, D., Kamath, V., Kaanumalle, S.,

Kenny, K., Larsen, M., Lazare, M., Li, Q., Lowes, C., McCulloch, C. C.,

McDonough, E., Montalto, M. C., Pang, Z., Rittscher, J., Santamaria-Pang, A.,

Sarachan, B. D., Seel, M. L., Seppo, A., Shaikh, K., Sui, Y., Zhang, J., & Ginty, F.

(2013, Jul 16). Highly multiplexed single-cell analysis of formalin-fixed, paraffin-

embedded cancer tissue. *Proc Natl Acad Sci U S A*, 110(29), 11982-11987.

<https://doi.org/10.1073/pnas.1300136110>

54. Gerhardt, L. M. S., Liu, J., Koppitch, K., Cippà, P. E., & McMahon, A. P. (2021, Jul

6). Single-nuclear transcriptomics reveals diversity of proximal tubule cell states in a

dynamic response to acute kidney injury. *Proc Natl Acad Sci U S A*, 118(27).

<https://doi.org/10.1073/pnas.2026684118>



55. Gerner, M. Y., Kastenmuller, W., Ifrim, I., Kabat, J., & Germain, R. N. (2012, Aug 24). Histo-cytometry: a method for highly multiplex quantitative tissue imaging analysis applied to dendritic cell subset microanatomy in lymph nodes. *Immunity*, 37(2), 364-376. <https://doi.org/10.1016/j.immuni.2012.07.011>
56. Gerner, M. Y., Torabi-Parizi, P., & Germain, R. N. (2015, Jan 20). Strategically localized dendritic cells promote rapid T cell responses to lymph-borne particulate antigens. *Immunity*, 42(1), 172-185. <https://doi.org/10.1016/j.immuni.2014.12.024>
57. Giesen, C., Wang, H. A., Schapiro, D., Zivanovic, N., Jacobs, A., Hattendorf, B., Schüffler, P. J., Grolimund, D., Buhmann, J. M., Brandt, S., Varga, Z., Wild, P. J., Günther, D., & Bodenmiller, B. (2014, Apr). Highly multiplexed imaging of tumor tissues with subcellular resolution by mass cytometry. *Nat Methods*, 11(4), 417-422. <https://doi.org/10.1038/nmeth.2869>
58. Glaser, A. K., Reder, N. P., Chen, Y., Yin, C., Wei, L., Kang, S., Barner, L. A., Xie, W., McCarty, E. F., Mao, C., Halpern, A. R., Stoltzfus, C. R., Daniels, J. S., Gerner, M. Y., Nicovich, P. R., Vaughan, J. C., True, L. D., & Liu, J. T. C. (2019, 2019/07/04). Multi-immersion open-top light-sheet microscope for high-throughput imaging of cleared tissues. *Nature Communications*, 10(1), 2781. <https://doi.org/10.1038/s41467-019-10534-0>
59. Goltsev, Y., Samusik, N., Kennedy-Darling, J., Bhate, S., Hale, M., Vazquez, G., Black, S., & Nolan, G. P. (2018, Aug 9). Deep Profiling of Mouse Splenic Architecture with CODEX Multiplexed Imaging. *Cell*, 174(4), 968-981.e915. <https://doi.org/10.1016/j.cell.2018.07.010>

60. Halse, H., Colebatch, A. J., Petrone, P., Henderson, M. A., Mills, J. K., Snow, H., Westwood, J. A., Sandhu, S., Raleigh, J. M., Behren, A., Cebon, J., Darcy, P. K., Kershaw, M. H., McArthur, G. A., Gyorki, D. E., & Neeson, P. J. (2018, Jul 24). Multiplex immunohistochemistry accurately defines the immune context of metastatic melanoma. *Sci Rep*, 8(1), 11158. <https://doi.org/10.1038/s41598-018-28944-3>
61. Hanania, R., Sun, H. S., Xu, K., Pustynnik, S., Jeganathan, S., & Harrison, R. E. (2012, Mar 9). Classically activated macrophages use stable microtubules for matrix metalloproteinase-9 (MMP-9) secretion. *J Biol Chem*, 287(11), 8468-8483. <https://doi.org/10.1074/jbc.M111.290676>
62. Hato, T., Winfree, S., Day, R., Sandoval, R. M., Molitoris, B. A., Yoder, M. C., Wiggins, R. C., Zheng, Y., Dunn, K. W., & Dagher, P. C. (2017, Aug). Two-Photon Intravital Fluorescence Lifetime Imaging of the Kidney Reveals Cell-Type Specific Metabolic Signatures. *J Am Soc Nephrol*, 28(8), 2420-2430. <https://doi.org/10.1681/asn.2016101153>
63. Hickey, J. W., Tan, Y., Nolan, G. P., & Goltsev, Y. (2021). Strategies for Accurate Cell Type Identification in CODEX Multiplexed Imaging Data. *Front Immunol*, 12, 727626. <https://doi.org/10.3389/fimmu.2021.727626>
64. Hillert, R., Gieseler, A., Krusche, A., Humme, D., Röwert-Huber, H. J., Sterry, W., Walden, P., & Schubert, W. (2016, Jan 13). Large molecular systems landscape uncovers T cell trapping in human skin cancer. *Sci Rep*, 6, 19012. <https://doi.org/10.1038/srep19012>

65. Howles, S. A., & Thakker, R. V. (2020, Jul). Genetics of kidney stone disease. *Nat Rev Urol*, 17(7), 407-421. <https://doi.org/10.1038/s41585-020-0332-x>
66. Im, S. J., Hashimoto, M., Gerner, M. Y., Lee, J., Kissick, H. T., Burger, M. C., Shan, Q., Hale, J. S., Lee, J., Nasti, T. H., Sharpe, A. H., Freeman, G. J., Germain, R. N., Nakaya, H. I., Xue, H. H., & Ahmed, R. (2016, Sep 15). Defining CD8<sup>+</sup> T cells that provide the proliferative burst after PD-1 therapy. *Nature*, 537(7620), 417-421. <https://doi.org/10.1038/nature19330>
67. Jackson, H. W., Fischer, J. R., Zanutelli, V. R. T., Ali, H. R., Mechera, R., Soysal, S. D., Moch, H., Muenst, S., Varga, Z., Weber, W. P., & Bodenmiller, B. (2020, Feb). The single-cell pathology landscape of breast cancer. *Nature*, 578(7796), 615-620. <https://doi.org/10.1038/s41586-019-1876-x>
68. Jager, N. A., Wallis de Vries, B. M., Hillebrands, J. L., Harlaar, N. J., Tio, R. A., Slart, R. H., van Dam, G. M., Boersma, H. H., Zeebregts, C. J., & Westra, J. (2016, Apr). Distribution of Matrix Metalloproteinases in Human Atherosclerotic Carotid Plaques and Their Production by Smooth Muscle Cells and Macrophage Subsets. *Mol Imaging Biol*, 18(2), 283-291. <https://doi.org/10.1007/s11307-015-0882-0>
69. Jain, M., Robinson, B. D., Scherr, D. S., Sterling, J., Lee, M. M., Wysock, J., Rubin, M. A., Maxfield, F. R., Zipfel, W. R., Webb, W. W., & Mukherjee, S. (2012, May). Multiphoton microscopy in the evaluation of human bladder biopsies. *Arch Pathol Lab Med*, 136(5), 517-526. <https://doi.org/10.5858/arpa.2011-0147-OA>
70. Jansen, R. S., Duijst, S., Mahakena, S., Sommer, D., Szeri, F., Váradi, A., Plomp, A., Bergen, A. A., Oude Elferink, R. P., Borst, P., & van de Wetering, K. (2014, Sep). ABCC6-mediated ATP secretion by the liver is the main source of the mineralization

inhibitor inorganic pyrophosphate in the systemic circulation-brief report.

Arterioscler Thromb Vasc Biol, 34(9), 1985-1989.

<https://doi.org/10.1161/atvbaha.114.304017>

71. Joshi, S., Clapp, W. L., Wang, W., & Khan, S. R. (2015, Sep). Osteogenic changes in kidneys of hyperoxaluric rats. *Biochim Biophys Acta*, 1852(9), 2000-2012.

<https://doi.org/10.1016/j.bbadis.2015.06.020>

72. Joshi, S., Wang, W., Peck, A. B., & Khan, S. R. (2015, May). Activation of the NLRP3 inflammasome in association with calcium oxalate crystal induced reactive oxygen species in kidneys. *J Urol*, 193(5), 1684-1691.

<https://doi.org/10.1016/j.juro.2014.11.093>

73. Khan, S. R. (2004, Jun). Crystal-induced inflammation of the kidneys: results from human studies, animal models, and tissue-culture studies. *Clin Exp Nephrol*, 8(2), 75-88. <https://doi.org/10.1007/s10157-004-0292-0>

74. Khan, S. R. (2012, Apr). Is oxidative stress, a link between nephrolithiasis and obesity, hypertension, diabetes, chronic kidney disease, metabolic syndrome? *Urol Res*, 40(2), 95-112. <https://doi.org/10.1007/s00240-011-0448-9>

75. Khan, S. R., Canales, B. K., & Dominguez-Gutierrez, P. R. (2021, Jun). Randall's plaque and calcium oxalate stone formation: role for immunity and inflammation. *Nat Rev Nephrol*, 17(6), 417-433. <https://doi.org/10.1038/s41581-020-00392-1>

76. Khan, S. R., Joshi, S., Wang, W., & Peck, A. B. (2014, Jun 1). Regulation of macromolecular modulators of urinary stone formation by reactive oxygen species: transcriptional study in an animal model of hyperoxaluria. *Am J Physiol Renal Physiol*, 306(11), F1285-1295. <https://doi.org/10.1152/ajprenal.00057.2014>

77. Khan, S. R., Pearle, M. S., Robertson, W. G., Gambaro, G., Canales, B. K., Doizi, S., Traxer, O., & Tiselius, H. G. (2016, Feb 25). Kidney stones. *Nat Rev Dis Primers*, 2, 16008. <https://doi.org/10.1038/nrdp.2016.8>
78. Khan, S. R., Rodriguez, D. E., Gower, L. B., & Monga, M. (2012, Mar). Association of Randall plaque with collagen fibers and membrane vesicles. *J Urol*, 187(3), 1094-1100. <https://doi.org/10.1016/j.juro.2011.10.125>
79. Khoury, J. D., Fink, L. M., & Vogelzang, N. J. (2008). Call for Revision of College of American Pathologists–Mandated Requirements for Retention of Laboratory Records and Materials. *Archives of Pathology & Laboratory Medicine*, 132(11), 1712-1713. <https://doi.org/10.5858/132.11.1712>
80. Kumada, M., Kihara, S., Ouchi, N., Kobayashi, H., Okamoto, Y., Ohashi, K., Maeda, K., Nagaretani, H., Kishida, K., Maeda, N., Nagasawa, A., Funahashi, T., & Matsuzawa, Y. (2004, May 4). Adiponectin specifically increased tissue inhibitor of metalloproteinase-1 through interleukin-10 expression in human macrophages. *Circulation*, 109(17), 2046-2049. <https://doi.org/10.1161/01.Cir.0000127953.98131.Ed>
81. Kusmartsev, S., Dominguez-Gutierrez, P. R., Canales, B. K., Bird, V. G., Vieweg, J., & Khan, S. R. (2016, Apr). Calcium Oxalate Stone Fragment and Crystal Phagocytosis by Human Macrophages. *J Urol*, 195(4 Pt 1), 1143-1151. <https://doi.org/10.1016/j.juro.2015.11.048>
82. LaFavers, K. A., Macedo, E., Garimella, P. S., Lima, C., Khan, S., Myslinski, J., McClintick, J., Witzmann, F. A., Winfree, S., Phillips, C. L., Hato, T., Dagher, P. C., Wu, X. R., El-Achkar, T. M., & Micanovic, R. (2019, Oct 2). Circulating uromodulin

inhibits systemic oxidative stress by inactivating the TRPM2 channel. *Sci Transl Med*, 11(512). <https://doi.org/10.1126/scitranslmed.aaw3639>

83. Lake, B. B., Chen, S., Hoshi, M., Plongthongkum, N., Salamon, D., Knoten, A., Vijayan, A., Venkatesh, R., Kim, E. H., Gao, D., Gaut, J., Zhang, K., & Jain, S. (2019, Jun 27). A single-nucleus RNA-sequencing pipeline to decipher the molecular anatomy and pathophysiology of human kidneys. *Nat Commun*, 10(1), 2832. <https://doi.org/10.1038/s41467-019-10861-2>
84. Lake, B. B., Menon, R., Winfree, S., Hu, Q., Ferreira, R. M., Kalhor, K., Barwinska, D., Otto, E. A., Ferkowicz, M., Diep, D., Plongthongkum, N., Knoten, A., Urata, S., Naik, A. S., Eddy, S., Zhang, B., Wu, Y., Salamon, D., Williams, J. C., Wang, X., Balderrama, K. S., Hoover, P., Murray, E., Vijayan, A., Chen, F., Waikar, S. S., Rosas, S., Wilson, F. P., Palevsky, P. M., Kiryluk, K., Sedor, J. R., Toto, R. D., Parikh, C., Kim, E. H., Macosko, E. Z., Kharchenko, P. V., Gaut, J. P., Hodgins, J. B., Eadon, M. T., Dagher, P. C., El-Achkar, T. M., Zhang, K., Kretzler, M., Jain, S., & (2021, 2021-01-01 00:00:00). An atlas of healthy and injured cell states and niches in the human kidney. *bioRxiv*.
85. Lee, S. S., Bindokas, V. P., Lingen, M. W., & Kron, S. J. (2019, Sep). Nondestructive, multiplex three-dimensional mapping of immune infiltrates in core needle biopsy. *Lab Invest*, 99(9), 1400-1413. <https://doi.org/10.1038/s41374-018-0156-y>
86. Letavernier, E., Boudier, E., Zaworski, J., Martin, L., & Daudon, M. (2019, Dec 17). Pseudoxanthoma Elasticum, Kidney Stones and Pyrophosphate: From a Rare

Disease to Urolithiasis and Vascular Calcifications. *Int J Mol Sci*, 20(24).

<https://doi.org/10.3390/ijms20246353>

87. Letavernier, E., Kauffenstein, G., Huguet, L., Navasiolava, N., Boudierlique, E., Tang, E., Delaitre, L., Bazin, D., de Frutos, M., Gay, C., Perez, J., Verpont, M. C., Haymann, J. P., Pomozi, V., Zoll, J., Le Saux, O., Daudon, M., Leftheriotis, G., & Martin, L. (2018, Sep). ABCC6 Deficiency Promotes Development of Randall Plaque. *J Am Soc Nephrol*, 29(9), 2337-2347.

<https://doi.org/10.1681/asn.2017101148>

88. Li H. Smile. Published online 2014. <https://haifengl.github.io>

89. Li, T., Li, X., Feng, Y., Dong, G., Wang, Y., & Yang, J. (2020). The Role of Matrix Metalloproteinase-9 in Atherosclerotic Plaque Instability. *Mediators Inflamm*, 2020, 3872367. <https://doi.org/10.1155/2020/3872367>

90. Li, W., Germain, R. N., & Gerner, M. Y. (2017, Aug 29). Multiplex, quantitative cellular analysis in large tissue volumes with clearing-enhanced 3D microscopy (C(e)3D). *Proc Natl Acad Sci U S A*, 114(35), E7321-e7330.

<https://doi.org/10.1073/pnas.1708981114>

91. Lillie, R. D. (1951, May). The allochrome procedure; a differential method segregating the connective tissues collagen, reticulum and basement membranes into two groups. *Am J Clin Pathol*, 21(5), 484-488.

92. Lin, J. R., Izar, B., Wang, S., Yapp, C., Mei, S., Shah, P. M., Santagata, S., & Sorger, P. K. (2018, Jul 11). Highly multiplexed immunofluorescence imaging of human tissues and tumors using t-CyCIF and conventional optical microscopes. *Elife*, 7.

<https://doi.org/10.7554/eLife.31657>

93. Liu, Q., Mukhopadhyay, S., Rodriguez, M. X. B., Fu, X., Sahu, S., Burk, D., & Gartia, M. (2020, 3-7 April 2020). A One-Shot Learning Framework for Assessment of Fibrillar Collagen from Second Harmonic Generation Images of an Infarcted Myocardium. 2020 IEEE 17th International Symposium on Biomedical Imaging (ISBI)
94. Liu, Z., Gerner, M. Y., Van Panhuys, N., Levine, A. G., Rudensky, A. Y., & Germain, R. N. (2015, Dec 10). Immune homeostasis enforced by co-localized effector and regulatory T cells. *Nature*, 528(7581), 225-230.  
<https://doi.org/10.1038/nature16169>
95. Liu, Z., Tan, R. J., & Liu, Y. (2020, Jun 25). The Many Faces of Matrix Metalloproteinase-7 in Kidney Diseases. *Biomolecules*, 10(6).  
<https://doi.org/10.3390/biom10060960>
96. Makki, M. S., Winfree, S., Lingeman, J. E., Witzmann, F. A., Worcester, E. M., Krambeck, A. E., Coe, F. L., Evan, A. P., Bledsoe, S., Bergsland, K. J., Khochare, S., Barwinska, D., Williams, J. C., Jr., & El-Achkar, T. M. (2020, May). A Precision Medicine Approach Uncovers a Unique Signature of Neutrophils in Patients With Brushite Kidney Stones. *Kidney Int Rep*, 5(5), 663-677.  
<https://doi.org/10.1016/j.ekir.2020.02.1025>
97. Malone, A. F., Wu, H., & Humphreys, B. D. (2018, Jan). Bringing Renal Biopsy Interpretation Into the Molecular Age With Single-Cell RNA Sequencing. *Semin Nephrol*, 38(1), 31-39. <https://doi.org/10.1016/j.semnephrol.2017.09.005>



98. Manicone, A. M., & McGuire, J. K. (2008, Feb). Matrix metalloproteinases as modulators of inflammation. *Semin Cell Dev Biol*, 19(1), 34-41.  
<https://doi.org/10.1016/j.semcdb.2007.07.003>
99. Matsui, T., Mizuno, H., Sudo, T., Kikuta, J., Haraguchi, N., Ikeda, J.-i., Mizushima, T., Yamamoto, H., Morii, E., Mori, M., & Ishii, M. (2017, 2017/07/31). Non-labeling multiphoton excitation microscopy as a novel diagnostic tool for discriminating normal tissue and colorectal cancer lesions. *Scientific Reports*, 7(1), 6959.  
<https://doi.org/10.1038/s41598-017-07244-2>
100. Mehde, A. A., Mehdi, W. A., Yusof, F., Raus, R. A., Zainal Abidin, Z. A., Ghazali, H., & Abd Rahman, A. (2018, Jan). Association of MMP-9 gene polymorphisms with nephrolithiasis patients. *J Clin Lab Anal*, 32(1).  
<https://doi.org/10.1002/jcla.22173>
101. Melo Ferreira, R., Freije, B. J., & Eadon, M. T. (2021). Deconvolution Tactics and Normalization in Renal Spatial Transcriptomics. *Front Physiol*, 12, 812947.  
<https://doi.org/10.3389/fphys.2021.812947>
102. Melo Ferreira, R., Sabo, A. R., Winfree, S., Collins, K. S., Janosevic, D., Gulbranson, C. J., Cheng, Y. H., Casbon, L., Barwinska, D., Ferkowicz, M. J., Xuei, X., Zhang, C., Dunn, K. W., Kelly, K. J., Sutton, T. A., Hato, T., Dagher, P. C., El-Achkar, T. M., & Eadon, M. T. (2021, Jun 22). Integration of spatial and single-cell transcriptomics localizes epithelial cell-immune cross-talk in kidney injury. *JCI Insight*, 6(12). <https://doi.org/10.1172/jci.insight.147703>

103. Messias, N. C., Walker, P. D., & Larsen, C. P. (2015, Jun). Paraffin immunofluorescence in the renal pathology laboratory: more than a salvage technique. *Mod Pathol*, 28(6), 854-860. <https://doi.org/10.1038/modpathol.2015.1>
104. Micanovic, R., Khan, S., Janosevic, D., Lee, M. E., Hato, T., Srour, E. F., Winfree, S., Ghosh, J., Tong, Y., Rice, S. E., Dagher, P. C., Wu, X. R., & El-Achkar, T. M. (2018, Mar). Tamm-Horsfall Protein Regulates Mononuclear Phagocytes in the Kidney. *J Am Soc Nephrol*, 29(3), 841-856. <https://doi.org/10.1681/asn.2017040409>
105. Micanovic, R., LaFavers, K., Garimella, P. S., Wu, X. R., & El-Achkar, T. M. (2020, Jan 1). Uromodulin (Tamm-Horsfall protein): guardian of urinary and systemic homeostasis. *Nephrol Dial Transplant*, 35(1), 33-43. <https://doi.org/10.1093/ndt/gfy394>
106. Modlin, M. (1980, Oct 18). A history of urinary stone. *S Afr Med J*, 58(16), 652-655.
107. Moore, J., Allan, C., Besson, S., Burel, J.-M., Diel, E., Gault, D., Kozlowski, K., Lindner, D., Linkert, M., Manz, T., Moore, W., Pape, C., Tischer, C., & Swedlow, J. R. (2021, 2021-01-01 00:00:00). OME-NGFF: scalable format strategies for interoperable bioimaging data. *bioRxiv*.
108. Moraes, D. A., Sibov, T. T., Pavon, L. F., Alvim, P. Q., Bonadio, R. S., Da Silva, J. R., Pic-Taylor, A., Toledo, O. A., Marti, L. C., Azevedo, R. B., & Oliveira, D. M. (2016, Jul 28). A reduction in CD90 (THY-1) expression results in increased differentiation of mesenchymal stromal cells. *Stem Cell Res Ther*, 7(1), 97. <https://doi.org/10.1186/s13287-016-0359-3>

109. Moreau, H. D., Lemaître, F., Terriac, E., Azar, G., Piel, M., Lennon-Dumenil, A. M., & Bousso, P. (2012, Aug 24). Dynamic in situ cytometry uncovers T cell receptor signaling during immunological synapses and kinapses in vivo. *Immunity*, 37(2), 351-363. <https://doi.org/10.1016/j.immuni.2012.05.014>
110. Mushtaq, S., Siddiqui, A. A., Naqvi, Z. A., Rattani, A., Talati, J., Palmberg, C., & Shafqat, J. (2007, Sep). Identification of myeloperoxidase, alpha-defensin and calgranulin in calcium oxalate renal stones. *Clin Chim Acta*, 384(1-2), 41-47. <https://doi.org/10.1016/j.cca.2007.05.015>
111. Neumann, E. K., Patterson, N. H., Rivera, E. S., Allen, J. L., Brewer, M., deCaestecker, M. P., Caprioli, R. M., Fogo, A. B., & Spraggins, J. M. (2022, Jan). Highly multiplexed immunofluorescence of the human kidney using co-detection by indexing. *Kidney Int*, 101(1), 137-143. <https://doi.org/10.1016/j.kint.2021.08.033>
112. Okada, A., Yasui, T., Hamamoto, S., Hirose, M., Kubota, Y., Itoh, Y., Tozawa, K., Hayashi, Y., & Kohri, K. (2009, May). Genome-wide analysis of genes related to kidney stone formation and elimination in the calcium oxalate nephrolithiasis model mouse: detection of stone-preventive factors and involvement of macrophage activity. *J Bone Miner Res*, 24(5), 908-924. <https://doi.org/10.1359/jbmr.081245>
113. Okumura, N., Tsujihata, M., Momohara, C., Yoshioka, I., Suto, K., Nonomura, N., Okuyama, A., & Takao, T. (2013). Diversity in protein profiles of individual calcium oxalate kidney stones. *PLOS ONE*, 8(7), e68624. <https://doi.org/10.1371/journal.pone.0068624>

114. Otsu, N. (1979). A Threshold Selection Method from Gray-Level Histograms. *IEEE Transactions on Systems, Man, and Cybernetics*, 9(1), 62-66.  
<https://doi.org/10.1109/TSMC.1979.4310076>
115. Park, J., Liu, C. L., Kim, J., & Susztak, K. (2019, Oct). Understanding the kidney one cell at a time. *Kidney Int*, 96(4), 862-870.  
<https://doi.org/10.1016/j.kint.2019.03.035>
116. Petrovas, C., Ferrando-Martinez, S., Gerner, M. Y., Casazza, J. P., Pegu, A., Deleage, C., Cooper, A., Hataye, J., Andrews, S., Ambrozak, D., Del Río Estrada, P. M., Boritz, E., Paris, R., Moysi, E., Boswell, K. L., Ruiz-Mateos, E., Vagios, I., Leal, M., Ablanedo-Terrazas, Y., Rivero, A., Gonzalez-Hernandez, L. A., McDermott, A. B., Moir, S., Reyes-Terán, G., Docobo, F., Pantaleo, G., Douek, D. C., Betts, M. R., Estes, J. D., Germain, R. N., Mascola, J. R., & Koup, R. A. (2017, Jan 18). Follicular CD8 T cells accumulate in HIV infection and can kill infected cells in vitro via bispecific antibodies. *Sci Transl Med*, 9(373).  
<https://doi.org/10.1126/scitranslmed.aag2285>
117. Pritzker, K. P. H., & Nieminen, H. J. (2019, Nov). Needle Biopsy Adequacy in the Era of Precision Medicine and Value-Based Health Care. *Arch Pathol Lab Med*, 143(11), 1399-1415. <https://doi.org/10.5858/arpa.2018-0463-RA>
118. Pulido-Olmo, H., García-Prieto, C. F., Álvarez-Llamas, G., Barderas, M. G., Vivanco, F., Aranguez, I., Somoza, B., Segura, J., Kreutz, R., Fernández-Alfonso, M. S., Ruilope, L. M., & Ruiz-Hurtado, G. (2016, Apr 1). Role of matrix metalloproteinase-9 in chronic kidney disease: a new biomarker of resistant albuminuria. *Clin Sci (Lond)*, 130(7), 525-538. <https://doi.org/10.1042/cs20150517>

119. Radtke, A. J., Kastenmüller, W., Espinosa, D. A., Gerner, M. Y., Tse, S. W., Sinnis, P., Germain, R. N., Zavala, F. P., & Cockburn, I. A. Lymph-node resident CD8 $\alpha$ <sup>+</sup> dendritic cells capture antigens from migratory malaria sporozoites and induce CD8<sup>+</sup> T cell responses. (1553-7374 (Electronic)).
120. Ranjit, S., Dobrinskikh, E., Montford, J., Dvornikov, A., Lehman, A., Orlicky, D. J., Nemenoff, R., Gratton, E., Levi, M., & Furgeson, S. Label-free fluorescence lifetime and second harmonic generation imaging microscopy improves quantification of experimental renal fibrosis. (1523-1755 (Electronic)).
121. Ranjit, S., Dvornikov, A., Stakic, M., Hong, S.-H., Levi, M., Evans, R. M., & Gratton, E. (2015, 2015/08/21). Imaging Fibrosis and Separating Collagens using Second Harmonic Generation and Phasor Approach to Fluorescence Lifetime Imaging. *Scientific Reports*, 5(1), 13378. <https://doi.org/10.1038/srep13378>
122. Ransick, A., Lindström, N. O., Liu, J., Zhu, Q., Guo, J. J., Alvarado, G. F., Kim, A. D., Black, H. G., Kim, J., & McMahon, A. P. Single-Cell Profiling Reveals Sex, Lineage, and Regional Diversity in the Mouse Kidney. (1878-1551 (Electronic)).
123. Rivenson, Y., Wang, H., Wei, Z., de Haan, K., Zhang, Y., Wu, Y., Gunaydin, H., Zuckerman, J. E., Chong, T., Sisk, A. E., Westbrook, L. M., Wallace, W. D., & Ozcan, A. (2019, Jun). Virtual histological staining of unlabelled tissue-autofluorescence images via deep learning. *Nat Biomed Eng*, 3(6), 466-477. <https://doi.org/10.1038/s41551-019-0362-y>
124. Roth, R., Parikh, S., Makey, D., Foster, J., Rozenblit, G., Satoskar, A., Nadasdy, G., Von Visger, J., Hebert, L., Rovin, B. H., Nadasdy, T., & Brodsky, S. V. (2013).

- When size matters: diagnostic value of kidney biopsy according to the gauge of the biopsy needle. *Am J Nephrol*, 37(3), 249-254. <https://doi.org/10.1159/000347219>
125. Rueden, C., Schindelin, J., Hiner, M. & Eliceiri, K. (2021). SciJava Common [Software]. <https://scijava.org/>.
  126. Sabo, A. R., Winfree, S., Bledsoe, S. B., Phillips, C. L., Lingeman, J. E., Eadon, M. T., Williams, J. C., Jr., & El-Achkar, T. A.-O. Label-free imaging of non-deparaffinized sections of the human kidney to determine tissue quality and signatures of disease. (2051-817X (Electronic)).
  127. Sarangi, R., Tripathy, K. P., Bahinipati, J., Gupta, P., Pathak, M., Mahapatra, S., & Mohapatra, S. A.-O. Urinary MMP-7: A Predictive, Noninvasive Early Marker for Chronic Kidney Disease Development in Patients with Hypertension. (1943-7730 (Electronic)).
  128. Scales, C. D., Jr., Smith Ac Fau - Hanley, J. M., Hanley Jm Fau - Saigal, C. S., & Saigal, C. S. Prevalence of kidney stones in the United States. (1873-7560 (Electronic)).
  129. Schindelin, J., Arganda-Carreras I Fau - Frise, E., Frise E Fau - Kaynig, V., Kaynig V Fau - Longair, M., Longair M Fau - Pietzsch, T., Pietzsch T Fau - Preibisch, S., Preibisch S Fau - Rueden, C., Rueden C Fau - Saalfeld, S., Saalfeld S Fau - Schmid, B., Schmid B Fau - Tinevez, J.-Y., Tinevez Jy Fau - White, D. J., White Dj Fau - Hartenstein, V., Hartenstein V Fau - Eliceiri, K., Eliceiri K Fau - Tomancak, P., Tomancak P Fau - Cardona, A., & Cardona, A. Fiji: an open-source platform for biological-image analysis. (1548-7105 (Electronic)).

130. Schubert, W., Bonnekoh B Fau - Pommer, A. J., Pommer Aj Fau - Philipsen, L., Philipsen L Fau - Böckelmann, R., Böckelmann R Fau - Malykh, Y., Malykh Y Fau - Gollnick, H., Gollnick H Fau - Friedenberger, M., Friedenberger M Fau - Bode, M., Bode M Fau - Dress, A. W. M., & Dress, A. W. Analyzing proteome topology and function by automated multidimensional fluorescence microscopy. (1087-0156 (Print)).
131. Schürch, C. M., Bhate, S. S., Barlow, G. L., Phillips, D. J., Noti, L., Zlobec, I., Chu, P., Black, S., Demeter, J., McIlwain, D. R., Kinoshita, S., Samusik, N., Goltsev, Y., & Nolan, G. P. Coordinated Cellular Neighborhoods Orchestrate Antitumoral Immunity at the Colorectal Cancer Invasive Front. (1097-4172 (Electronic)).
132. Shah, J., & Whitfield, H. N. Urolithiasis through the ages. (1464-4096 (Print)).
133. Shrestha, S., Singhal, S., Kalonick, M., Guyer, R., Volkert, A., Somji, S., Garrett, S. H., Sens, D. A., & Singhal, S. A.-O. X. Role of HRTPT in kidney proximal epithelial cell regeneration: Integrative differential expression and pathway analyses using microarray and scRNA-seq. (1582-4934 (Electronic)).
134. Stoltzfus, C. R., Filipek, J., Gern, B. H., Olin, B. E., Leal, J. M., Wu, Y., Lyons-Cohen, M. R., Huang, J. Y., Paz-Stoltzfus, C. L., Plumlee, C. R., Pöschinger, T., Urdahl, K. B., Perro, M., & Gerner, M. Y. CytoMAP: A Spatial Analysis Toolbox Reveals Features of Myeloid Cell Organization in Lymphoid Tissues. (2211-1247 (Electronic)).
135. Stoltzfus, C. R., Sivakumar, R., Kunz, L., Olin Pope, B. E., Menietti, E., Speziale, D., Adelfio, R., Bacac, M., Colombetti, S., Perro, M., & Gerner, M. Y. Multi-

Parameter Quantitative Imaging of Tumor Microenvironments Reveals Perivascular Immune Niches Associated With Anti-Tumor Immunity. (1664-3224 (Electronic)).

136. Strupler M Fau - Pena, A. M., Pena Am Fau - Hernest, M., Hernest M Fau - Tharaux, P. L., Tharaux Pl Fau - Martin, J. L., Martin JI Fau - Beaurepaire, E., Beaurepaire E Fau - Schanne-Klein, M. C., & Schanne-Klein, M. C. Second harmonic imaging and scoring of collagen in fibrotic tissues. (1094-4087 (Electronic)).
137. Strupler, M., Hernest M Fau - Fligny, C., Fligny C Fau - Martin, J.-L., Martin JI Fau - Tharaux, P.-L., Tharaux Pl Fau - Schanne-Klein, M.-C., & Schanne-Klein, M. C. Second harmonic microscopy to quantify renal interstitial fibrosis and arterial remodeling. (1083-3668 (Print)).
138. Surendran, K., Simon Tc Fau - Liapis, H., Liapis H Fau - McGuire, J. K., & McGuire, J. K. Matrilysin (MMP-7) expression in renal tubular damage: association with Wnt4. (0085-2538 (Print)).
139. Taguchi, K., Hamamoto, S., Okada, A., Sugino, T., Unno, R., Ando, R., Gao, B., Tozawa, K., Kohri, K., & Yasui, T. (2019, Jun). Helper T-cell signaling and inflammatory pathway lead to formation of calcium phosphate but not calcium oxalate stones on Randall's plaques. *Int J Urol*, 26(6), 670-677.  
<https://doi.org/10.1111/iju.13950>
140. Taguchi, K., Hamamoto, S., Okada, A., Unno, R., Kamisawa, H., Naiki, T., Ando, R., Mizuno, K., Kawai, N., Tozawa, K., Kohri, K., & Yasui, T. (2017, Jan). Genome-Wide Gene Expression Profiling of Randall's Plaques in Calcium Oxalate Stone Formers. *J Am Soc Nephrol*, 28(1), 333-347. <https://doi.org/10.1681/asn.2015111271>



141. Taguchi, K., Okada, A., Hamamoto, S., Unno, R., Moritoki, Y., Ando, R., Mizuno, K., Tozawa, K., Kohri, K., & Yasui, T. (2016, 2016/10/12). M1/M2-macrophage phenotypes regulate renal calcium oxalate crystal development. *Scientific Reports*, 6(1), 35167. <https://doi.org/10.1038/srep35167>
142. Taguchi, K., Okada, A., Unno, R., Hamamoto, S., & Yasui, T. (2021). Macrophage Function in Calcium Oxalate Kidney Stone Formation: A Systematic Review of Literature. *Front Immunol*, 12, 673690. <https://doi.org/10.3389/fimmu.2021.673690>
143. Tan, T. K., Zheng, G., Hsu, T. T., Lee, S. R., Zhang, J., Zhao, Y., Tian, X., Wang, Y., Wang, Y. M., Cao, Q., Wang, Y., Lee, V. W., Wang, C., Zheng, D., Alexander, S. I., Thompson, E., & Harris, D. C. (2013, Apr). Matrix metalloproteinase-9 of tubular and macrophage origin contributes to the pathogenesis of renal fibrosis via macrophage recruitment through osteopontin cleavage. *Lab Invest*, 93(4), 434-449. <https://doi.org/10.1038/labinvest.2013.3>
144. Tan, T. K., Zheng, G., Hsu, T. T., Wang, Y., Lee, V. W., Tian, X., Wang, Y., Cao, Q., Wang, Y., & Harris, D. C. (2010, Mar). Macrophage matrix metalloproteinase-9 mediates epithelial-mesenchymal transition in vitro in murine renal tubular cells. *Am J Pathol*, 176(3), 1256-1270. <https://doi.org/10.2353/ajpath.2010.090188>
145. Tang, P. M., Nikolic-Paterson, D. J., & Lan, H. Y. (2019, Mar). Macrophages: versatile players in renal inflammation and fibrosis. *Nat Rev Nephrol*, 15(3), 144-158. <https://doi.org/10.1038/s41581-019-0110-2>

146. Tewari, A. K., Shevchuk, M. M., Sterling, J., Grover, S., Herman, M., Yadav, R., Mudalair, K., Srivastava, A., Rubin, M. A., Zipfel, W. R., Maxfield, F. R., Xu, C., Webb, W. W., & Mukherjee, S. (2011, Nov). Multiphoton microscopy for structure identification in human prostate and periprostatic tissue: implications in prostate cancer surgery. *BJU Int*, 108(9), 1421-1429. <https://doi.org/10.1111/j.1464-410X.2011.10169.x>
147. Thomas M. h2. Published online 2005.  
<https://www.h2database.com/html/main.html>
148. Varberg, K. M., Winfree, S., Chu, C., Tu, W., Blue, E. K., Gohn, C. R., Dunn, K. W., & Haneline, L. S. (2017, Apr 1). Kinetic analyses of vasculogenesis inform mechanistic studies. *Am J Physiol Cell Physiol*, 312(4), C446-c458.  
<https://doi.org/10.1152/ajpcell.00367.2016>
149. Wählby, C., Erlandsson, F., Bengtsson, E., & Zetterberg, A. (2002, Jan 1). Sequential immunofluorescence staining and image analysis for detection of large numbers of antigens in individual cell nuclei. *Cytometry*, 47(1), 32-41.
150. Wang, X., Yu, Y. Y., Lieu, S., Yang, F., Lang, J., Lu, C., Werb, Z., Hu, D., Miclau, T., Marcucio, R., & Colnot, C. (2013, Jan). MMP9 regulates the cellular response to inflammation after skeletal injury. *Bone*, 52(1), 111-119.  
<https://doi.org/10.1016/j.bone.2012.09.018>
151. Wang, Y., Woehrstein, J. B., Donoghue, N., Dai, M., Avendaño, M. S., Schackmann, R. C. J., Zoeller, J. J., Wang, S. S. H., Tillberg, P. W., Park, D., Lapan, S. W., Boyden, E. S., Brugge, J. S., Kaeser, P. S., Church, G. M., Agasti, S. S., Jungmann, R., & Yin, P. (2017, Oct 11). Rapid Sequential in Situ Multiplexing with

- DNA Exchange Imaging in Neuronal Cells and Tissues. *Nano Lett*, 17(10), 6131-6139. <https://doi.org/10.1021/acs.nanolett.7b02716>
152. Watson, A. M., Rose, A. H., Gibson, G. A., Gardner, C. L., Sun, C., Reed, D. S., Lam, L. K. M., St Croix, C. M., Strick, P. L., Klimstra, W. B., & Watkins, S. C. (2017). Ribbon scanning confocal for high-speed high-resolution volume imaging of brain. *PLOS ONE*, 12(7), e0180486. <https://doi.org/10.1371/journal.pone.0180486>
  153. Winfree, S., Al Hasan, M., & El-Achkar, T. M. (2022, May 26). Profiling Immune Cells in the Kidney Using Tissue Cytometry and Machine Learning. *Kidney360*, 3(5), 968-978. <https://doi.org/10.34067/kid.0006802020>
  154. Winfree, S., Dagher, P. C., Dunn, K. W., Eadon, M. T., Ferkowicz, M., Barwinska, D., Kelly, K. J., Sutton, T. A., & El-Achkar, T. M. (2018). Quantitative Large-Scale Three-Dimensional Imaging of Human Kidney Biopsies: A Bridge to Precision Medicine in Kidney Disease. *Nephron*, 140(2), 134-139. <https://doi.org/10.1159/000490006>
  155. Winfree, S., Ferkowicz, M. J., Dagher, P. C., Kelly, K. J., Eadon, M. T., Sutton, T. A., Markel, T. A., Yoder, M. C., Dunn, K. W., & El-Achkar, T. M. (2017, Nov). Large-scale 3-dimensional quantitative imaging of tissues: state-of-the-art and translational implications. *Transl Res*, 189, 1-12. <https://doi.org/10.1016/j.trsl.2017.07.006>
  156. Winfree, S., Khan, S., Micanovic, R., Eadon, M. T., Kelly, K. J., Sutton, T. A., Phillips, C. L., Dunn, K. W., & El-Achkar, T. M. (2017, Jul). Quantitative Three-Dimensional Tissue Cytometry to Study Kidney Tissue and Resident Immune Cells. *J Am Soc Nephrol*, 28(7), 2108-2118. <https://doi.org/10.1681/asn.2016091027>

157. Winfree, S., McNutt, A. T., Khochare, S., Borgard, T. J., Barwinska, D., Sabo, A. R., Ferkowicz, M. J., Williams, J. C., Lingeman, J. E., Gulbronson, C. J., Kelly, K. J., Sutton, T. A., Dagher, P. C., Eadon, M. T., Dunn, K. W., & El-Achkar, T. M. (2022, 2022-01-01 00:00:00). Integrated cytometry with machine learning applied to high-content imaging of human kidney tissue for in-situ cell classification and neighborhood analysis. *bioRxiv*.
158. Winfree, S., Weiler, C., Bledsoe, S. B., Gardner, T., Sommer, A. J., Evan, A. P., Lingeman, J. E., Krambeck, A. E., Worcester, E. M., El-Achkar, T. M., & Williams, J. C., Jr. (2021, Apr). Multimodal imaging reveals a unique autofluorescence signature of Randall's plaque. *Urolithiasis*, 49(2), 123-135.  
<https://doi.org/10.1007/s00240-020-01216-4>
159. Witzmann, F. A., Evan, A. P., Coe, F. L., Worcester, E. M., Lingeman, J. E., & Williams, J. C., Jr. (2016). Label-free proteomic methodology for the analysis of human kidney stone matrix composition. *Proteome Sci*, 14, 4.  
<https://doi.org/10.1186/s12953-016-0093-x>
160. Woloshuk, A., Khochare, S., Almulhim, A. F., McNutt, A. T., Dean, D., Barwinska, D., Ferkowicz, M. J., Eadon, M. T., Kelly, K. J., Dunn, K. W., Hasan, M. A., El-Achkar, T. M., & Winfree, S. (2021, Jul). In Situ Classification of Cell Types in Human Kidney Tissue Using 3D Nuclear Staining. *Cytometry A*, 99(7), 707-721.  
<https://doi.org/10.1002/cyto.a.24274>
161. Worcester, E. M., & Coe, F. L. (2010, Sep 2). Clinical practice. Calcium kidney stones. *N Engl J Med*, 363(10), 954-963. <https://doi.org/10.1056/NEJMcp1001011>

162. Wu, L., Chang, D. Y., Zhang, L. X., Chen, M., & Zhao, M. H. (2021, Feb). Urinary soluble CD90 predicts renal prognosis in patients with diabetic kidney disease. *Ann Transl Med*, 9(4), 282. <https://doi.org/10.21037/atm-20-6528>
163. Wu, Y., Zhang, J., Li, C., Hu, H., Qin, B., Wang, T., Lu, Y., & Wang, S. (2021). The Activation of ROS/NF- $\kappa$ B/MMP-9 Pathway Promotes Calcium-Induced Kidney Crystal Deposition. *Oxid Med Cell Longev*, 2021, 8836355. <https://doi.org/10.1155/2021/8836355>
164. Xi, J., Chen, Y., Jing, J., Zhang, Y., Liang, C., Hao, Z., & Zhang, L. (2019, Jul). Sirtuin 3 suppresses the formation of renal calcium oxalate crystals through promoting M2 polarization of macrophages. *J Cell Physiol*, 234(7), 11463-11473. <https://doi.org/10.1002/jcp.27803>
165. Xia, Y., Zhou, X., Ye, Z., Yu, W., Ning, J., Ruan, Y., Yuan, R., Lin, F., Ye, P., Zheng, D., Rao, T., & Cheng, F. (2021). Construction and Analysis of Immune Infiltration-Related ceRNA Network for Kidney Stones. *Front Genet*, 12, 774155. <https://doi.org/10.3389/fgene.2021.774155>
166. Yang, X., Ou, J., Zhang, H., Xu, X., Zhu, L., Li, Q., Li, J., Xie, D., Sun, J., Zha, Y., Li, Y., Tian, J., Liu, Y., & Hou, F. F. (2020, Mar). Urinary Matrix Metalloproteinase 7 and Prediction of IgA Nephropathy Progression. *Am J Kidney Dis*, 75(3), 384-393. <https://doi.org/10.1053/j.ajkd.2019.07.018>
167. Yu, G., & He, Q. Y. (2016, Feb). ReactomePA: an R/Bioconductor package for reactome pathway analysis and visualization. *Mol Biosyst*, 12(2), 477-479. <https://doi.org/10.1039/c5mb00663e>

168. Yu, G., Wang, L. G., Han, Y., & He, Q. Y. (2012, May). clusterProfiler: an R package for comparing biological themes among gene clusters. *Omics*, 16(5), 284-287. <https://doi.org/10.1089/omi.2011.0118>
169. Yunna, C., Mengru, H., Lei, W., & Weidong, C. (2020, Jun 15). Macrophage M1/M2 polarization. *Eur J Pharmacol*, 877, 173090. <https://doi.org/10.1016/j.ejphar.2020.173090>
170. Zhou, D., Tian, Y., Sun, L., Zhou, L., Xiao, L., Tan, R. J., Tian, J., Fu, H., Hou, F. F., & Liu, Y. (2017, Feb). Matrix Metalloproteinase-7 Is a Urinary Biomarker and Pathogenic Mediator of Kidney Fibrosis. *J Am Soc Nephrol*, 28(2), 598-611. <https://doi.org/10.1681/asn.2016030354>

## Curriculum Vitae

**Angela Renae Sabo**

### Education

2018-2023                      PhD, Cellular and Integrative Physiology, Indiana University,  
Indianapolis, IN

Laboratories of James C. Williams, Jr. and Tarek El-Achkar  
*Multiplexed high-resolution imaging approach to decipher the  
cellular heterogeneity of the kidney and its alteration in kidney  
disease and nephrolithiasis*

2015-2018                      BS, Biological Sciences, Indiana University Southeast, New  
Albany, IN

### Publications

#### *In-press*

1. Ferkowicz, M.J., Winfree, S., **Sabo, A.R.** et al. (2021). Large-scale, three-dimensional tissue cytometry of the human kidney: a complete and accessible pipeline. *Laboratory Investigation*, 101, 661–676
2. Melo Ferreira, R., **Sabo, A. R.**, Winfree, S., et al. (2021). Integration of spatial and single-cell transcriptomics localizes epithelial cell-immune cross-talk in kidney injury. *JCI insight*, 6(12), e147703.
3. **Sabo, A. R.**, Winfree, S., Bledsoe, S. B., et al. (2022). Label-free imaging of non-deparaffinized sections of the human kidney to determine tissue quality and signatures of disease. *Physiological Reports*, 10(3), e15167.

4. Micanovic, R., LaFavers, K. A., ... **Sabo, A. R.**, et al (2022). The kidney releases a nonpolymerizing form of uromodulin in the urine and circulation that retains the external hydrophobic patch domain. *American Journal of Physiology-Renal Physiology*, 322(4), F403-F418.
5. LaFavers, K. A., Micanovic, R., **Sabo, A. R.**, et al. (2022). Evolving Concepts in Uromodulin Biology, Physiology, and Its Role in Disease: a Tale of Two Forms. *Hypertension*, 79(11), 2409-2418.
6. **Sabo, A. R.**, Winfree, S., & El-Achkar, T. M. (2022). Defining protein expression in the kidney at large scale: from antibody validation to cytometry analysis. *American Journal of Physiology-Renal Physiology*.

***Submitted or in preparation***

1. Winfree, S., McNutt, A. T., ... **Sabo, A. R.**, et al (2021). Integrated cytometry with machine learning applied to high-content imaging of human kidney tissue for in-situ cell classification and neighborhood analysis. *bioRxiv*.
2. Canela, V. H., Bowen, W. S., ... **Sabo, A. R.**, et al (2022). A spatially anchored transcriptomic atlas of the human kidney papilla identifies significant immune injury and matrix remodeling in patients with stone disease. *bioRxiv*.

**Presentations**

***Oral presentation***

2022	ASN Kidney Week 2022 American Society of Nephrology, Orlando FL
2020	Kidney Precision Medicine Project Face to Face, KPMP, Virtual Meeting



- 2020 Renal Research Conference, IU School of Medicine – Department of Nephrology, IUSM, Indianapolis, IN
- 2019 ASN Kidney Week 2019 American Society of Nephrology, Washington D.C.

***Poster presentation***

- 2022 ASN Kidney Week 2022 American Society of Nephrology, Orlando FL
- 2022 The 2<sup>nd</sup> Acute Kidney Injury Conference: From Bench to Bedside, FASEB, Banff Canada

**Awards and Scholarships**

- 2022 Knoebel Fellowship – Travel Award, IUSM Department of Anatomy, Cell Biology & Physiology, Indianapolis, IN
- 2022 Travel Award – Kidney Precision Medicine Project Face to Face Meeting, KPMP, Washington D.C.
- 2022 The 2<sup>nd</sup> Acute Kidney Injury Conference: From Bench to Bedside Travel Award, FASEB, Banff Canada
- 2020 Moenkhaus Fellowship Award, IUSM Department of Anatomy, Cell Biology & Physiology, Indianapolis, IN